



ATLAS Note

ATL-COM-PHYS-2019-962

1st June 2021



1

2 WZ + Heavy Flavor Production in pp collisions 3 at $\sqrt{s} = 13$ TeV

4

The ATLAS Collaboration¹, Aaron Webb^a, Peter Onyisi^a

5

^a*Univ. of Texas at Austin*

6

A measurement of the cross-section for production of WZ with an associated heavy flavor jet
7 is performed using 140 fb^{-1} of proton-proton collision data at $\sqrt{s} = 13$ TeV from the ATLAS
8 experiment at the LHC. A measurement of the fully leptonic decay mode, $WZ \rightarrow l\nu ll$, is
9 performed. The cross-section of $WZ + b$ and $WZ + \text{charm}$ in various fiducial regions is
10 measured.

11

© 2021 CERN for the benefit of the ATLAS Collaboration.

Reproduction of this article or parts of it is allowed as specified in the CC-BY-4.0 license.

12 Contents

13	1 Changes and outstanding items	4
14	1.1 Changelog	4
15	1.1.1 Changes relative to v9	4
16	1.1.2 Changes relative to v8	4
17	1.1.3 Changes relative to v7	5
18	1.1.4 Changes relative to v5	5
19	1.1.5 Changes relative to v4	5
20	1.1.6 Changes relative to v3	6
21	1.1.7 Changes relative to v2	6
22	1.1.8 Changes relative to v1	7
23	1.2 Outstanding Items	7
24	2 Executive Summary	8
25	3 Data and Monte Carlo Samples	9
26	3.1 Data Samples	9
27	3.2 Monte Carlo Samples	10
28	4 Object Reconstruction	11
29	4.1 Trigger	11
30	4.2 Light leptons	12
31	4.3 Jets	13
32	4.4 B-tagged Jets	13
33	4.5 Missing transverse energy	15
34	4.6 Overlap removal	15
35	5 tZ Separation Multivariate Analysis	15
36	5.1 Top Mass Reconstruction	16
37	5.2 tZ BDT	16
38	5.3 tZ Interference Studies	20
39	6 Event Selection and Signal Region Definitions	22
40	6.1 Event Preselection	22
41	6.2 Fit Regions	26
42	6.3 Non-Prompt Lepton Estimation	42
43	6.3.1 $t\bar{t}$ Validation	42
44	6.3.2 Z+jets Validation	45
45	7 Systematic Uncertainties	49
46	8 Results	58
47	8.1 Fit Procedure	58
48	8.2 Results of the Simultaneous Fit	59

49	8.3 Inclusive 1+2 Jet Fit	70
50	8.4 Alternate tZ Inclusive Fit	74
51	8.4.1 tZ Inclusive Fit	74
52	8.4.2 Floating tZ	74
53	9 Conclusion	75
54	A Appendices	78
55	Appendices	78
56	A.1 Non-prompt lepton MVA	78
57	A.2 Non-prompt CR Modelling	80
58	A.3 DSID list	84

59 List of contributions

60	Aaron Webb	Main analyser. Responsible for ntuple production, fits, and note writing.
61	Peter Onyisi	Advisor to Aaron Webb. Analysis design and implementation strategy.

62 **1 Changes and outstanding items**

63 **1.1 Changelog**

64 This is version 10

65 **1.1.1 Changes relative to v9**

- 66 • Reordered note to put fiducial region definition in the intro, tZ BDT before the event
67 selection
- 68 • moved alternative fit strategies from the appendix into the main text of the note
- 69 • removed correlation matrix plot from results
- 70 • added c/light rejection rates for each DL1r WP
- 71 • updated OR procedure - previously had an outdated algorithm
- 72 • Updated results section to include latest fits, table summarizing results
- 73 • Replaced correlation table with a plot

74 **1.1.2 Changes relative to v8**

- 75 • Included more references to appendices in the text
- 76 • Expanded explanation of fiducial region definition
- 77 • Previous draft claimed that both standard and custom PLVs were used. Text is fixed to
78 state that a custom PLV is used for lepton iso, but standard lepton id is used
- 79 • Included plots of PLV output, included WPs used
- 80 • specified that non-prompt CR plots are post correction
- 81 • changed title of results section

82 1.1.3 Changes relative to v7

- 83 • Moved from LO to NLO tZ sample
84 • Add additional plots of Z+jets and ttbar CRs in Section A.2
85 • Clarified CDI file used, MC ptag, PFlow jet algorithm
86 • Included overlap removal procedure
87 • Included details on PLV
88 • Added plots of missing tZ BDT input features for each fit region
89 • Changed reference on PLV to recent ttH/ttW note
90 • Included alternate fits with WZ+1-2 jet inclusive, tZ floating

91 1.1.4 Changes relative to v5

- 92 • added list of DSIDs to an appendix
93 • included systematics on jet migrations
94 • Updated results section to include simultaneous fit over 1-jet and 2-jet bins, describe
95 unfolding procedure
96 • Updated other sections to account for this change
97 • Included info about migrations in Section 5.2

98 1.1.5 Changes relative to v4

- 99 • Fixed various typos, clarified wording
100 • Expanded info about JER uncertainties, electron systematics, theory uncertainties
101 • removed a table on lepton selection, included information in the text instead
102 • Plotted lepton Pt Z and W for Zjet CR, rather than lep 1 and 2
103 • fixed binning in kinematic plots
104 • Included prefit and postfit yield tables
105 • added signal modelling systematics
106 • included alternate fit studies with tZ included in signal

107 **1.1.6 Changes relative to v3**

- 108 • Merged introduction into executive summary, including unblinding details and list of
- 109 SRs/CRs used
- 110 • listed ptag used (p4133), and release (AB 21.2.127)
- 111 • Included table reftab:xsecUnc listing x-sec uncertainties used
- 112 • Removed selection criteria listed in table ?? (QMisID, AmbiguityType) that were removed
- 113 from the analysis
- 114 • specified variable used to make truth jet flavor determination (HadronConeExclTruthLa-
- 115 belID)
- 116 • fixed bug in MtLepMet calculation, updated selection/fits to account for this
- 117 • Included plots of MtLepMet and PtZ, swapped lep 1 and 2 p_T plots for lep W and lep Z
- 118 plots
- 119 • updated tZ BDT training to reduce overfitting, updated plots to include error bars, feature
- 120 importance
- 121 • updated table 8 to clarify selection, fix the tZ_BDT cut used
- 122 • replace a few broken ntuples which included large weight events
- 123 • include DL1r distribution for Z+jets and tt} VRs
- 124 • Expanded section on fakes, included information on derived scale factors from VRs.
- 125 • Changed the kinematic plots to include $p_T(Z)$ and $m_T(W)$, list lepton p_T based on W and
- 126 Z candidates.

127 **1.1.7 Changes relative to v2**

- 128 • Added alternate VBS samples to include missing b-jet diagrams
- 129 • Included a section on tZ interference effects, ??.
- 130 • Updated to reflect changes for 2018, including the move to PFlow jets, DL1r, updated
- 131 trigger, and updated AnalysisBase version (now 21.2.127)
- 132 • Revised fit regions, using separate 1-jet and 2-jet fits, with all 2-j regions included
- 133 • updated plots for tZ BDT, added details about the model
- 134 • Included truth jet information

135 **1.1.8 Changes relative to v1**

- 136 • Added GRL list
137 • Fixed latex issue in line 92, typo in line 172
138 • Added tables 6 and ??, summarizing the event and object selection
139 • Added table 2, which includes the DSID of samples used
140 • Included reference to WZ inclusive paper in introduction

141 **1.2 Outstanding Items**

- 142 • Unblind, update plots and fits to include data
143 • Add cross-section, significance once unblinded

144 2 Executive Summary

145 The production of WZ in association with a heavy flavor jet represents an important background
 146 for many major analyses. This includes any process with multiple leptons and b-jets in the final
 147 state, such as $t\bar{t}H$, $t\bar{t}W$, and $t\bar{t}Z$. While precise measurements have been made of inclusive WZ
 148 production [1], $WZ +$ heavy flavor remains poorly understood. This is largely because the QCD
 149 processes involved in the production of the b-jet make it difficult to simulate accurately. This
 150 introduces a large uncertainty for analyses that include this process as a background.

151 We perform a study of the fully leptonic decay mode of this channel; that is, events where both
 152 the W and Z decay leptonically. Because WZ has no associated jets at leading order, while the
 153 major backgrounds for this channel tend to have high jet multiplicity, events with more than two
 154 jets are rejected. This gives a final state signature of three leptons and one or two jets.

155 Events that meet a preselection criteria are sorted into regions based on the b-tagging score of
 156 their associated jets. This is done to separate $WZ +$ b-jet events from $WZ +$ charm and $WZ +$
 157 light jets. These regions are fit to data in order to make a more accurate estimate of the contribution
 158 of $WZ +$ heavy-flavor, where heavy-flavor jets include b-jets and charm jets. The full Run-2
 159 dataset collected by the ATLAS detector, representing 139 fb^{-1} of data from pp collisions at
 160 $\sqrt{s} = 13 \text{ TeV}$, is used for this study.

161 The fiducial volume at particle level is defined based on the number of stable leptons and jets in
 162 each event. Three light leptons with total charge ± 1 and one or two associated jets are required.
 163 Only leptons which do not originate from hadron or τ decays are considered. The phase space
 164 definitions use dressed kinematics of the final state particles. Leptons are dressed by summing
 165 the momentum of photons within a cone of $\Delta R < 0.1$ of the lepton to correct the leptons energy.
 166 Particle level jets are reconstructed using the anti- k_t algorithm with a radius of $R = 0.4$. The
 167 kinematic selection applied to these objects is summarized below:

- 168 • Three light leptons with total charge ± 1 , $|\eta| < 2.5$
- 169 • OS lepton with $p_T > 10 \text{ GeV}$, SS leptons with $p_T > 20 \text{ GeV}$
- 170 • One OSSF lepton pair with $|M(l\bar{l}) - 91.2 \text{ GeV}| < 10 \text{ GeV}$
- 171 • One or two associated truth jets with $p_T > 25 \text{ GeV}$, $|\eta| < 2.5$, $R < 0.4$

172 The result of the fit is used to extract the cross-section in this fiducial region for $WZ + b$ and
 173 $WZ + c$ with one associated jet, and $WZ + b$ and $WZ + c$ with two associated jets, where the
 174 number and flavor of the jets is determined at particle level. Events with both charm and b-jets
 175 are counted as $WZ + b$. The analysis reports a cross-section measurement of $WZ + b$ and $WZ +$
 176 c , along with their correlations, for both 1-jet and 2-jet exclusive regions. Normalization factors,
 177 representing how the MC prediction differs from the observed result, are also reported.

178 Section 3 details the data and Monte Carlo (MC) samples used in the analysis. The reconstruction
 179 of various physics objects is described in Section 4. Section 6 describes the event selection applied
 180 to these samples, along the definitions of the various regions used in the fit. The multivariate

181 analysis techniques used to separate the tZ background from WZ + heavy flavor are described in
 182 Section 5. Section 7 describes the various sources of systematic uncertainties considered in the
 183 fit. Finally, the results of the analysis are summarized in Section 8, followed by a brief conclusion
 184 in Section 9.

185 **3 Data and Monte Carlo Samples**

186 Both data and Monte Carlo samples used in this analysis were prepared in the `xAOD` format,
 187 which was used to produce a `DxAOD` sample in the HIGG8D1 derivation framework. The HIGG8D1
 188 framework is designed for the $t\bar{t}H$ multi-lepton analysis, which targets events with multiple
 189 leptons as well as tau hadrons. This framework reduces the size of the dataset by removing
 190 events based on event topology and only keeping useful information for each event. Events are
 191 removed from the derivations that do not meet one of the following selections:

- 192 • at least two light leptons within a range $|\eta| < 2.6$, with leading lepton $p_T > 15$ GeV and
 193 subleading lepton $p_T > 5$ GeV
- 194 • OR at least one light lepton with $p_T > 15$ GeV within a range $|\eta| < 2.6$, and at least two
 195 hadronic taus with $p_T > 15$ GeV.

196 Samples were then generated from these HIGG8D1 derivations with p-tag of p4134 for data
 197 and p4133 for Monte Carlo using AnalysisBase version 21.2.127 modified to include custom
 198 variables.

199 **3.1 Data Samples**

200 The study uses a sample of proton-proton collision data collected by the ATLAS detector from
 201 2015 through 2018 at an energy of $\sqrt{s} = 13$ TeV, which represents an integrated luminosity of
 202 139 fb^{-1} [2]. This data set was collected with a bunch-crossing rate of 25 ns. All data used in
 203 this analysis was verified by data quality checks [3], having been included in the following Good
 204 Run Lists:

- 205 • `data15_13TeV.periodAllYear_DetStatus-v79-repro20-02_DQDefects-00-02-02`
 206 `_PHYS_StandardGRL_All_Good_25ns.xml`
- 207 • `data16_13TeV.periodAllYear_DetStatus-v88-pro20-21_DQDefects-00-02-04`
 208 `_PHYS_StandardGRL_All_Good_25ns.xml`
- 209 • `data17_13TeV.periodAllYear_DetStatus-v97-pro21-13_Uncknown_PHYS_StandardGRL`
 210 `_All_Good_25ns_Triggerno17e33prim.xml`
- 211 • `data18_13TeV.periodAllYear_DetStatus-v102-pro22-04_Uncknown_PHYS_StandardGRL`
 212 `_All_Good_25ns_Triggerno17e33prim.xml`

213 Runs included from the AllYear period containers are included.

214 **3.2 Monte Carlo Samples**

215 Several different generators were used to produce Monte Carlo simulations of the signal and
216 background processes. For all samples, the response of the ATLAS detector is simulated using
217 GEANT4 [4]. The WZ signal samples are simulated using Sherpa 2.2.2 [5]. Signal events are
218 generated using NNPDF30NNLO PDF set with up to one parton at NLO and 2 to 3 partons at
219 LO [**Butterworth:2015oua**].

220 The tZ background is simulated at NLO with **MADGRAPH5_AMC@NLO**, with PYTHIA8 used to
221 perform parton showering and fragmentation. The NNPDF30NNLO PDF set is used.

222 Specific information about the Monte Carlo samples being used can be found in Table 1. A list
223 of the specific samples used by data set ID is shown in Table 2.

Table 1: The configurations used for event generation of signal and background processes, including the event generator, matrix element (ME) order, parton shower algorithm, and parton distribution function (PDF).

Process	Event generator	ME order	Parton Shower	PDF
WZ, VV	SHERPA 2.2.2	MEPS NLO	SHERPA	CT10 [6]
tZ	MG5_AMC [7]	NLO	PYTHIA 8	CTEQ6L1
t̄W	MG5_AMC (SHERPA 2.1.1)	NLO (LO multileg)	PYTHIA 8 (SHERPA)	NNPDF 3.0 NLO (NNPDF 3.0 NLO)
t̄t(Z/γ* → ll)	MG5_AMC	NLO	PYTHIA 8	NNPDF 3.0 NLO
t̄tH	MG5_AMC (MG5_AMC)	NLO (NLO)	PYTHIA 8 (HERWIG++) [9]	NNPDF 3.0 NLO [8] (CT10 [6])
tHqb	MG5_AMC	LO	PYTHIA 8	CT10
tHW	MG5_AMC (SHERPA 2.1.1)	NLO (LO multileg)	HERWIG++ (SHERPA)	CT10 (NNPDF 3.0 NLO)
tWZ	MG5_AMC	NLO	PYTHIA 8	NNPDF 2.3 LO
t̄t̄, t̄t̄t̄	MG5_AMC	LO	PYTHIA 8	NNPDF 2.3 LO [10]
t̄tW+W-	MG5_AMC	LO	PYTHIA 8	NNPDF 2.3 LO
t̄t	POWHEG-BOX v2 [11]	NLO	PYTHIA 8	NNPDF 3.0 NLO
t̄t̄γ	MG5_AMC	LO	PYTHIA 8	NNPDF 2.3 LO
s-, t-channel, Wt single top	POWHEG-BOX v1 [12]	NLO	PYTHIA 6	CT10
qqVV, VVV Z → l+l-	SHERPA 2.2.1	MEPS NLO	SHERPA	NNPDF 3.0 NLO

Sample	DSID
WZ	364253, 364739-42
VV	364250, 364254, 364255, 363355-60, 364890
t̄W	410155
t̄Z	410156, 410157, 410218-20
low mass t̄Z	410276-8
Rare Top	410397, 410398, 410399
single Top	410658-9, 410644-5
three Top	304014
four Top	410080
t̄WW	410081
Z + jets	364100-41
low mass Z + jets	364198-215
W + jets	364156-97
Vγ	364500-35
tZ	412063-5
tW	410013-4
WtZ	410408
VVV	364242-9
VH	342284-5
WtH	341998
t̄tγ	410389
t̄t	410470
t̄tH	345873-5, 346343-5

Table 2: List of Monte Carlo samples by data set ID used in the analysis.

224 4 Object Reconstruction

225 All regions defined in this analysis share a common lepton, jet, and overall event preselection.
 226 The selection applied to each physics object is detailed here; the event preselection, and the
 227 selection used to define the various fit regions, is described in Section 6.

228 4.1 Trigger

229 Events are required to be selected by dilepton triggers, as summarized in Table 3.

Dilepton triggers (2015)	
$\mu\mu$ (asymm.)	HLT_mu18_mu8noL1
ee (symm.)	HLT_2e12_lhloose_L12EM10VH
$e\mu, \mu e$ (\sim symm.)	HLT_e17_lhloose_mu14
Dilepton triggers (2016)	
$\mu\mu$ (asymm.)	HLT_mu22_mu8noL1
ee (symm.)	HLT_2e17_lhvloose_nod0
$e\mu, \mu e$ (\sim symm.)	HLT_e17_lhloose_nod0_mu14
Dilepton triggers (2017)	
$\mu\mu$ (asymm.)	HLT_mu22_mu8noL1
ee (symm.)	HLT_2e24_lhvloose_nod0
$e\mu, \mu e$ (\sim symm.)	HLT_e17_lhloose_nod0_mu14
Dilepton triggers (2018)	
$\mu\mu$ (asymm.)	HLT_mu22_mu8noL1
ee (symm.)	HLT_2e24_lhvloose_nod0
$e\mu, \mu e$ (\sim symm.)	HLT_e17_lhloose_nod0_mu14

Table 3: List of lowest p_T -threshold, un-prescaled dilepton triggers used for 2015–2018 data taking.

4.2 Light leptons

Electron candidates are reconstructed from energy clusters in the electromagnetic calorimeter that are associated with charged particle tracks reconstructed in the inner detector [13]. Electron candidates are required to have $p_T > 10$ GeV and $|\eta_{\text{cluster}}| < 2.47$. Muon candidates are reconstructed by combining inner detector tracks with track segments or full tracks in the muon spectrometer [14]. Muon candidates are required to have $p_T > 10$ GeV and $|\eta| < 2.5$. Candidates in the transition region between different electromagnetic calorimeter components, $1.37 < |\eta_{\text{cluster}}| < 1.52$, are rejected. A multivariate likelihood discriminant combining shower shape and track information is used to distinguish real electrons from hadronic showers (fake electrons). To further reduce the non-prompt electron contribution, the track is required to be consistent with originating from the primary vertex; requirements are imposed on the transverse impact parameter significance ($|d_0|/\sigma_{d_0} < 5$) and the longitudinal impact parameter ($|\Delta z_0 \sin \theta_\ell| < 0.5$ mm). Electron candidates are required to pass TightLH identification.

Muon candidates are reconstructed by combining inner detector tracks with track segments or full tracks in the muon spectrometer [14]. Muon candidates are required to have $p_T > 10$ GeV and $|\eta| < 2.5$. The longitudinal impact parameter is the same for both electrons and muons, while muons are required to pass a slightly tighter transverse impact parameter, $|d_0|/\sigma_{d_0} < 3$. Muons are also required to pass Medium ID requirements.

248 Leptons are additionally required to pass a non-prompt BDT selection developed by the $t\bar{t}H$
249 multilepton/ $t\bar{t}W$ analysis group. This BDT and the WPs used are summarized in Appendix A.1,
250 and described in detail in [15]. Optimized working points and scale factors for this BDT are
251 taken from that analysis.

252 **4.3 Jets**

253 Jets are reconstructed from calibrated topological clusters built from energy deposits in the
254 calorimeters [16], as well as information from the inner tracking detector, using the anti- k_t
255 algorithm with a radius parameter $R = 0.4$. Particle Flow, or PFlow, jets are used in the analysis.
256 Jets with energy contributions likely arising from noise or detector effects are removed from
257 consideration [17], and only jets satisfying $p_T > 25$ GeV and $|\eta| < 2.5$ are used in this analysis.
258 For jets with $p_T < 60$ GeV and $|\eta| < 2.4$, a jet-track association algorithm is used to confirm
259 that the jet originates from the selected primary vertex, in order to reject jets arising from pileup
260 collisions [18].

261 **4.4 B-tagged Jets**

262 In order to make a measurement of $WZ +$ heavy flavor it is necessary to distinguish these events
263 from $WZ +$ light jets. For this purpose, the DL1r b-tagging algorithm is used to distinguish
264 heavy flavor jets from lighter ones. The DL1r algorithm [19] uses jet kinematics, particularly
265 jet vertex information, as input for a neural network which assigns each jet a score designed to
266 reflect how likely that jet is to have originated from a b-quark.

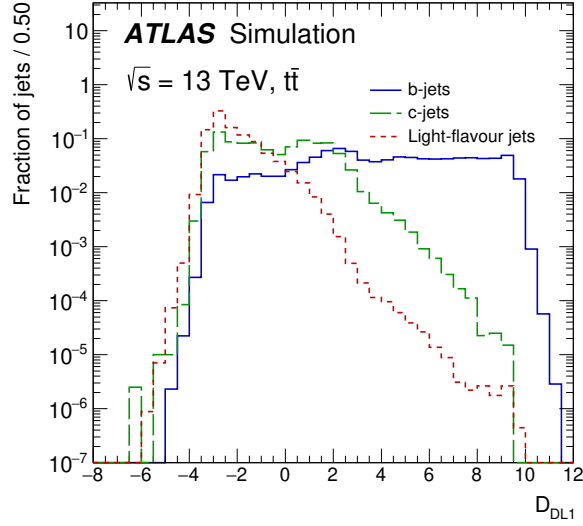


Figure 1: Output distribution of the DL1r algorithm for pure samples of b-jets, charm jets, and light jets, with each normalized to unity [19]

From the output of the BDT, working points (WPs) are developed based on the efficiency of truth b-jets at particular values of the DL1r algorithm. These WPs are taken from the March 2020 CDI file, 2020-21-13TeV-MC16-CDI-2020-03-11_v2.root. The working points used in this analysis are summarized in Table 4.

WP	Rejection		
	b-jet eff.	c-jet	light jet
85%	2.6	29	
77%	4.9	130	
70%	9.4	390	
60%	27	1300	

Table 4: c-jet and light-flavor jet rejections corresponding to each b-tagging Working Point by b-jet efficiency, evaluated on $t\bar{t}$ events.

As shown in table 4, a tighter WP will accept fewer b-jets, but reject a higher fraction of charm and light jets. Generally, analyses that include b-jets will use a fixed working point, for example, requiring that a jet pass the 70% threshold. By instead treating these working points as bins, e.g. events with jets that fall between the 85% and 77% WPs fall into one bin, while events with jets passing the 60% WP fall into another, additional information can be gained. This analysis uses each of these working points to form orthogonal regions in order to provide separation between $WZ + b$, $WZ + c$, and $WZ + \text{light}$.

278 **4.5 Missing transverse energy**

279 Missing transverse momentum (E_T^{miss}) is used as part of the event selection. The missing
 280 transverse momentum vector is defined as the negative of the vector sum of the transverse
 281 momenta of all reconstructed physics objects as well as remaining unclustered energy, the latter
 282 of which is estimated from low- p_T tracks associated with the primary vertex but not assigned
 283 to a hard object, with object definitions taken from [20]. Light leptons considered in the E_T^{miss}
 284 reconstruction are required to have $p_T > 10 \text{ GeV}$, while jets are required to have $p_T > 20 \text{ GeV}$.

285 **4.6 Overlap removal**

286 To avoid double counting objects and remove leptons originating from decays of hadrons, overlap
 287 removal is performed in the following order: any electron candidate within $\Delta R = 0.1$ of another
 288 electron candidate with higher p_T is removed; any electron candidate within $\Delta R = 0.1$ of a muon
 289 candidate is removed; any jet within $\Delta R = 0.2$ of an electron candidate is removed; if a muon
 290 candidate and a jet lie within $\Delta R = \min(0.4, 0.04 + 10[\text{GeV}]/p_T(\text{muon}))$ of each other, the jet
 291 is kept and the muon is removed if the jet has at least three associated tracks, otherwise the jet is
 292 removed and the muon is kept.

293 This algorithm is applied to the preselected objects. The overlap removal procedure is summarized
 294 in Table 5.

Keep	Remove	Cone size (ΔR)
electron	electron (low p_T)	0.1
muon	electron	0.1
electron	jet	0.2
jet	muon	$\min(0.4, 0.04 + 10[\text{GeV}]/p_T(\text{muon}))$, $n_{\text{track}} > 3$
muon	jet	$\min(0.4, 0.04 + 10[\text{GeV}]/p_T(\text{muon}))$, $n_{\text{track}} < 3$
electron	tau	0.2

Table 5: Summary of the overlap removal procedure between electrons, muons, and jets.

295 **5 tZ Separation Multivariate Analysis**

296 Because tZ produces a final state identical to signal, it represents a predominant background in
 297 the most signal enriched regions. That is, the region with one jet passing the 60% DL1r WP.
 298 Therefore, a boosted decision tree (BDT) algorithm is trained to separate WZ + heavy flavor
 299 from tZ.

300 Separation between tZ and WZ + heavy flavor is achieved in part by reconstructing the invariant
 301 mass of the top candidate, which clusters more closely to the top mass for tZ than WZ + heavy

302 flavor. The result of this BDT is used to create a tZ enriched region in the fit, reducing its impact
 303 on the measurement of WZ + heavy flavor.

304 **5.1 Top Mass Reconstruction**

305 The reconstruction of the top mass follows the procedure described in detail in section 6.1 of
 306 [21]. The mass of the top quark candidate is reconstructed from the jet, the lepton not included
 307 in the Z-candidate, and a reconstructed neutrino. In the case that there is one jet in the event,
 308 there is only possible b-jet candidate. For events with two jets, the jet with the highest DL1r
 309 score is used.

310 The neutrino from the W decay is expected to be the only source of E_T^{miss} . Therefore, the E_T
 311 and ϕ of the neutrino are taken from the E_T^{miss} measurement. This leaves the z-component of
 312 the neutrino momentum, $p_{\nu z}$ as the only unknown.

313 This unknown is solved for by taking the combined invariant mass of the lepton and neutrino to
 314 give the invariant mass of the W boson:

$$315 \quad (p_l + p_\nu)^2 = m_W^2$$

316 Expanding this out into components, this equation gives:

$$317 \quad \sqrt{p_{T\nu}^2 + p_{z\nu}^2} E_l = \frac{m_W^2 - m_l^2}{2} + p_{T\nu}(p_{lx}\cos\phi_\nu + p_{ly}\sin\phi_\nu) + p_{lz}p_{\nu z}$$

318 This equation gives two solutions for $p_{\nu z}$. For cases where only one of these solutions is real,
 319 that is taken as the value of $p_{\nu z}$. For instances with two real solutions, the one which is shown
 320 to be correct in the largest fraction of simulations is taken. For cases when no real solution is
 321 found, often because of detector effects, the value of E_T^{miss} is varied in decreasing increments of
 322 100 MeV until a real solution is found.

323 The reconstructed top mass distribution for tZ and WZ + b can be seen in figure 2.

324 **5.2 tZ BDT**

325 A Boosted Decision Tree (BDT), specifically XGBoost [22], is used to provide separation between
 326 tZ and WZ+b. The following kinematic variables are used as inputs:

- 327 • The invariant mass of the reconstructed top candidate
- 328 • p_T of each of the leptons, jet
- 329 • The invariant mass of each combination of lepton pairs, $M(l\bar{l})$

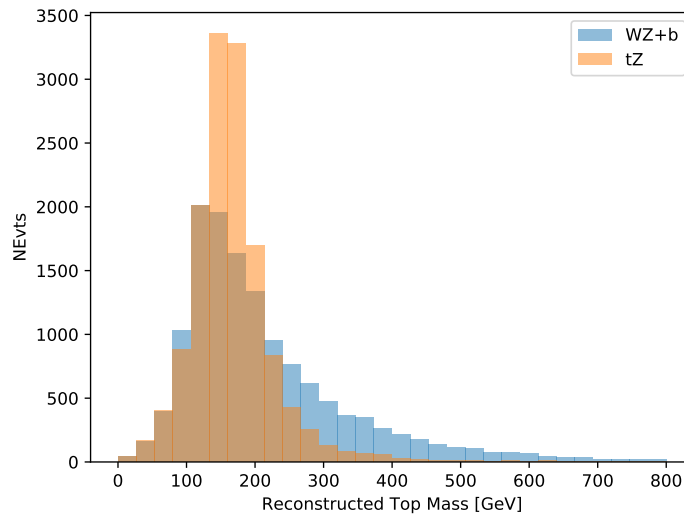


Figure 2: Reconstructed top mass distributions for tZ and WZ + b, measured in MeV.

330 • E_T^{miss}

331 • Distance between each combination of leptons, $\Delta R(ll)$

332 • Distance between each lepton and the jet, $\Delta R(lj)$

333 The training samples included only events meeting the requirements of the 1-jet, >60% region,
 334 i.e. passing all the selection described in section 6 and having exactly one jet which passes the
 335 tightest (60%) DL1r working point.

336 The distributions of a few of these features for both signal and background is shown in figure
 337 3.

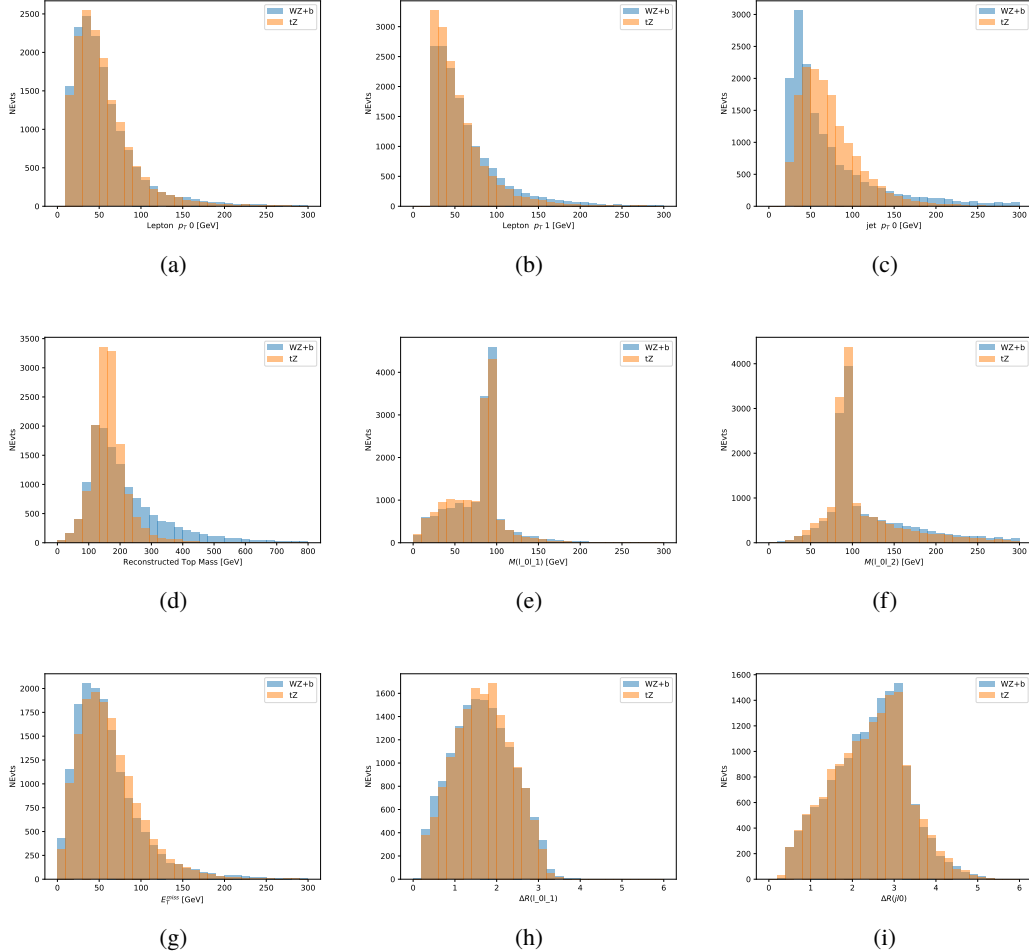


Figure 3: Distribution of input features of the BDT for signal (WZ) and background (tZ). Both are scaled to an equal number of events. (a), (b) and (c) show the p_T of lepton 0, lepton 1, and the jet, (d) show the reconstructed top mass, (e) and (f) show the invariant mass of leptons 0 and 1, leptons 0 and 2. (g) shows the E_T^{miss} of each event. (h) and (i) show the ΔR between lepton 0 and lepton 1, and the jet.

338 A sample of 20,000 background (tZ) and signal (WZ+b) Monte Carlo events are used to train
 339 the BDT. And additional 5,000 events are reserved for testing the model, in order to prevent
 340 over-fitting. A total of 750 decision trees with a maximum depth of 6 branches are used to build
 341 the model. These parameters are chosen empirically, by training several models with different
 342 parameters and selecting the one that gave the best separation for the test sample.

343 The results of the BDT training are shown in figure 4. The output scores for both signal and
 344 background events is shown on the left. The right shows the receiving operating characteristic
 345 (ROC) curve that results from the MVA. The ROC curve represents the background rejection
 346 as a function of signal efficiency, where each point on the curve represents a different response

347 score.

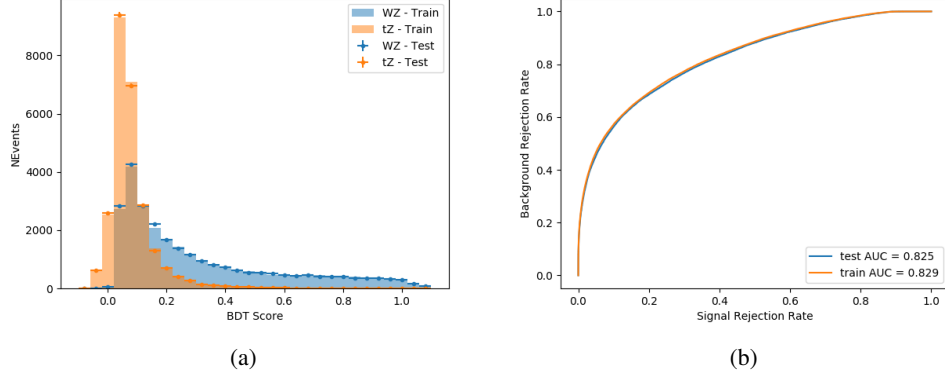


Figure 4: Distribution of the BDT response for signal and background events on the left, the ROC curve for the BDT on the right.

348 The relative important of each input feature in the model, measured by how often they appeared
 349 in the decision trees, is shown in figure 5.

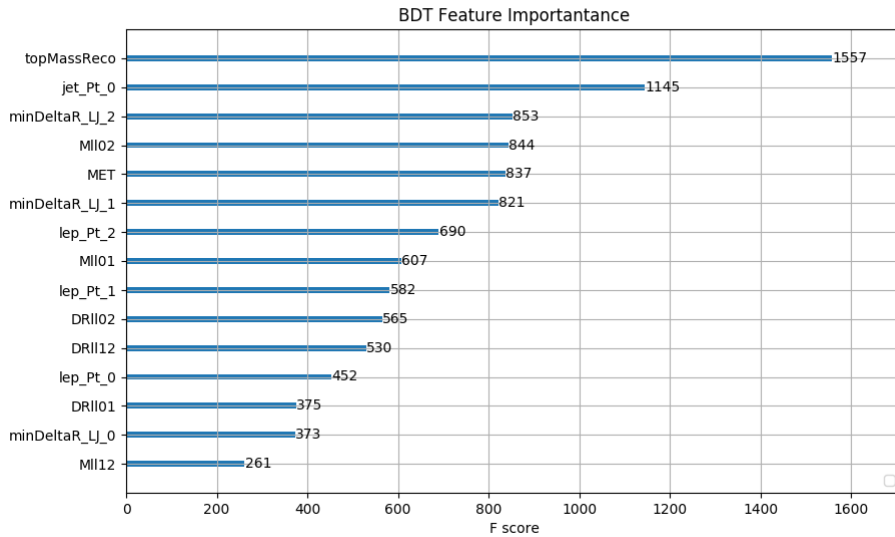


Figure 5: Relative importance of each input feature in the model.

350 These results suggest that some amount of separation can be achieved between these two pro-
 351 cesses, with a high BDT score selecting a set of events that is pure in WZ + b. A BDT score

of 0.12 is selected as a cutoff, where events with scores higher than this form a signal enriched region, and events with scores lower than this form a tZ control region. This cutoff is selected by varying the value of this cutoff in stat-only Asimov fits, and selecting the value that minimizes the statistical uncertainty on WZ + b. A working point of 0.12 produces a background rejection rate of 74%, compared to a signal acceptance of 78%.

5.3 tZ Interference Studies

Because it includes an on-shell Z boson as well as a b-jet and W from the top decay, tZ production represents an identical final state to WZ + b-jet. This implies the possibility of matrix level interference between these two processes not accounted for in the Monte Carlo simulations, which consider the two processes independently. Truth level studies are performed in order to estimate the impact of these interference effects.

In order to estimate the matrix level interference effects between tZ and WZ + b-jet, two different sets of simulations are produced using MadGraph 5 [23] - one which simulates these two processes independently, and another where they are produced simultaneously, such that interference effects are present. These two sets of samples are then compared, and the difference between them can be taken to represent any interference effects.

MadGraph simulations of 10,000 tZ and 10,000 WZ + b-jet events are produced, along with 20,000 events where both are present, in the fiducial region where three leptons and at least one jet are produced.

A selection mimicking the preselection used in the main analysis is applied to the samples: The SS leptons are required to have $p_T > 20$ GeV, and > 10 GeV is required for the OS lepton. The associated b-jet is required to have $p_T > 25$ GeV, and all physics objects are required to fall in a range of $|\eta| < 2.5$.

The kinematics of these samples after the selection has been applied are shown below:

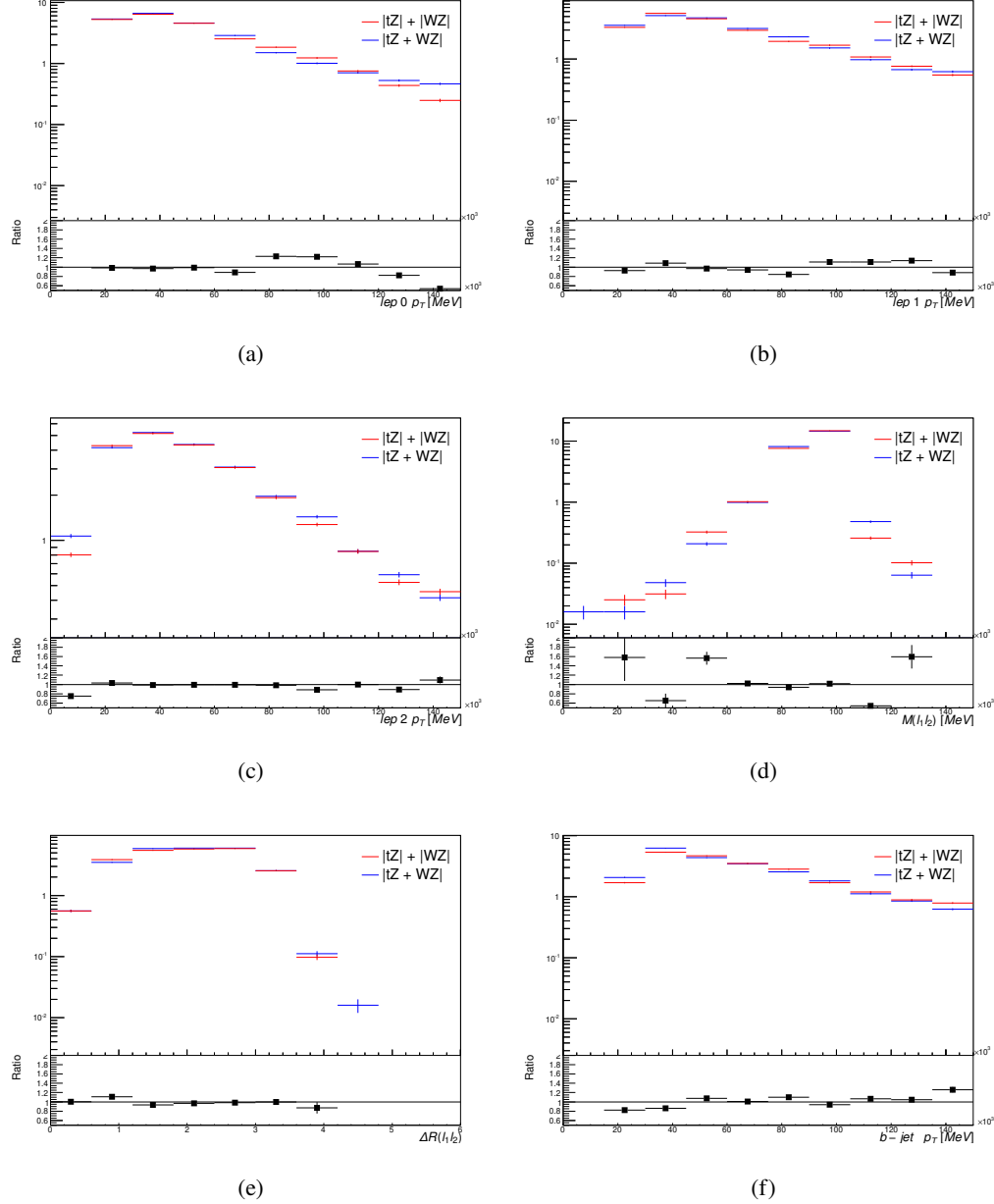


Figure 6: Comparisons between (a) the p_T of the lepton from the W, (b) and (c) show the p_T of the lepton from the Z, (d) the invariant mass of the Z-candidate, (e) ΔR of the leptons from the Z, and (f) the p_T of the b-jet, for WZ and tZ events generated with interference effects (blue) and without interference effects (red).

376 The overall cross-section of the two methods agree within error, and no significant differences
 377 in the kinematic distributions are seen. It is therefore concluded that interference effects do not

³⁷⁸ significantly impact the results.

³⁷⁹ 6 Event Selection and Signal Region Definitions

³⁸⁰ Event are required to pass a preselection described in Section 6.1 and summarized in Table 6.
³⁸¹ Those that pass this preselection are divided into various fit regions described in Section 6.2,
³⁸² based on the number of jets in the event, and the b-tag score of those jets.

³⁸³ 6.1 Event Preselection

³⁸⁴ Events are required to include exactly three reconstructed light leptons passing the requirement
³⁸⁵ described in 4.2, which have a total charge of ± 1 .

³⁸⁶ The leptons are ordered in the analysis code as 0, 1, and 2. Lepton 0 is the lepton whose charge
³⁸⁷ is opposite the other two. Lepton 1 is the lepton closest to the opposite charge lepton, i.e. the
³⁸⁸ smallest ΔR , leaving lepton 2 as the lepton further from the opposite charge lepton. Lepton 0 is
³⁸⁹ required to have $p_T > 10$ GeV, as it is found to be prompt the vast majority of the time, while
³⁹⁰ the same sign leptons, 1 and 2, are required to have $p_T > 20$ GeV to reduce the contribution of
³⁹¹ non-prompt leptons, as non-prompt leptons tend to be soft.

³⁹² The invariant mass of at least one pair of opposite sign, same flavor leptons is required to fall
³⁹³ within 10 GeV of the mass of the Z boson, 91.2 GeV. Events where one of the opposite sign pairs
³⁹⁴ have an invariant mass less than 12 GeV are rejected in order to suppress low mass resonances.

³⁹⁵ An additional requirement is placed on the missing transverse energy, $E_T^{\text{miss}} > 20$ GeV, and the
³⁹⁶ transverse mass of the W candidate, $m(E_T^{\text{miss}} + l_{\text{other}}) > 30$ GeV, defined as

³⁹⁷ $\sqrt{2p_T^{\text{lep}} E_T^{\text{miss}} * (1 - \cos(\phi_{\text{lep}} - \phi_{E_T^{\text{miss}}}))}$. Here E_T^{miss} is the missing transverse energy, and
³⁹⁸ l_{other} is the lepton not included in the Z-candidate.

³⁹⁹ Events are required to have one or two reconstructed jets passing the selection described in
⁴⁰⁰ Section 4.3. Events with more than two jets are rejected in order to reduce the contribution of
⁴⁰¹ backgrounds such as $t\bar{t}Z$ and $t\bar{t}W$, which tend to have higher jet multiplicity.

Event Selection
Exactly three leptons with total charge ± 1
Two same-charge leptons with $p_T > 20$ GeV
One opposite charge lepton with $p_T > 10$ GeV
$m(l^+l^-)$ within 10 GeV of 91.2 GeV
Transverse mass of W-candidate, $\sqrt{2p_T^{lep}E_T^{\text{miss}} * (1 - \cos(\phi_{lep} - \phi_{E_T^{\text{miss}}}))} > 30$ GeV
Missing transverse energy, $E_T^{\text{miss}} > 20$ GeV
One or two jets with $p_T > 25$ GeV

Table 6: Summary of the selection applied to events for inclusion in the fit

402 The event yields in the preselection region for both data and Monte Carlo are summarized in
 403 Table 6.1, which shows good agreement between data and Monte Carlo, and demonstrates that
 404 this region consists primarily of WZ + jets events. The WZ events are split into WZ + b, WZ
 405 + c, and WZ + l based on the truth flavor of the associated jet in the event. Specifically, this
 406 determination is made based on the HadronConeExclTruthLabelID of the jet, as recommended
 407 by the b-tagging working group [24]. In this ordering b-jet supersedes charm, which supersedes
 408 light. That is, WZ + light events contain no charm and no b jets at truth level, WZ + c contain at
 409 least one truth charm and no b-jets, and WZ + b contains at least one truth b-jet.

Process	Events
WZ + b	167.6 ± 6.5
WZ + c	1080 ± 40
WZ + l	7220 ± 310
Other VV	850 ± 140
t̄tW	16.8 ± 2.3
t̄tZ	115 ± 17
rare Top	2.2 ± 0.1
Single top	0.10 ± 0.45
Three top	0.01 ± 0.01
Four top	0.02 ± 0.01
t̄tWW	0.23 ± 0.05
Z + jets	600 ± 260
V + γ	37 ± 54
tZ	190 ± 70
tW	5.5 ± 1.2
WtZ	25.8 ± 1.1
VVV	26.2 ± 0.9
VH	94 ± 7
t̄t	108.68 ± 8
t̄tH	4.3 ± 0.5
Total	10600 ± 530
Data	10574

Table 7: Event yields in the preselection region at 139.0 fb^{-1}

⁴¹⁰ Here Other VV represents diboson processes other than WZ, and consists predominantly of
⁴¹¹ ZZ → ll̄ll events where one of the leptons is not reconstructed.

⁴¹² Simulations are further validated by comparing the kinematic distributions of the Monte Carlo
⁴¹³ with data, which are shown in Figure 7. Here, bins with 5% or more WZ+b are blinded.

WZ Fit Region - Inclusive

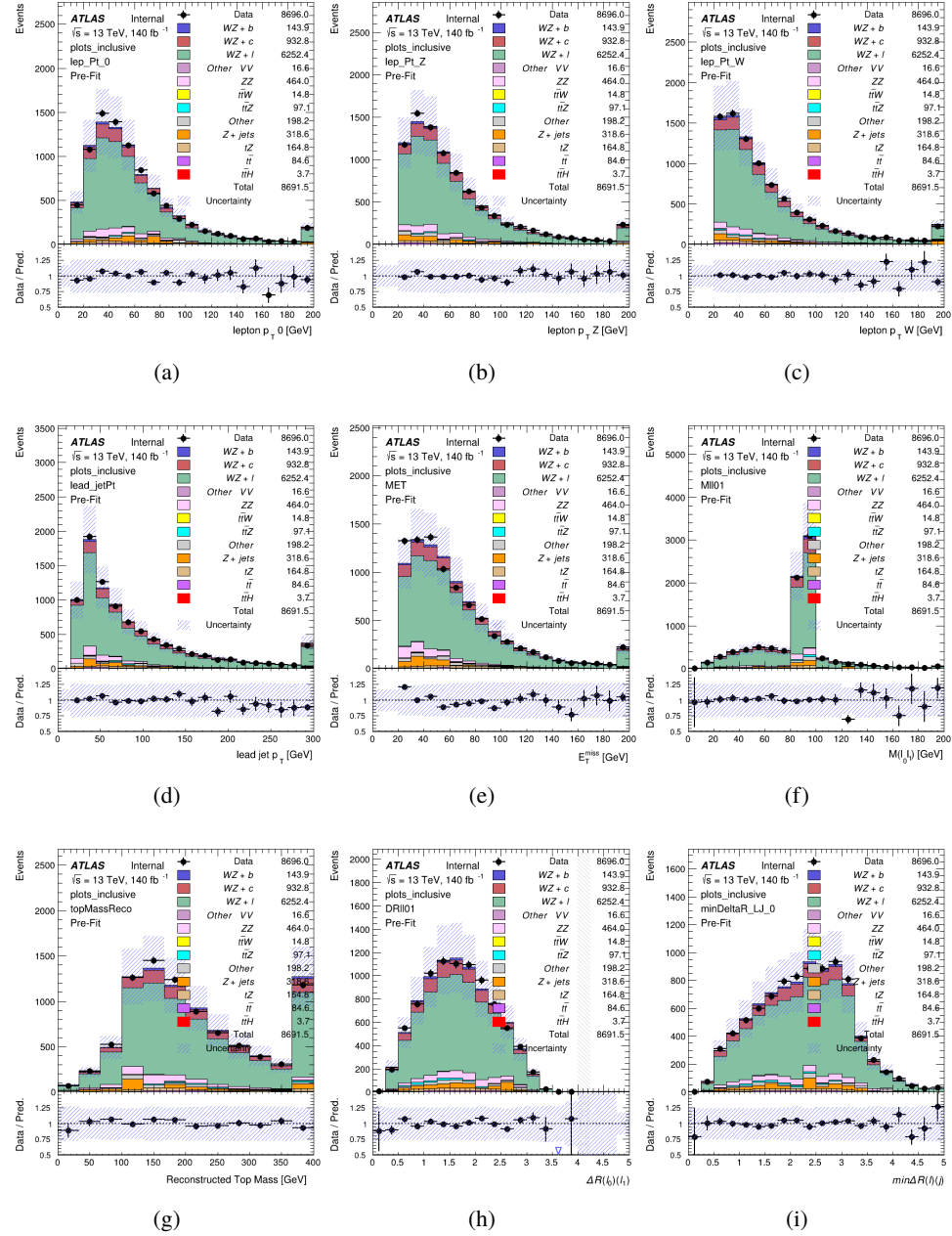


Figure 7: Comparisons between the data and MC distributions in the preselection region for (a) the p_T of the opposite sign lepton, (b) the p_T of the other lepton from the Z candidate, (c) the p_T of the lepton from the W candidate, (d) the leading jet p_T , (e) the E_T^{miss} , and (f) the invariant mass of leptons 0 and 1, (g) the reconstructed top mass, (h) $\Delta(R)$ between lepton 0 and 1, (i) the $\Delta(R)$ between the closest lepton and jet.

⁴¹⁴ **6.2 Fit Regions**

⁴¹⁵ Once preselection has been applied, the remaining events are categorized into one of twelve
⁴¹⁶ orthogonal regions. The regions used in the fit are summarized in Table 8.

Table 8: A list of the regions used in the fit and the selection used for each.

Region	Selection
1j, <85%	$N_{\text{jets}} = 1, n_{\text{Jets_DL1r_85}} = 0$
1j, 85%-77%	$N_{\text{jets}} = 1, n_{\text{Jets_DL1r_85}} = 1, n_{\text{Jets_DL1r_77}} = 0$
1j, 77%-70%	$N_{\text{jets}} = 1, n_{\text{Jets_DL1r_77}} = 1, n_{\text{Jets_DL1r_70}} = 0$
1j, 70%-60%	$N_{\text{jets}} = 1, n_{\text{Jets_DL1r_70}} = 1, n_{\text{Jets_DL1r_60}} = 0$
1j, >60%	$N_{\text{jets}} = 1, n_{\text{Jets_DL1r_60}} = 1, tZ \text{ BDT} > 0.12$
1j tZ CR	$N_{\text{jets}} = 1, n_{\text{Jets_DL1r_60}} = 1, tZ \text{ BDT} < 0.12$
2j, <85%	$N_{\text{jets}} = 2, n_{\text{Jets_DL1r_85}} = 0$
2j, 85%-77%	$N_{\text{jets}} = 2, n_{\text{Jets_DL1r_85}} \geq 1, n_{\text{Jets_DL1r_77}} = 0$
2j, 77%-70%	$N_{\text{jets}} = 2, n_{\text{Jets_DL1r_77}} \geq 1, n_{\text{Jets_DL1r_70}} = 0$
2j, 70%-60%	$N_{\text{jets}} = 2, n_{\text{Jets_DL1r_70}} \geq 1, n_{\text{Jets_DL1r_60}} = 0$
2j, >60%	$N_{\text{jets}} = 2, n_{\text{Jets_DL1r_60}} \geq 1, tZ \text{ BDT} > 0.12$
2j tZ CR	$N_{\text{jets}} = 2, n_{\text{Jets_DL1r_60}} \geq 1, tZ \text{ BDT} < 0.12$

⁴¹⁷ The working points discussed in Section 4.4 are used to separate events into fit regions based on
⁴¹⁸ the highest working point reached by a jet in each event. Because the background composition
⁴¹⁹ differs significantly based on the number of b-jets, events are further subdivided into 1-jet and
⁴²⁰ 2-jet regions in order to minimize the impact of background uncertainties.

⁴²¹ An unfolding procedure is performed to account for differences in the number of reconstructed
⁴²² jets compared to the number of truth jets in each event. The `AntiKt4TruthDressedWZJets`
⁴²³ truth jet collection is used to make this determination. In order to account for migration of
⁴²⁴ WZ+1-jet and WZ+2-jet events between the 1-jet and 2-jet bins at reco level, the signal samples
⁴²⁵ are separated based on the number of truth jets. Events with 0 jets or more than 3 jets at truth
⁴²⁶ level, yet fall within one of the categories listed in Table 8, are categorized as WZ + other, and
⁴²⁷ treated as a background. The migration matrix in the number of jets at truth level versus reco
⁴²⁸ level is shown in Figure 8. The composition of the number of truth jets in each reco jet bin is
⁴²⁹ taken from MC, with uncertainties in these estimates described in detail in Section 7.

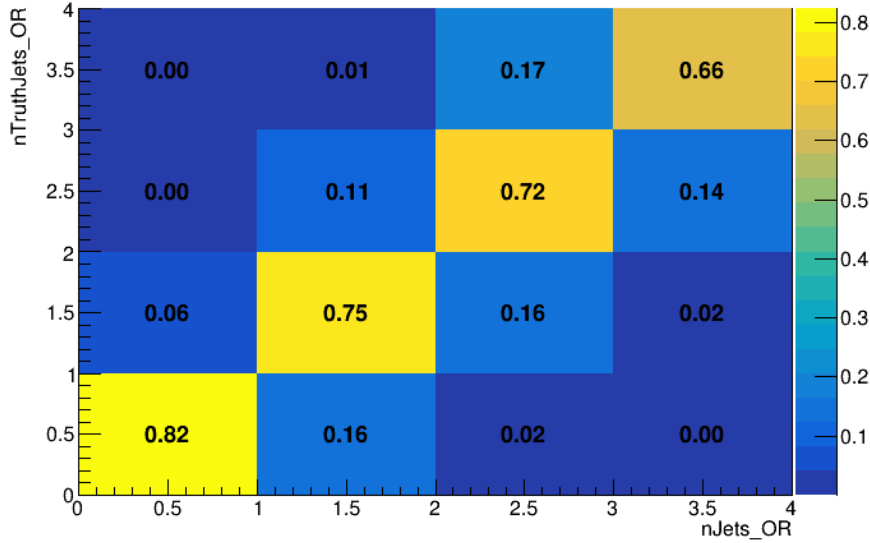


Figure 8: Number of truth jets compared to the number of reconstructed jets in each WZ event falling in the preselection region. Each row is normalized to unity.

- 430 An additional tZ control region is created based on the BDT described in Section 5. The region
 431 with 1-jet passing the 60% working point is split in two - a signal enriched region of events with
 432 a BDT score greater than 0.12, and a tZ control region including events with a score less than
 433 0.12. This cutoff is arrived at by performing a fit an Asimov dataset with a variety of cutoffs,
 434 and selecting the value that produces the highest significance for the measurement of WZ + b.
 435 The modeling in each region is validated by comparing data and MC predictions for various
 436 kinematic distributions. Events containing 5% or more WZ + b are blinded. These plot are
 437 shown in Figures 9-22.

WZ Fit Region - 1j Inclusive

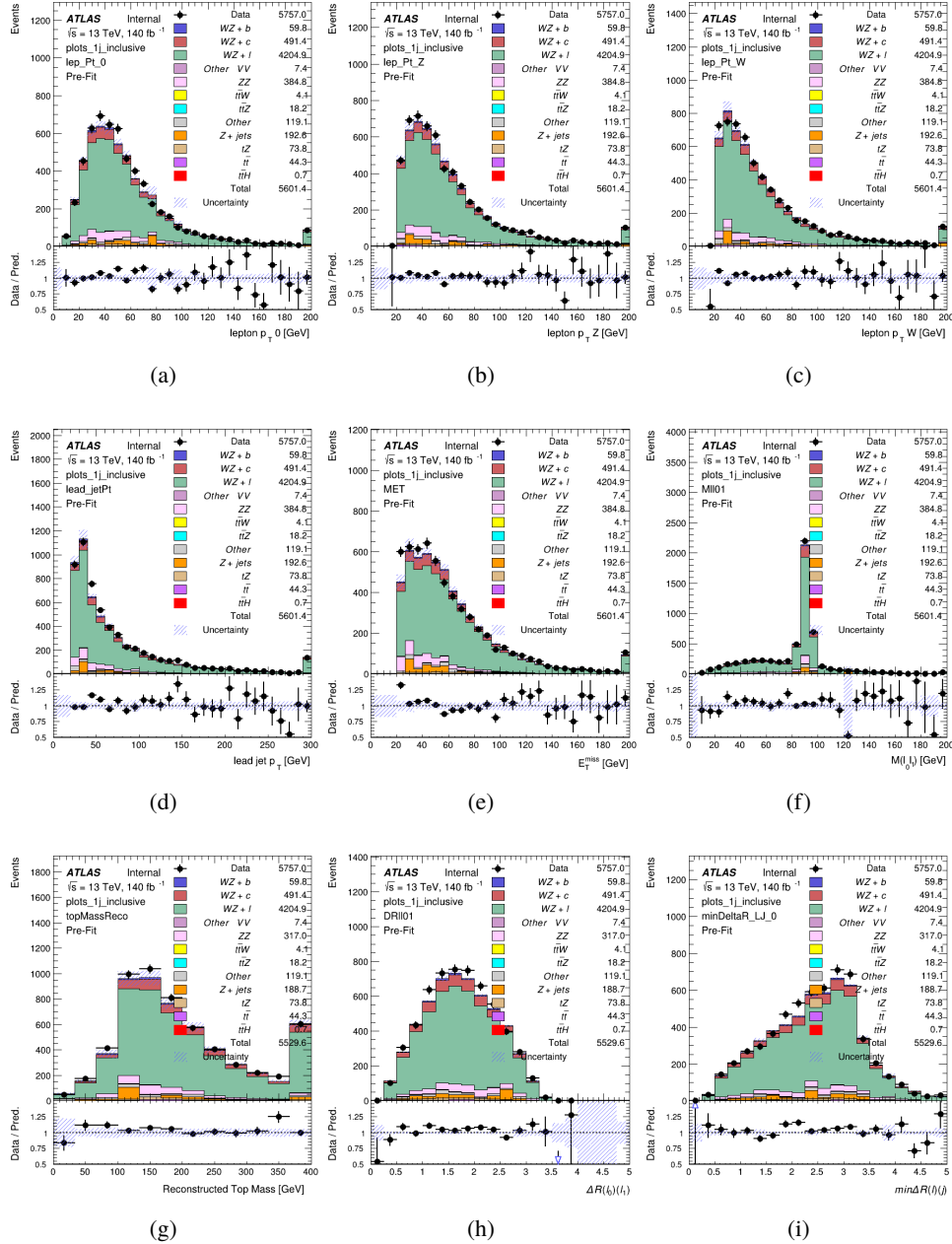


Figure 9: Comparisons between the data and MC distributions in the preselection region for (a) the p_T of the opposite sign lepton, (b) the p_T of the other lepton from the Z candidate, (c) the p_T of the lepton from the W candidate, (d) the leading jet p_T , (e) the E_T^{miss} , and (f) the invariant mass of leptons 0 and 1, (g) the reconstructed top mass, (h) $\Delta(R)$ between lepton 0 and 1, (i) the $\Delta(R)$ between the closest lepton and jet.

WZ Fit Region - 1j < 85% WP

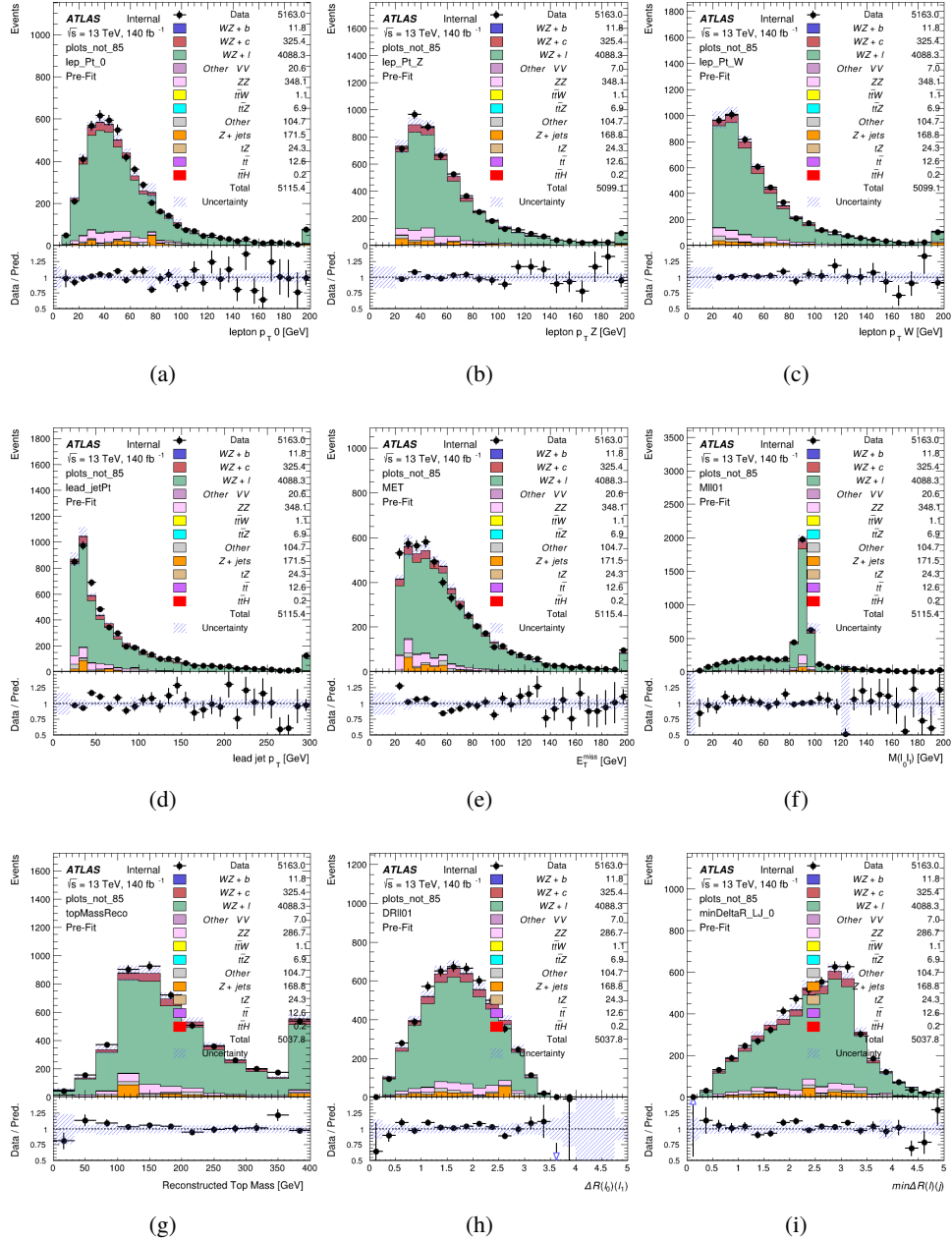


Figure 10: Comparisons between the data and MC distributions in the preselection region for (a) the p_T of the opposite sign lepton, (b) the p_T of the other lepton from the Z candidate, (c) the p_T of the lepton from the W candidate, (d) the leading jet p_T , (e) the E_T^{miss} , and (f) the invariant mass of leptons 0 and 1, (g) the reconstructed top mass, (h) $\Delta(R)$ between lepton 0 and 1, (i) the $\Delta(R)$ between the closest lepton and jet.

WZ Fit Region - 1j 77-85% WP

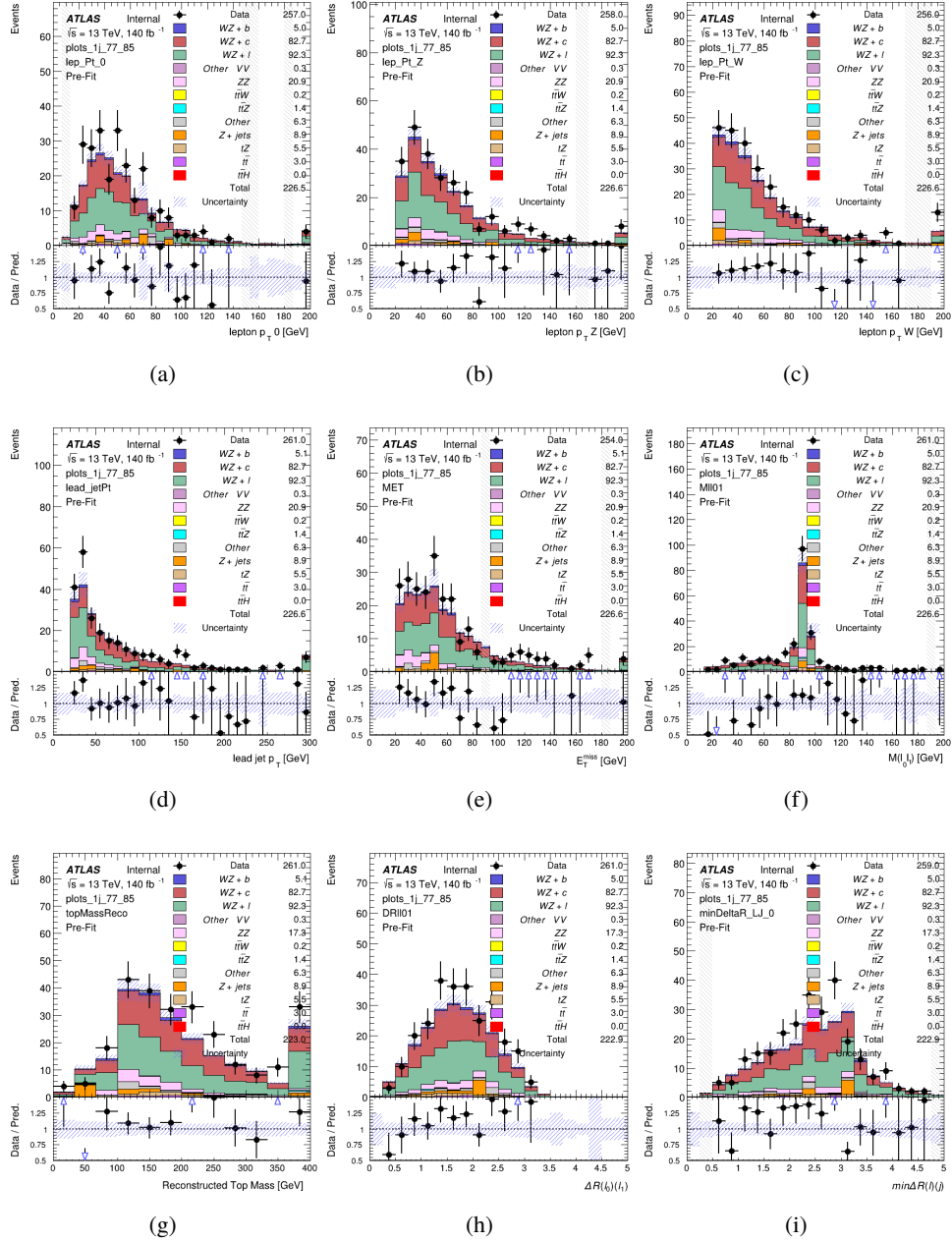


Figure 11: Comparisons between the data and MC distributions in the preselection region for (a) the p_T of the opposite sign lepton, (b) the p_T of the other lepton from the Z candidate, (c) the p_T of the lepton from the W candidate, (d) the leading jet p_T , (e) the E_T^{miss} , and (f) the invariant mass of leptons 0 and 1, (g) the reconstructed top mass, (h) $\Delta(R)$ between lepton 0 and 1, (i) the $\Delta(R)$ between the closest lepton and jet.

WZ Fit Region - 1j 70-77% WP

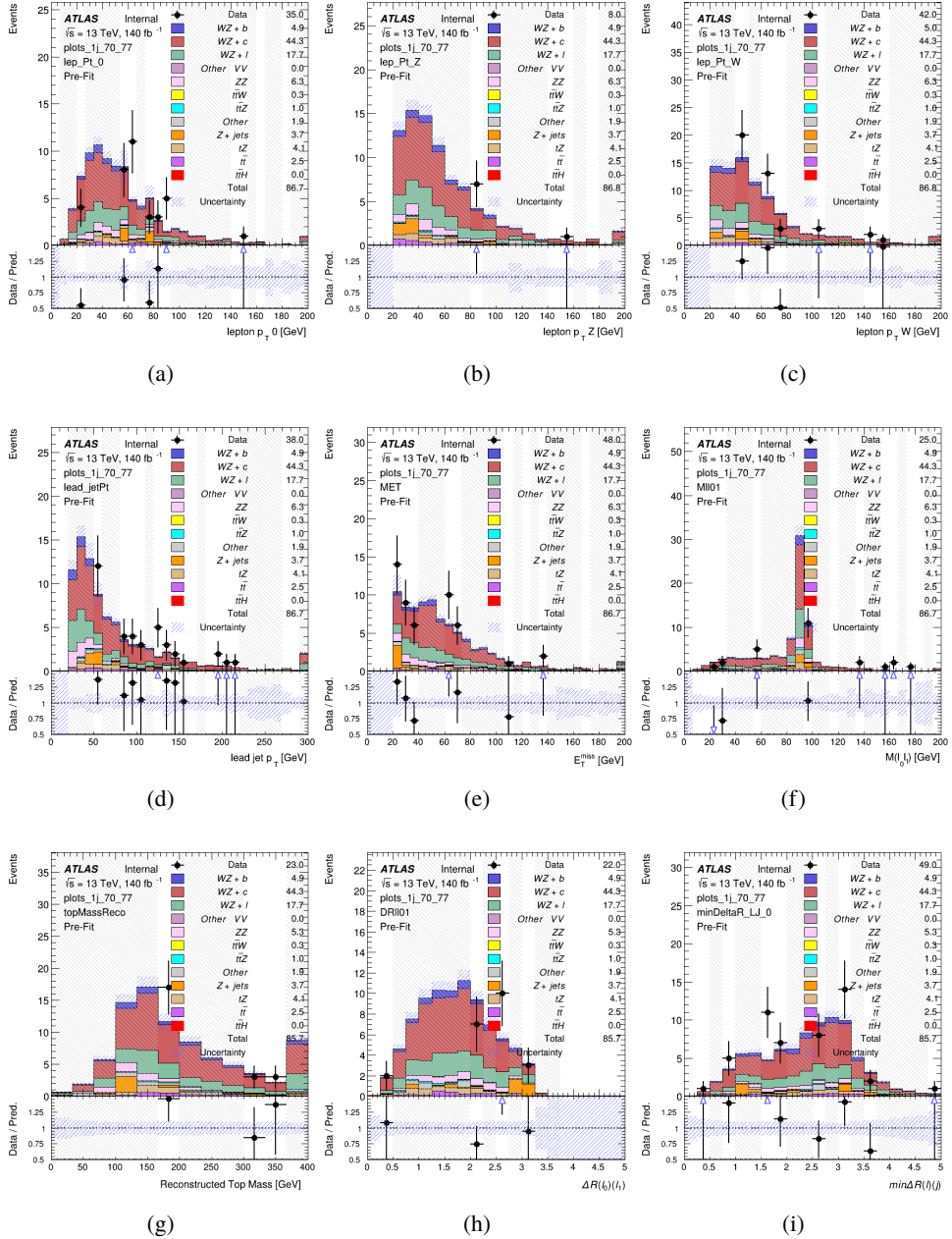


Figure 12: Comparisons between the data and MC distributions in the preselection region for (a) the p_T of the opposite sign lepton, (b) the p_T of the other lepton from the Z candidate, (c) the p_T of the lepton from the W candidate, (d) the leading jet p_T , (e) the E_T^{miss} , and (f) the invariant mass of leptons 0 and 1, (g) the reconstructed top mass, (h) $\Delta(R)$ between lepton 0 and 1, (i) the $\Delta(R)$ between the closest lepton and jet.

WZ Fit Region - 1j 60-70% WP

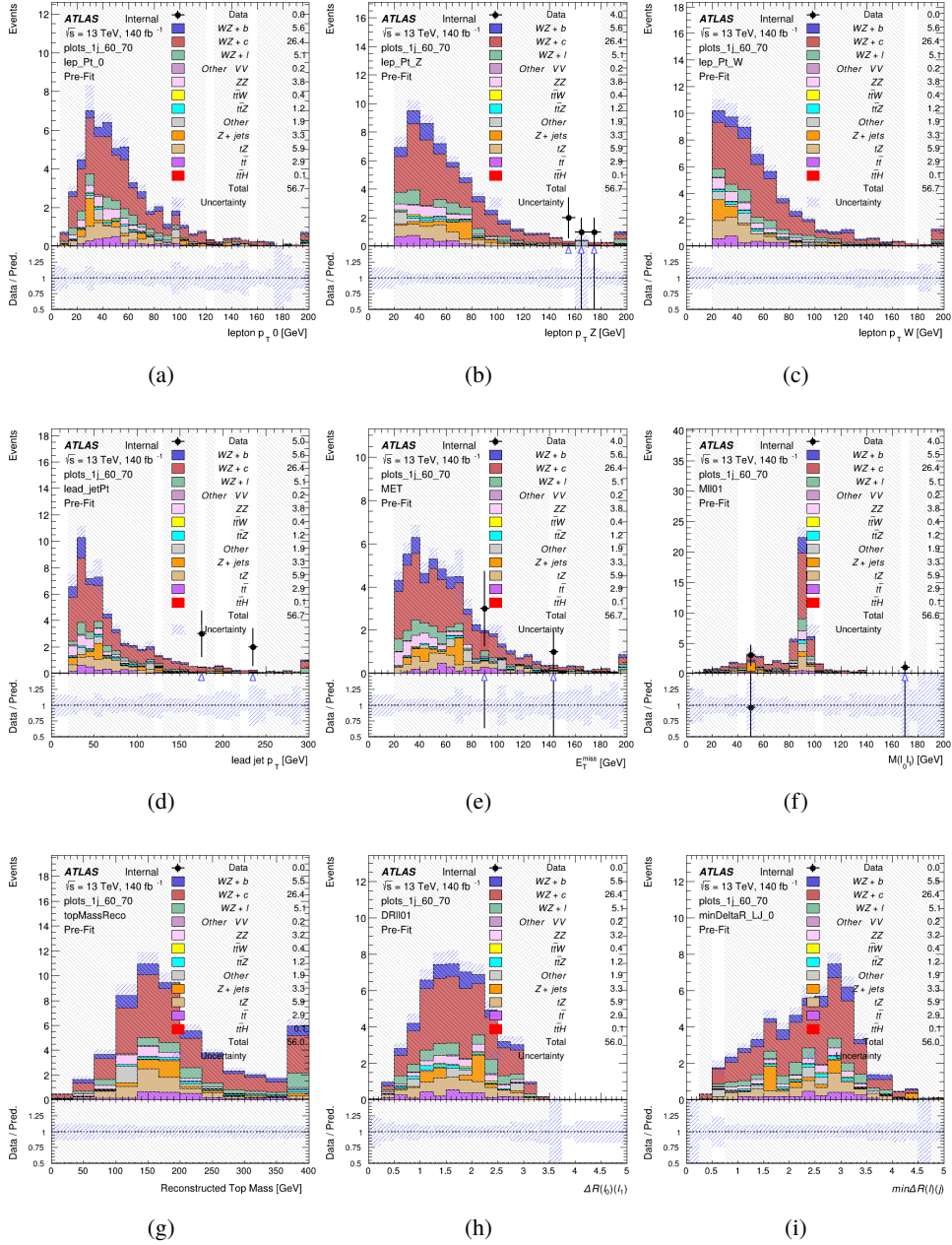


Figure 13: Comparisons between the data and MC distributions in the preselection region for (a) the p_T of the opposite sign lepton, (b) the p_T of the other lepton from the Z candidate, (c) the p_T of the lepton from the W candidate, (d) the leading jet p_T , (e) the E_T^{miss} , and (f) the invariant mass of leptons 0 and 1, (g) the reconstructed top mass, (h) $\Delta(R)$ between lepton 0 and 1, (i) the $\Delta(R)$ between the closest lepton and jet.

WZ Fit Region - 1j 60% WP

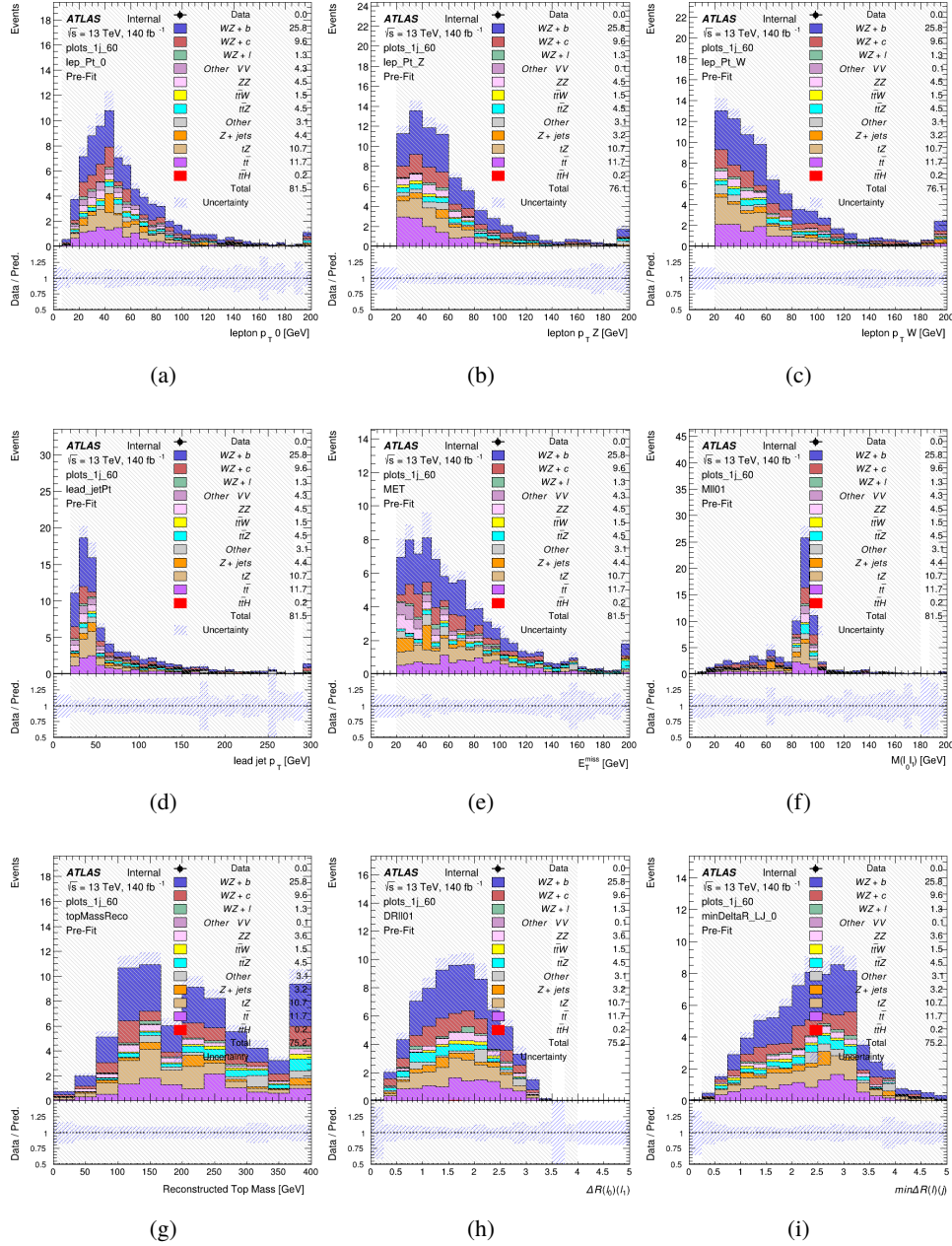


Figure 14: Comparisons between the data and MC distributions in the preselection region for (a) the p_T of the opposite sign lepton, (b) the p_T of the other lepton from the Z candidate, (c) the p_T of the lepton from the W candidate, (d) the leading jet p_T , (e) the E_T^{miss} , and (f) the invariant mass of leptons 0 and 1, (g) the reconstructed top mass, (h) $\Delta(R)$ between lepton 0 and 1, (i) the $\Delta(R)$ between the closest lepton and jet.

WZ Fit Region - tZ-CR

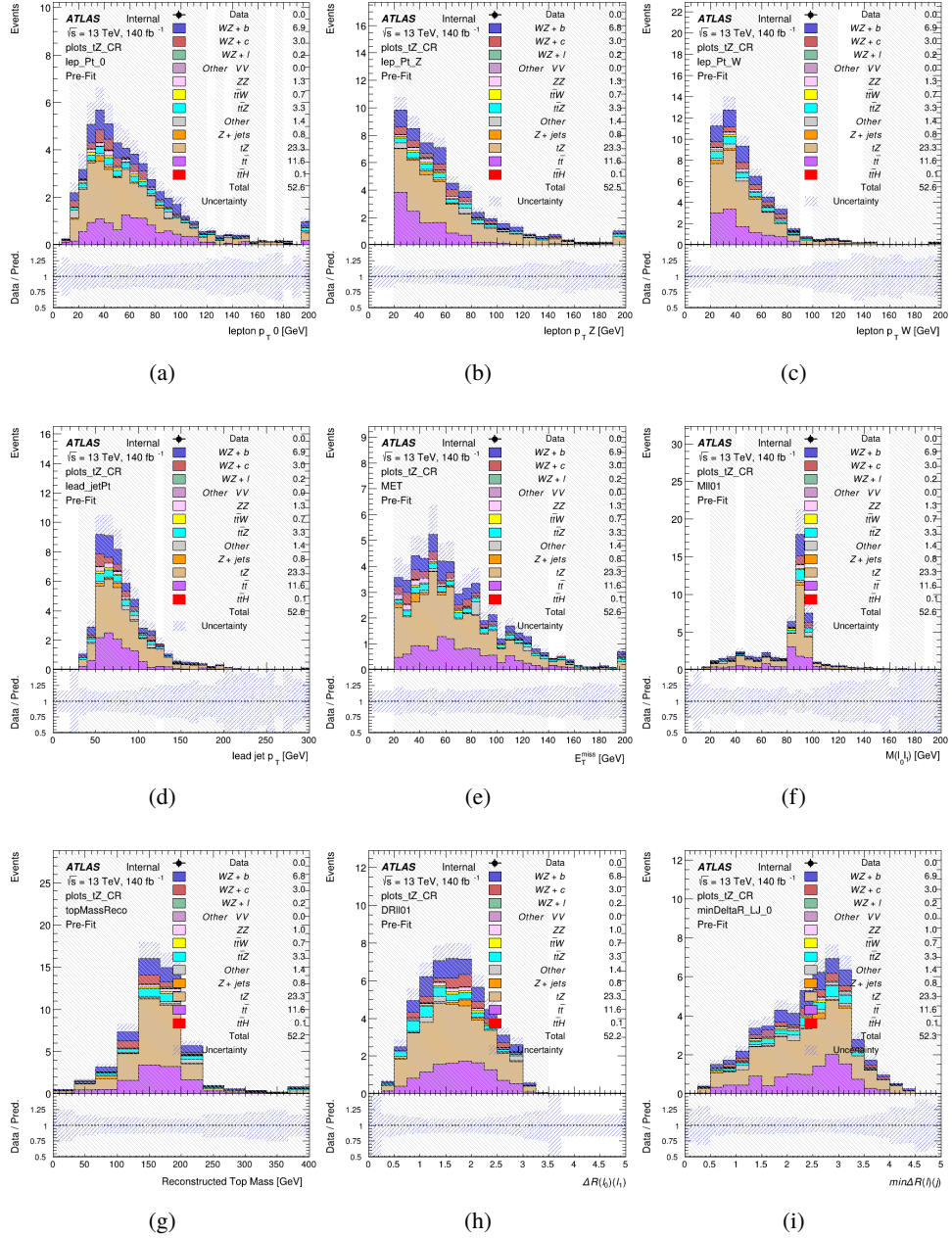


Figure 15: Comparisons between the data and MC distributions in the preselection region for (a) the p_T of the opposite sign lepton, (b) the p_T of the other lepton from the Z candidate, (c) the p_T of the lepton from the W candidate, (d) the leading jet p_T , (e) the E_T^{miss} , and (f) the invariant mass of leptons 0 and 1, (g) the reconstructed top mass, (h) $\Delta(R)$ between lepton 0 and 1, (i) the $\Delta(R)$ between the closest lepton and jet.

WZ Fit Region - 2j Inclusive

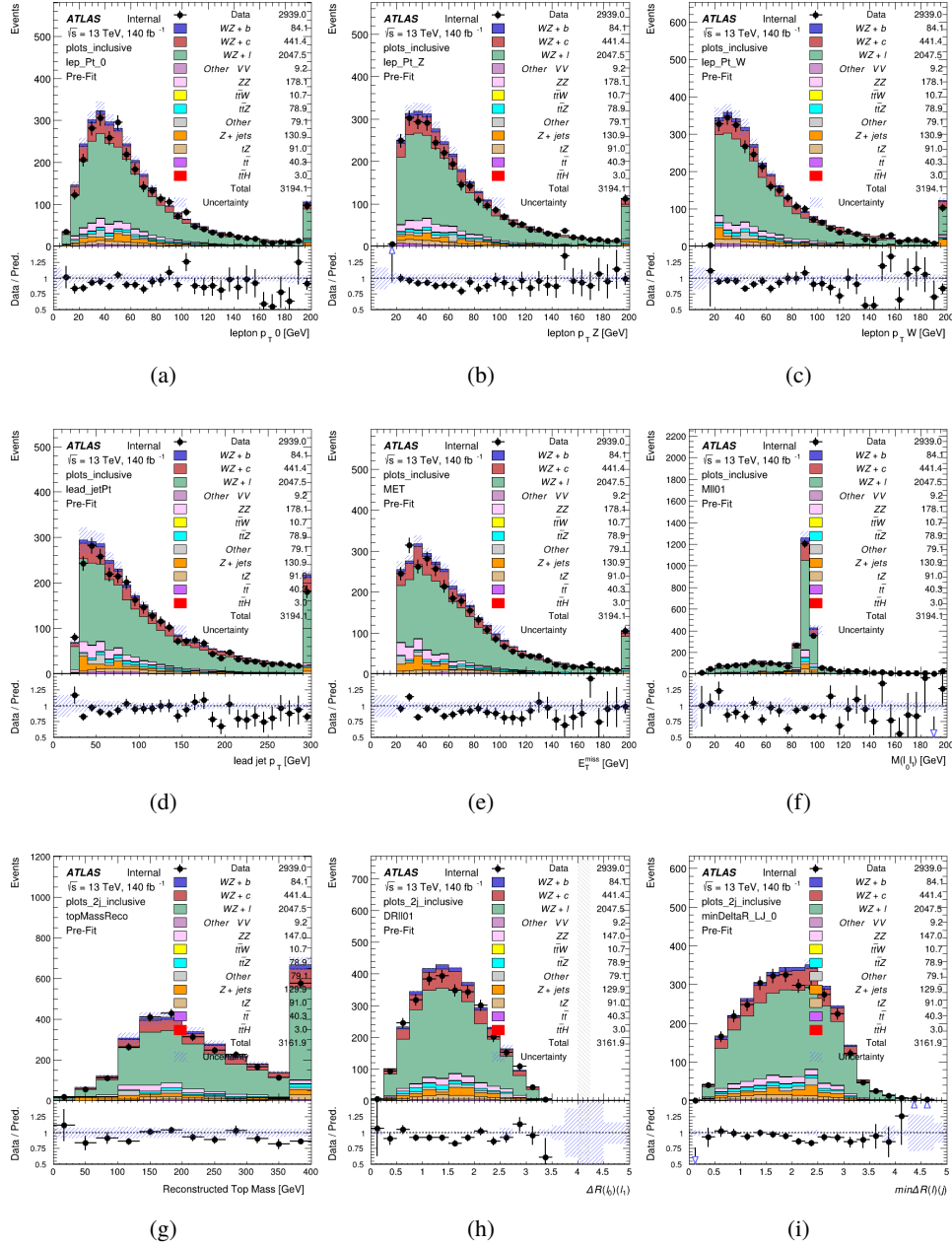


Figure 16: Comparisons between the data and MC distributions in the preselection region for (a) the p_T of the opposite sign lepton, (b) the p_T of the other lepton from the Z candidate, (c) the p_T of the lepton from the W candidate, (d) the leading jet p_T , (e) the E_T^{miss} , and (f) the invariant mass of leptons 0 and 1, (g) the reconstructed top mass, (h) $\Delta(R)$ between lepton 0 and 1, (i) the $\Delta(R)$ between the closest lepton and jet.

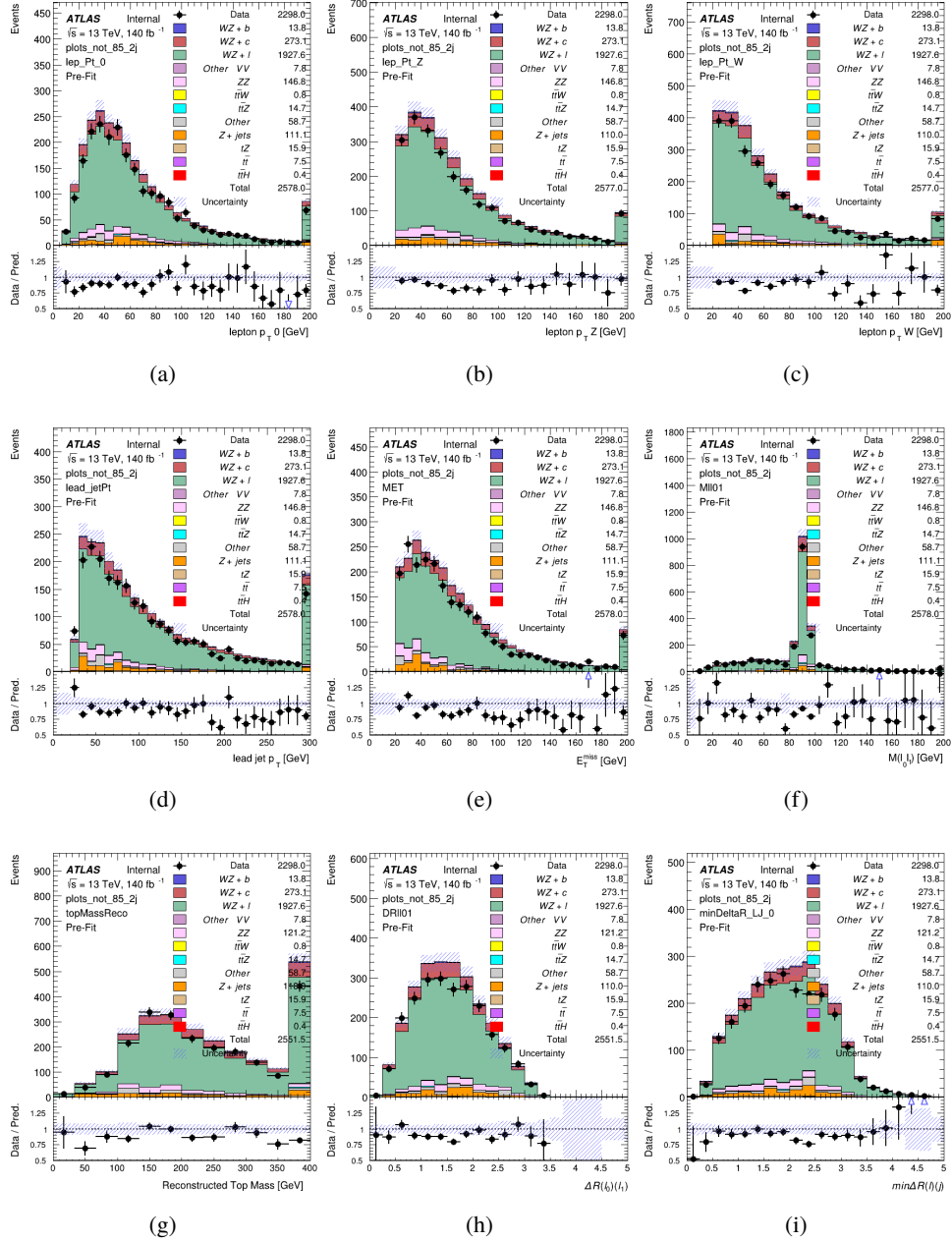
WZ Fit Region - $2j < 85\%$ WP

Figure 17: Comparisons between the data and MC distributions in the preselection region for (a) the p_T of the opposite sign lepton, (b) the p_T of the other lepton from the Z candidate, (c) the p_T of the lepton from the W candidate, (d) the leading jet p_T , (e) the E_T^{miss} , and (f) the invariant mass of leptons 0 and 1, (g) the reconstructed top mass, (h) $\Delta(R)$ between lepton 0 and 1, (i) the $\Delta(R)$ between the closest lepton and jet.

WZ Fit Region - 2j 77-85% WP

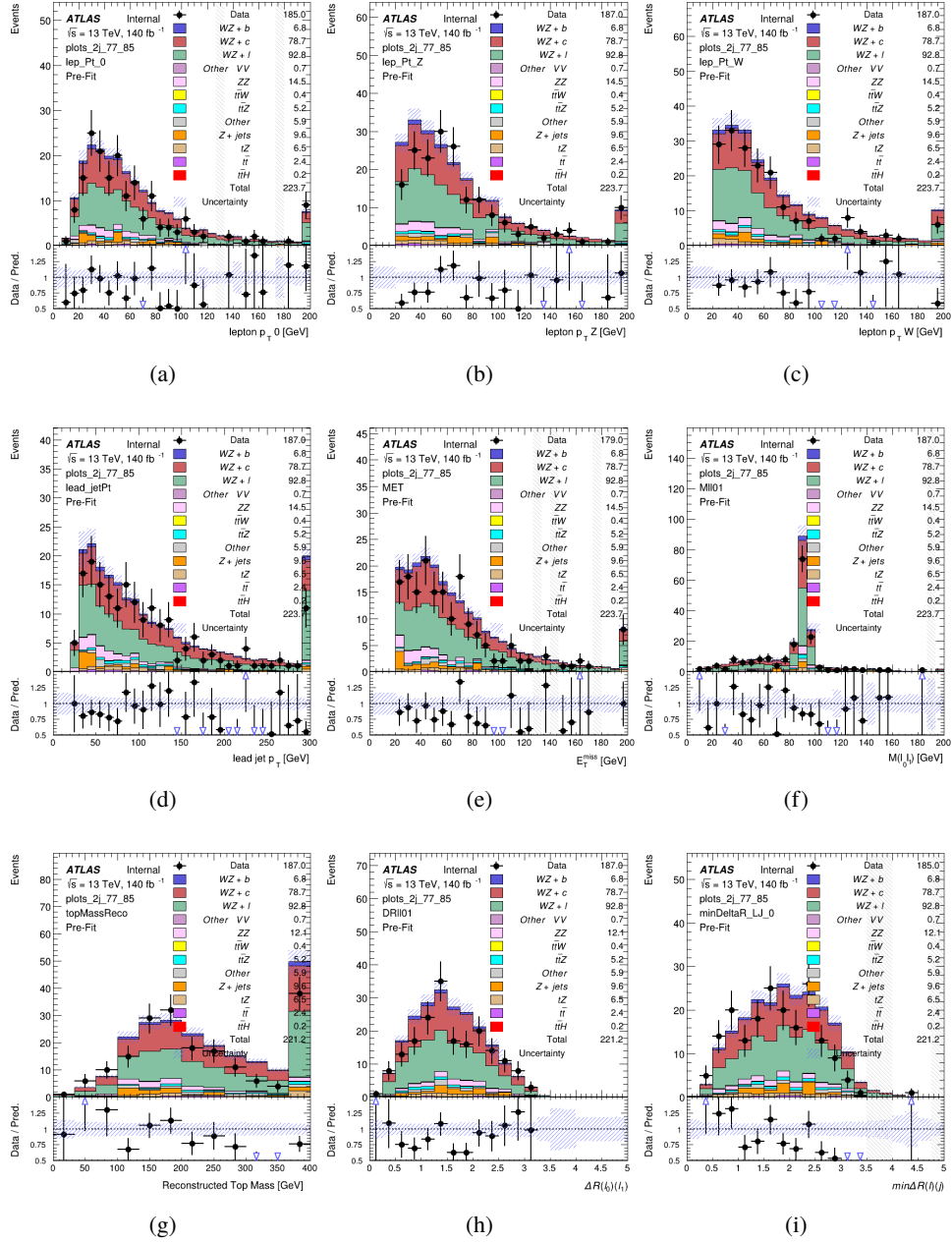


Figure 18: Comparisons between the data and MC distributions in the preselection region for (a) the p_T of the opposite sign lepton, (b) the p_T of the other lepton from the Z candidate, (c) the p_T of the lepton from the W candidate, (d) the leading jet p_T , (e) the E_T^{miss} , and (f) the invariant mass of leptons 0 and 1, (g) the reconstructed top mass, (h) $\Delta(R)$ between lepton 0 and 1, (i) the $\Delta(R)$ between the closest lepton and jet.

WZ Fit Region - 2j 70-77% WP

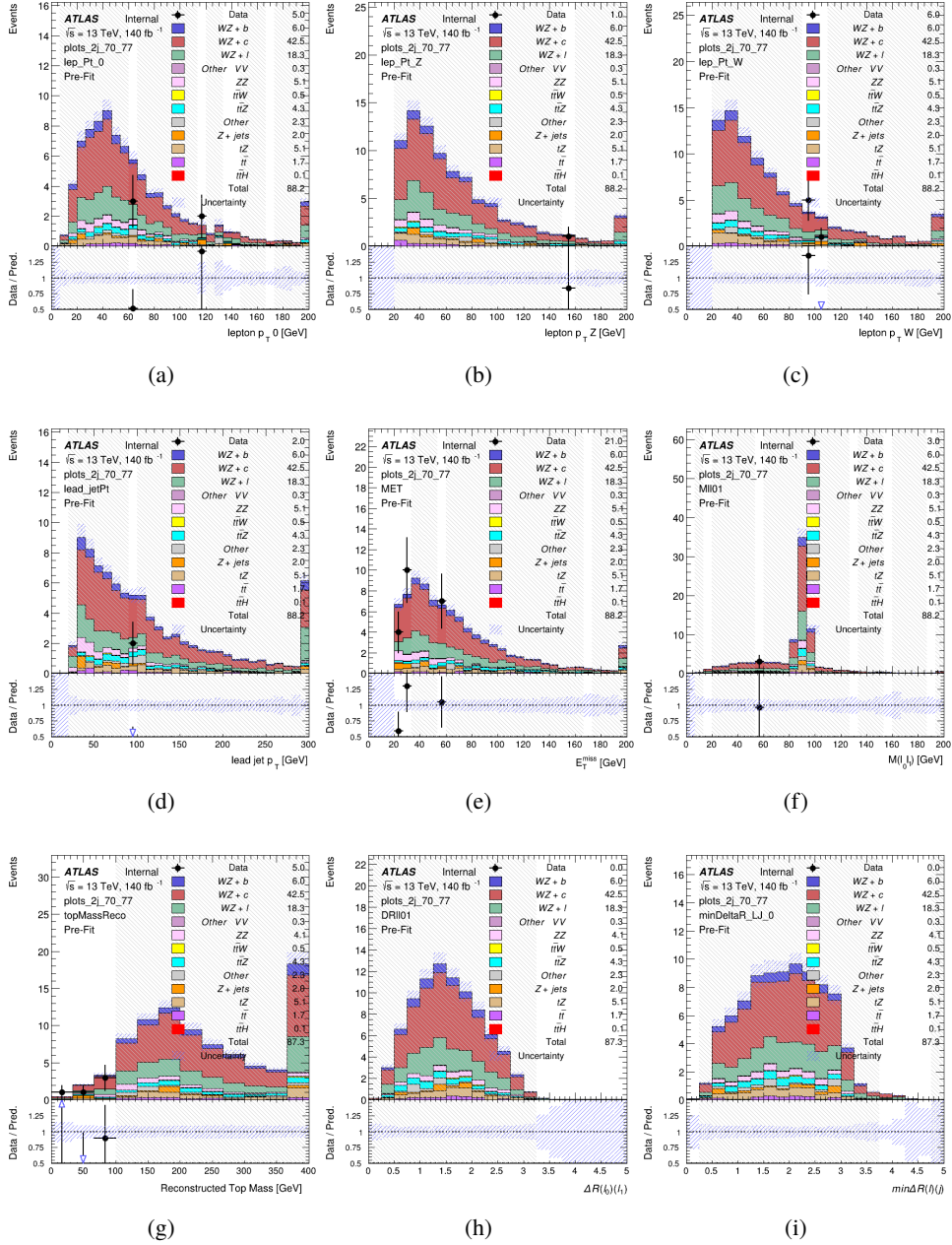


Figure 19: Comparisons between the data and MC distributions in the preselection region for (a) the p_T of the opposite sign lepton, (b) the p_T of the other lepton from the Z candidate, (c) the p_T of the lepton from the W candidate, (d) the leading jet p_T , (e) the E_T^{miss} , and (f) the invariant mass of leptons 0 and 1, (g) the reconstructed top mass, (h) $\Delta(R)$ between lepton 0 and 1, (i) the $\Delta(R)$ between the closest lepton and jet.

WZ Fit Region - 2j 60-70% WP

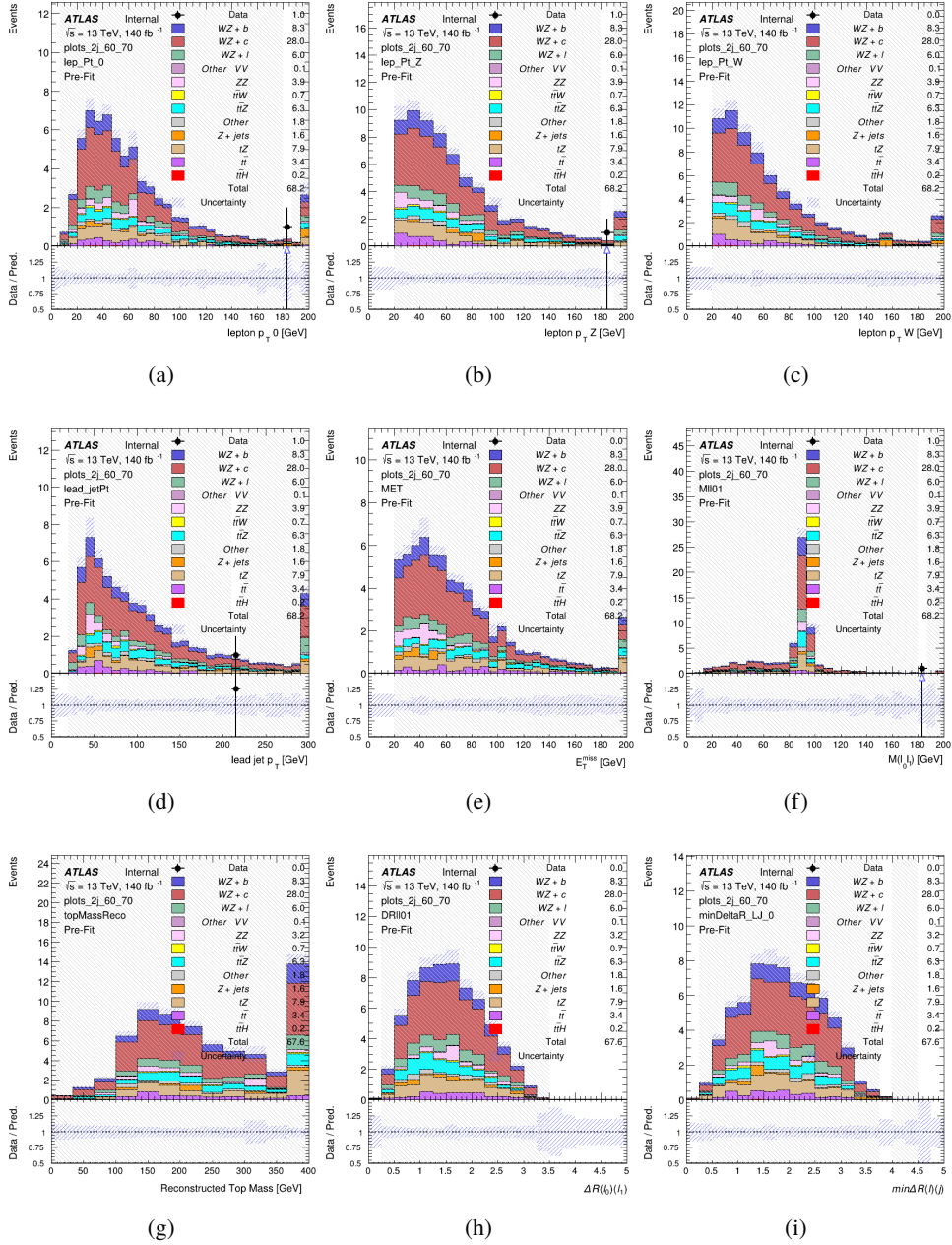


Figure 20: Comparisons between the data and MC distributions in the preselection region for (a) the p_T of the opposite sign lepton, (b) the p_T of the other lepton from the Z candidate, (c) the p_T of the lepton from the W candidate, (d) the leading jet p_T , (e) the E_T^{miss} , and (f) the invariant mass of leptons 0 and 1, (g) the reconstructed top mass, (h) $\Delta(R)$ between lepton 0 and 1, (i) the $\Delta(R)$ between the closest lepton and jet.

WZ Fit Region - 2j 60% WP

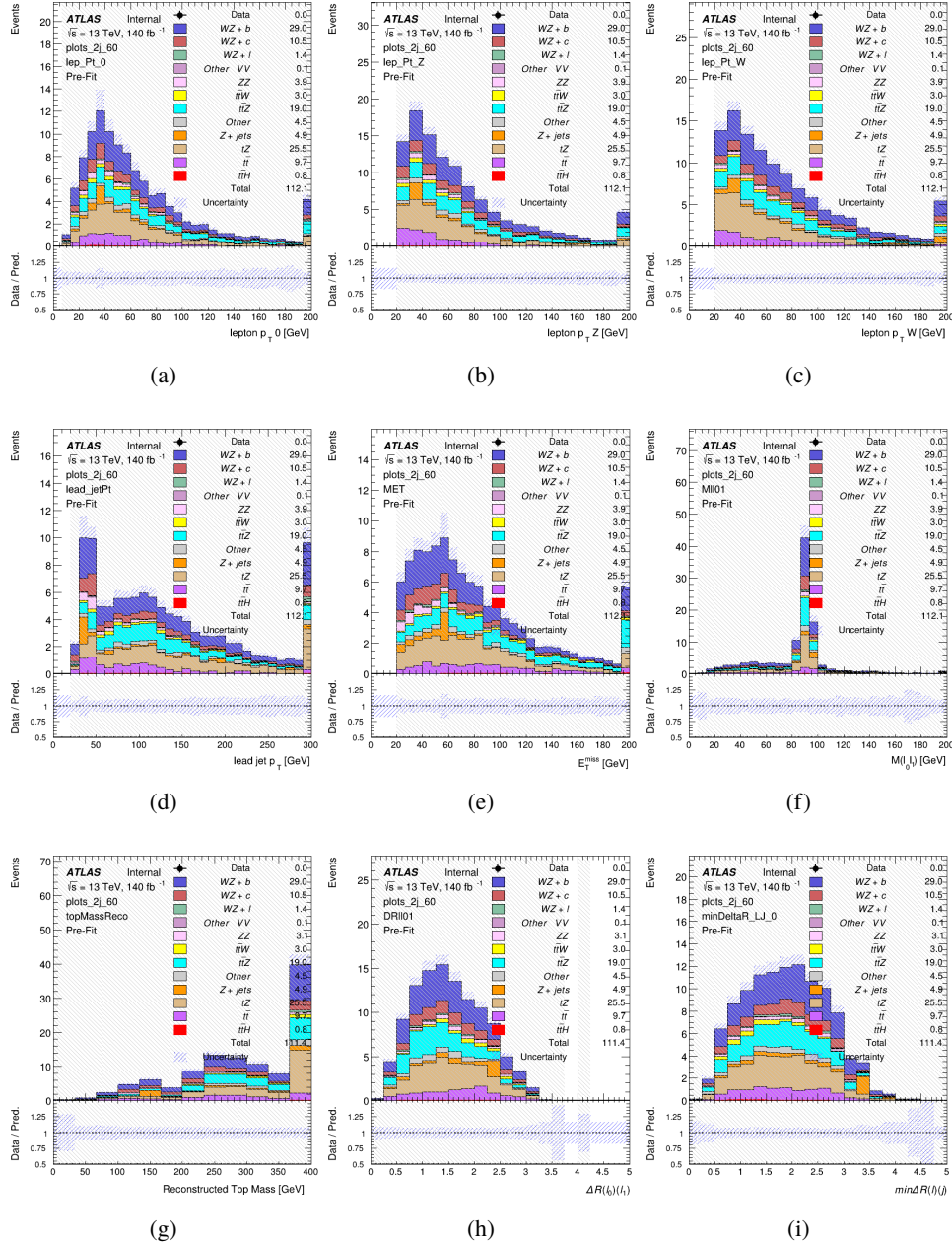


Figure 21: Comparisons between the data and MC distributions in the preselection region for (a) the p_T of the opposite sign lepton, (b) the p_T of the other lepton from the Z candidate, (c) the p_T of the lepton from the W candidate, (d) the leading jet p_T , (e) the E_T^{miss} , and (f) the invariant mass of leptons 0 and 1, (g) the reconstructed top mass, (h) $\Delta(R)$ between lepton 0 and 1, (i) the $\Delta(R)$ between the closest lepton and jet.

WZ Fit Region - tZ-CR-2j

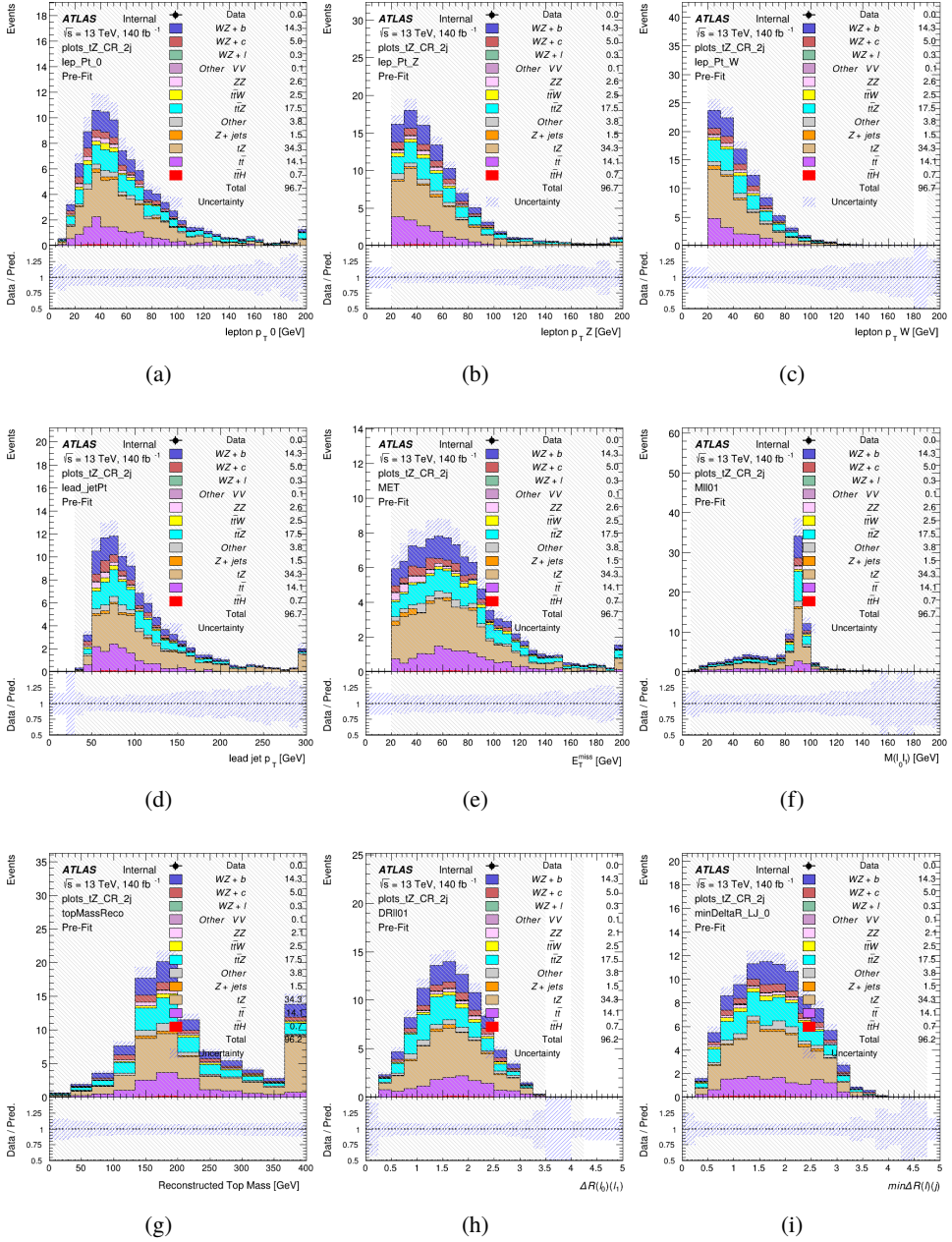


Figure 22: Comparisons between the data and MC distributions in the preselection region for (a) the p_T of the opposite sign lepton, (b) the p_T of the other lepton from the Z candidate, (c) the p_T of the lepton from the W candidate, (d) the leading jet p_T , (e) the E_T^{miss} , and (f) the invariant mass of leptons 0 and 1, (g) the reconstructed top mass, (h) $\Delta(R)$ between lepton 0 and 1, (i) the $\Delta(R)$ between the closest lepton and jet.

438 **6.3 Non-Prompt Lepton Estimation**

439 Two processes act as sources of non-prompt leptons appear in the analysis: $t\bar{t}$ and Z+jet
 440 production both produce two prompt leptons, and each contribute to the 31 region when an
 441 additional non-prompt lepton appears in the event. The contribution of these processes is
 442 estimated with Monte Carlo simulations, which are validated using enriched validation regions.

443 The modelling in the Z+jets and $t\bar{t}$ CRs is further validated for each of the pseudo-continuous
 444 b-tag regions used in the analysis. The relevant lepton p_T spectrum in each b-tag region is shown
 445 in Appendix A.2 for these CRs after the correction factors derived below have been applied.

446 **6.3.1 $t\bar{t}$ Validation**

447 $t\bar{t}$ events can produce two prompt leptons from the decay of each of the tops. These top decays
 448 produce two b-quarks, the decay of which can produce additional non-prompt leptons, which
 449 occasionally pass the event preselection. In order to validate that the Monte Carlo accurately
 450 simulates this process accurately, the MC prediction in a non-prompt $t\bar{t}$ enriched validation
 451 region is compared to data.

452 The $t\bar{t}$ validation region is similar to the preselection region - three leptons meeting the criteria
 453 described in Section 6 are required, and the requirements on E_T^{miss} remain the same. However,
 454 the selection requiring that a lepton pair form a Z-candidate are reversed. Events where the
 455 invariant mass of any two opposite sign, same flavor leptons falls within 10 GeV of 91.2 GeV are
 456 rejected. This ensures the $t\bar{t}$ validation region is orthogonal to the preselection region.

457 Further, because the jet multiplicity of $t\bar{t}$ events tends to be higher than WZ + jets, the number
 458 of jets in each event is required to be greater than 1. As b-jets are almost invariably produced
 459 from top decays, at least one b-tagged jet passing the 70% DL1r WP in each event is required.
 460 Various kinematic plots of this region are shown in Figure 23.

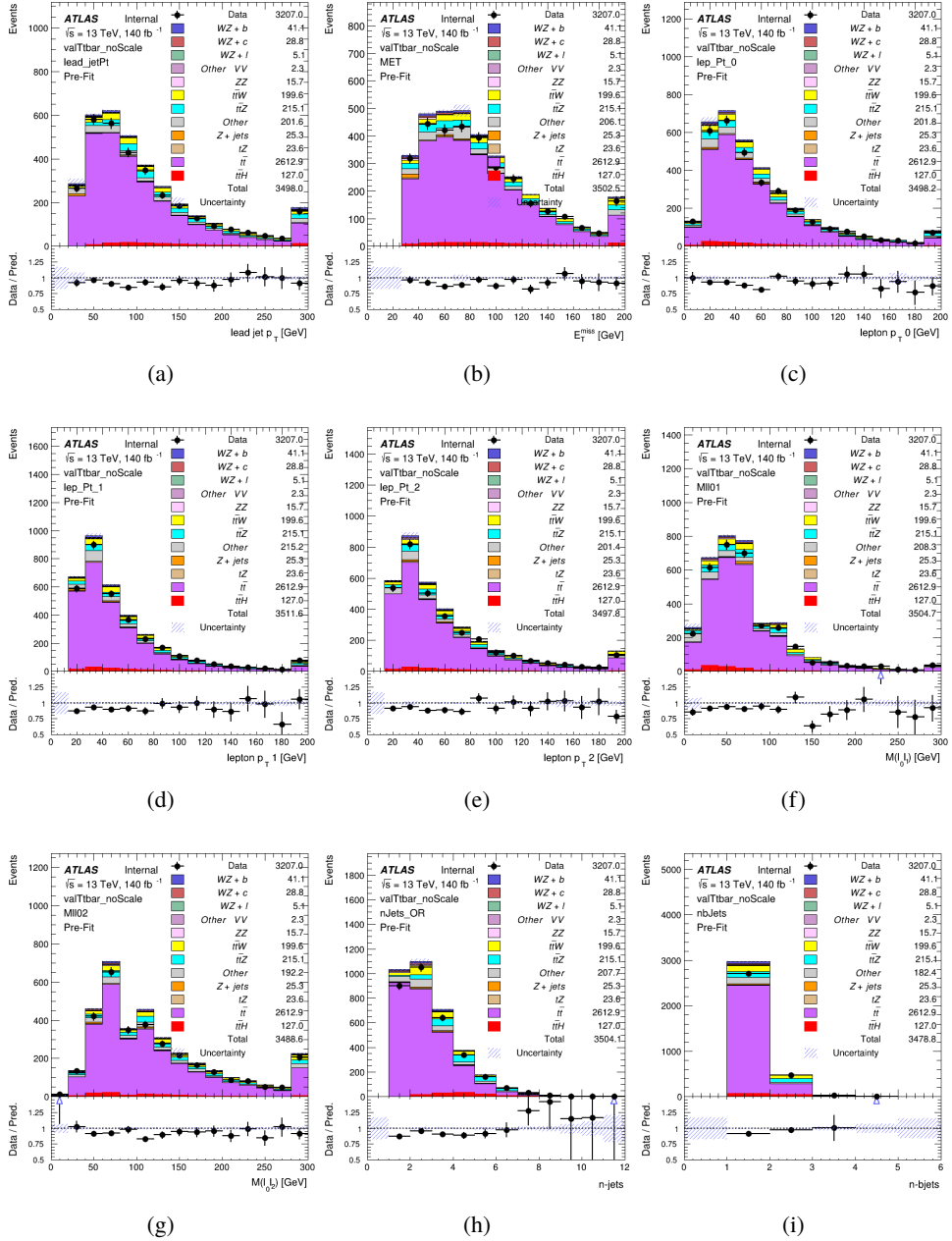


Figure 23: Comparisons between the data and MC distributions in the $t\bar{t}$ validation region for (a) the p_T of the leading jet, (b) the missing transverse energy, (c) the p_T of lepton 0, (d) p_T of lepton 1, (e) p_T of lepton 2, (f) the invariant mass of leptons 0 and 1, (g) the invariant mass of leptons 0 and 2, (h) the number of jets, (i) the number of b-tagged jets.

461 The shape of each distribution agrees quite well between data and MC, with a constant offset
 462 between the two. This is accounted for by applying a constant correction factor of 0.9 to the $t\bar{t}$

463 MC prediction. Plots showing the kinematics of the $t\bar{t}$ VR after this correction factor has been
 464 applied are shown in Figure 24.

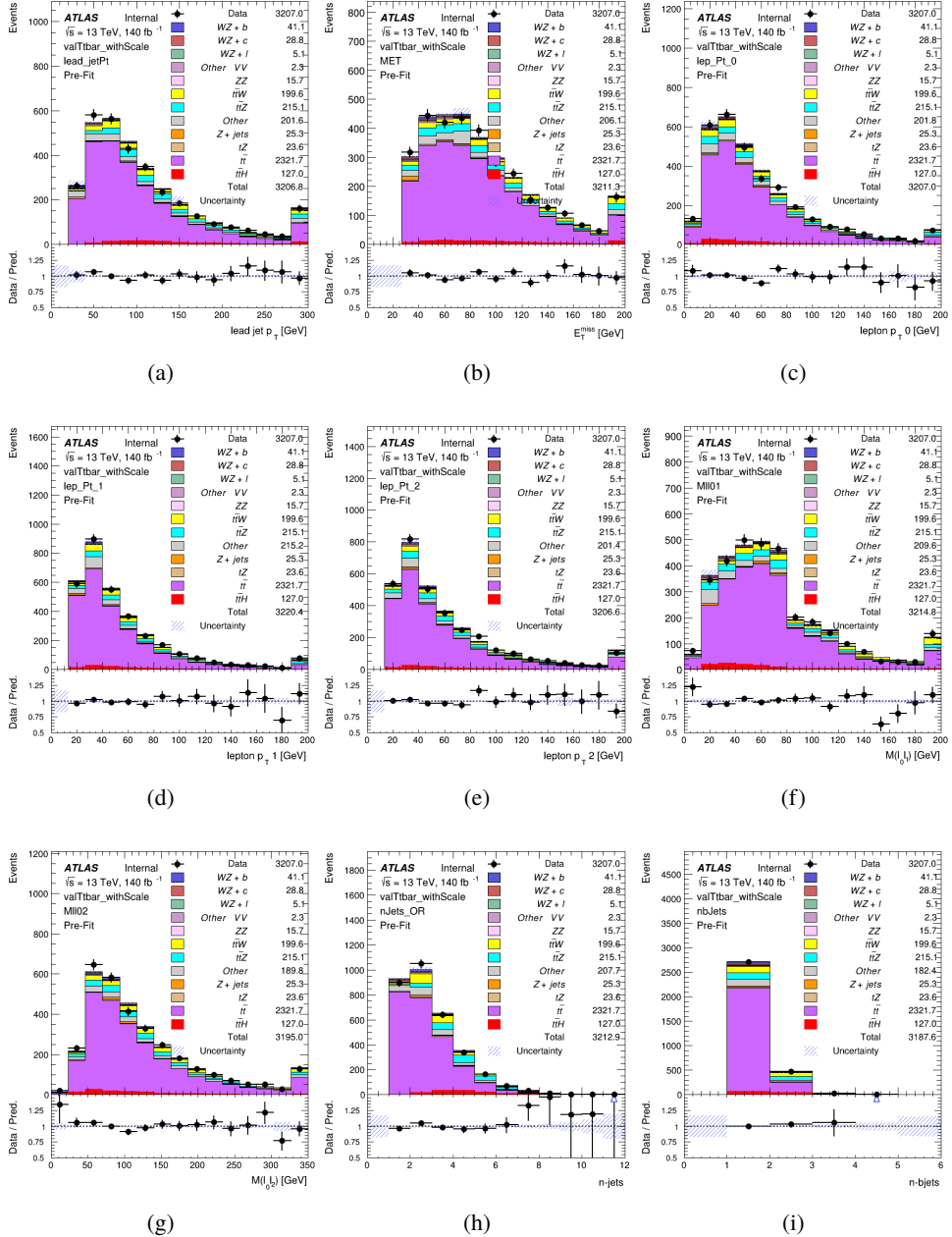


Figure 24: Comparisons between the data and MC distributions in the $t\bar{t}$ validation region after the correction factor has been applied for (a) the p_T of the leading jet, (b) the missing transverse energy, (c) the p_T of lepton 0, (d) p_T of lepton 1, (e) p_T of lepton 2, (f) the invariant mass of leptons 0 and 1, (g) the invariant mass of leptons 0 and 2, (h) the number of jets, (i) the number of b-tagged jets.

465 The modeling is further validated by looking at the yield in the $t\bar{t}$ VR for each DL1r WP, giving
 466 a clearer correspondence to the signal regions used in the fit. For these plots, the requirement
 467 that each event contain at least one b-tagged jet is removed. Each region shown in Figure 25
 468 requires one or more jets pass the listed WP, with no jets passing the next highest WP.

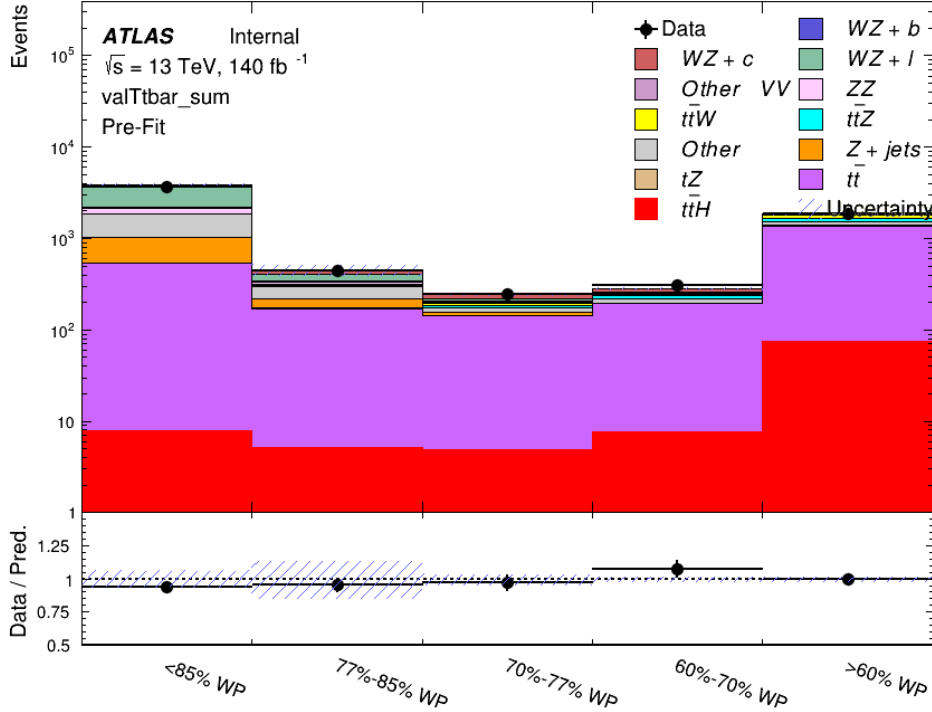


Figure 25: Data and MC comparisons for each DL1r WP for both 1-jet and 2-jet regions, after the $t\bar{t}$ VR selection and correction factor have been applied

469 As data and MC are found to agree within 20% for each of these working points, a 20% systematic
 470 uncertainty on the $t\bar{t}$ prediction is included for the analysis.

471 6.3.2 Z+jets Validation

472 Similar to $t\bar{t}$, a non-prompt Z+jets validation region is produced in order to validate the MC
 473 predictions. The lepton requirements remain the same as the preselection region. Because no
 474 neutrinos are present for this process, the E_T^{miss} cut is reversed, requiring $E_T^{\text{miss}} < 30 \text{ GeV}$. This
 475 also ensures this validation region is orthogonal to the preselection region. Further, the number
 476 of jets in each event is required to be greater than or equal to one. Various kinematic plots of this
 477 region are shown below. The general agreement between data and MC in each of these suggests
 478 that the non-prompt contribution of Z+jets is well modeled by Monte Carlo.

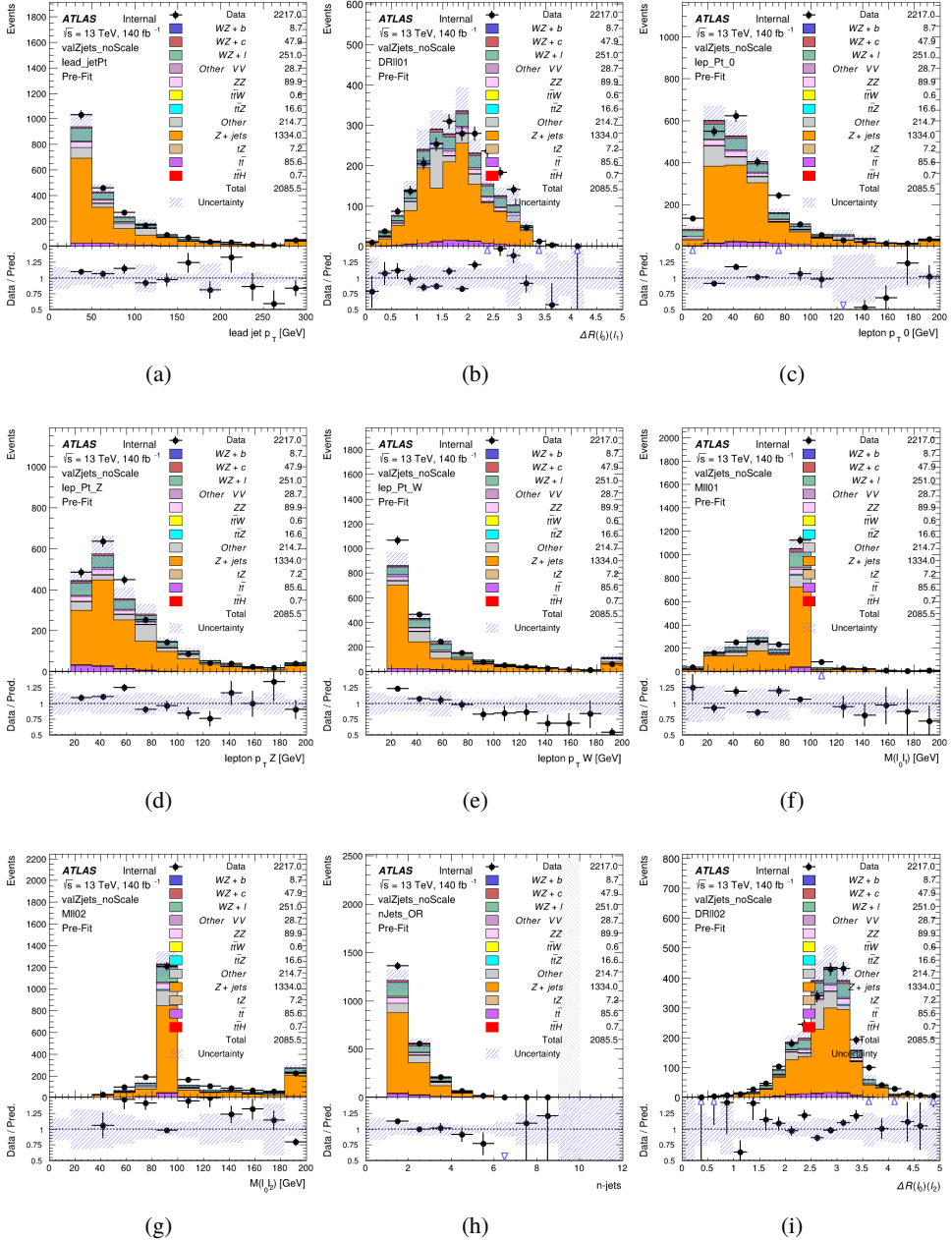


Figure 26: Comparisons between the data and MC distributions in the Z+jets validation region for (a) the p_T of the leading jet, (b) ΔR between leptons 0 and 1, (c) the p_T of lepton 0, (d) p_T of SS lepton from the Z candidate, (e) p_T of the SS lepton from the W candidate, (f) the invariant mass of leptons 0 and 1, (g) the invariant mass of leptons 0 and 2, (h) the number of jets, (i) ΔR between leptons 0 and 2. Includes only statistical uncertainties

479 While there is general agreement between data and MC within statistical uncertainty, the shape

of the p_T spectrum of the lepton from the W candidate is found to differ. As this is the lepton not included in the Z-candidate, in the case of Z+jets, this lepton is most often the non-prompt lepton. A similar effect is seen for both non-prompt muons and electrons in the Z+jets validation region, as shown in Figure 27.

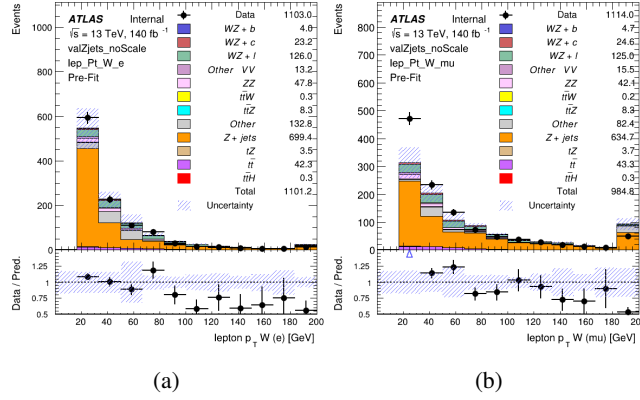


Figure 27: p_T spectrum of the lepton from the W candidate for (a) electrons and (b) muons

To account for this discrepancy, a variable correction factor is applied to Z+jets. χ^2 minimization of the W lepton p_T spectrum is performed to derive a correction factor as a function of this p_T . Kinematic plots of the Z + jets validation region after this correction factor has been applied are shown in Figure 28.

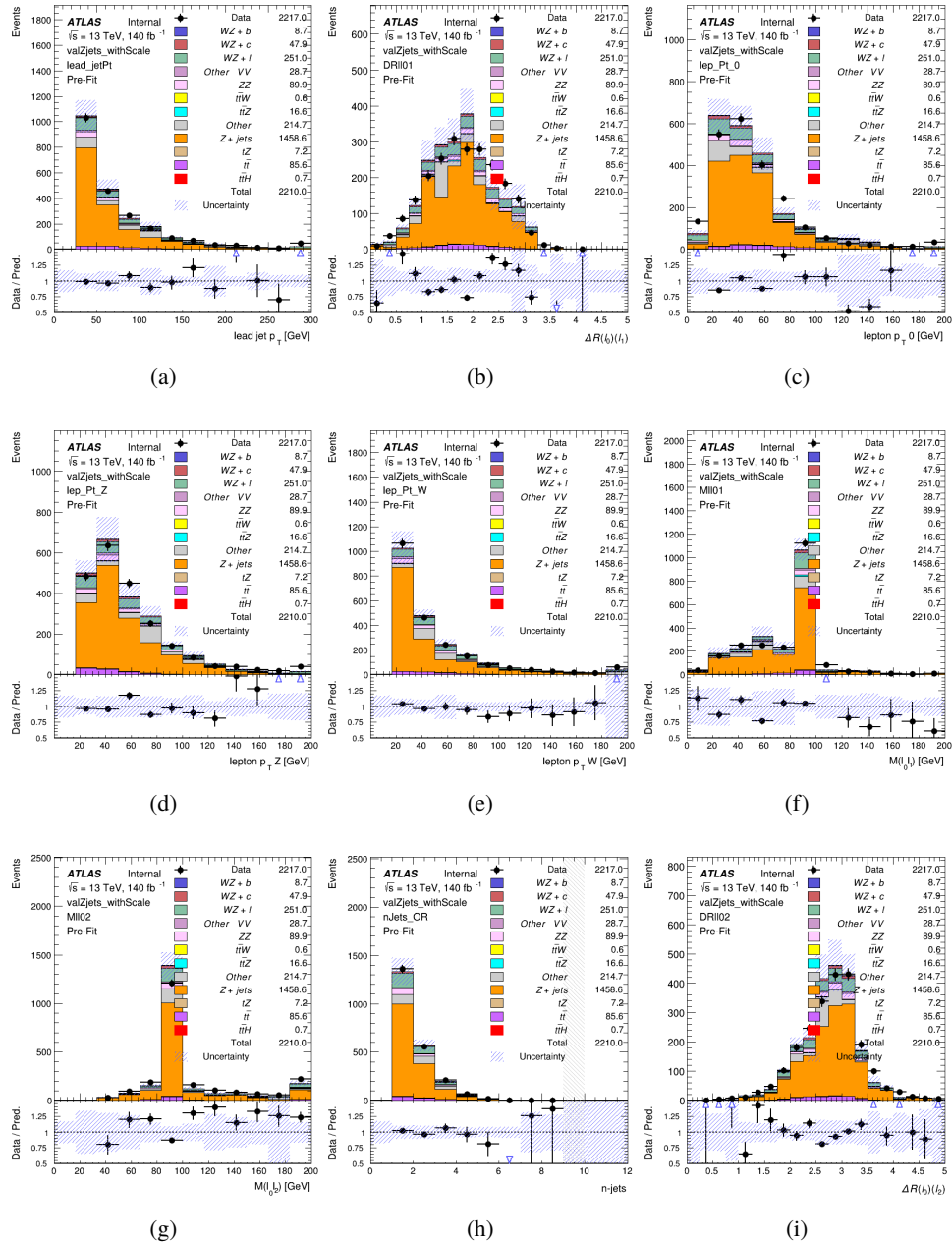


Figure 28: Comparisons between the data and MC distributions in the Z+jets validation region after the correction factor has been applied for (a) the p_T of the leading jet, (b) ΔR between leptons 0 and 1, (c) the p_T of lepton 0, (d) p_T of SS lepton from the Z candidate, (e) p_T of the SS lepton from the W candidate, (f) the invariant mass of leptons 0 and 1, (g) the invariant mass of leptons 0 and 2, (h) the number of jets, (i) ΔR between leptons 0 and 2

488 The modeling is further validated by looking at the yield in the Z+jets VR for each DL1r WP,

489 giving a clearer correspondence to the signal regions used in the fit. Each region shown in Figure
 490 29 requires one or more jets pass the listed WP, with no jets passing the next highest WP.

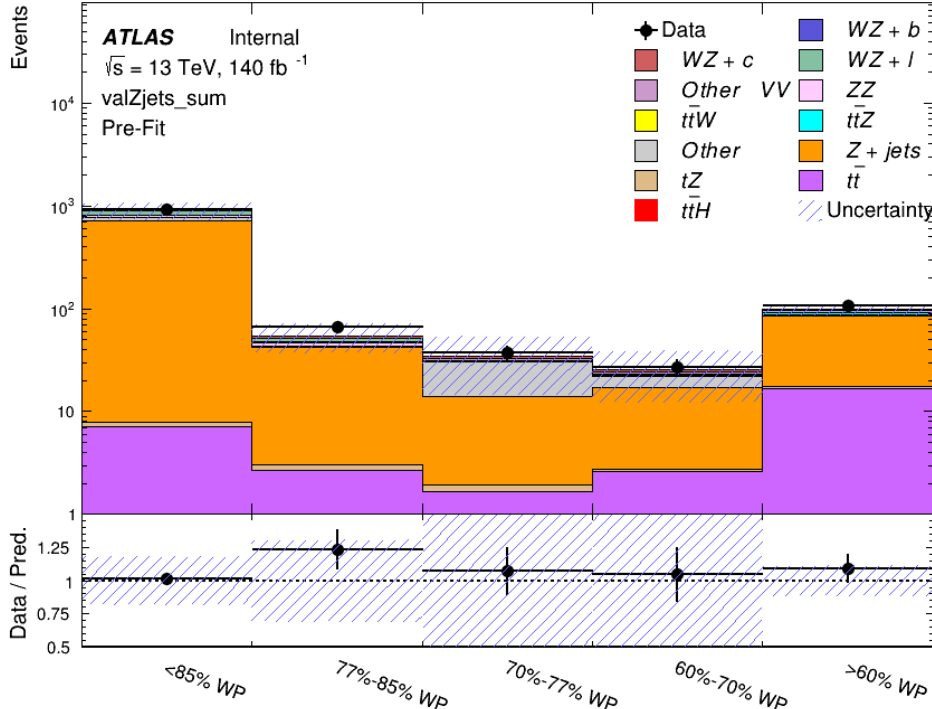


Figure 29: Data and MC comparisons for each DL1r WP for both 1-jet and 2-jet regions, after the Z+jets VR selection and correction factor have been applied

491 For each of the b-tagging working points considered, the data falls within 25% of the MC
 492 prediction once this correction factor has been applied. Therefore, a 25% systematic uncertainty
 493 is applied to Z + jets in the analysis.

7 Systematic Uncertainties

495 The systematic uncertainties that are considered are summarized in Table 9. These are imple-
 496 mented in the fit either as a normalization factors or as a shape variation or both in the signal
 497 and background estimations. The numerical impact of each of these uncertainties is outlined in
 498 Section 8.

Table 9: Sources of systematic uncertainty considered in the analysis.

Systematic uncertainty	Components
Luminosity	1
Pileup reweighting	1
Physics Objects	
Electron	5
Muon	14
Prompt Lepton Veto	1
Jet energy scale	28
Jet energy resolution	8
Jet vertex fraction	1
Jet flavor tagging	131
E_T^{miss}	3
Total (Experimental)	194
Signal Modeling	
Shape modelling	3
Renormalization and factorization scales	5
nJet Migration	5
Background Modeling	
Cross section	15
Renormalization and factorization scales	12
Parton shower and hadronization model	2
Shower tune	4
Total (Signal and background modeling)	41
Total (Overall)	235

499 The uncertainty in the combined 2015–2018 integrated luminosity is 1.7% [25], obtained using
500 the LUCID-2 detector [26] for the primary luminosity measurements.

501 The experimental uncertainties are related to the reconstruction and identification of light
502 leptons and b-tagging of jets, and to the reconstruction of E_T^{miss} . The TOTAL electron ID
503 correlation model is used, corresponding to 1 electron ID systematic [27]. Electron ID is found
504 to be a subleading systematic that is unconstrained by the fit, making it an appropriate choice for
505 this analysis.

506 The sources which contribute to the uncertainty in the jet energy scale (JES) [28] are decom-
507 posed into uncorrelated components and treated as independent sources in the analysis. The
508 CategoryReduction model is used to account for JES uncertainties, which decomposes the uncer-
509 tainties into 30 nuisance parameters included in the fit. The SimpleJER model is used to account

510 for jet energy resolution (JER) uncertainties, and 8 JER uncertainty components included as NPs
511 in the fit.

512 The uncertainties in the b-tagging efficiencies measured in dedicated calibration analyses
513 [19] are also decomposed into uncorrelated components. The large number of components for
514 b-tagging is due to the calibration of the distribution of the MVA discriminant.

515 The full list of systematic uncertainties considered in the analysis is summarized in Tables 10,
516 11 and 12.

517

Experimental Systematics on Leptons and E_T^{miss}			
Type	Description	Systematics Name	Application
Trigger			
Scale Factors	Trigger Efficiency	lepSFTrigTight_MU(EL)_SF_Trigger_STAT(SYST)	Event Weight
Muons			
Efficiencies	Reconstruction and Identification	lepSFObjTight_MU_SF_ID_STAT(SYST)	Event Weight
	Isolation	lepSFObjTight_MU_SF_Isol_STAT(SYST)	Event Weight
	Track To Vertex Association	lepSFObjTight_MU_SF_TTVA_STAT(SYST)	Event Weight
p_T Scale	p_T Scale	MUONS_SCALE	p_T Correction
Resolution	Inner Detector Energy Resolution	MUONS_ID	p_T Correction
	Muon Spectrometer Energy Resolution	MUONS_MS	p_T Correction
Electrons			
Efficiencies	Reconstruction	lepSFObjTight_EL_SF_ID	Event Weight
	Identification	lepSFObjTight_EL_SF_Reco	Event Weight
	Isolation	lepSFObjTight_EL_SF_Isol	Event Weight
Scale Factor	Energy Scale	EG_SCALE_ALL	Energy Correction
Resolution	Energy Resolution	EG_RESOLUTION_ALL	Energy Correction
E_T^{miss}			
Soft Tracks Terms	Resolution	MET_SoftTrk_ResoPerp	p_T Correction
	Resolution	MET_SoftTrk_ResoPara	p_T Correction
	Scale	MET_SoftTrk_ScaleUp	p_T Correction
	Scale	MET_SoftTrk_ScaleDown	p_T Correction

Table 10: Summary of experimental systematics considered for leptons and E_T^{miss} . Includes type, description, name of systematic as used in the fit, and mode of application. The mode of application indicates the systematic evaluation, e.g. as an overall event re-weighting (Event Weight) or rescaling (p_T Correction).

Experimental Systematics on Jets			
Type	Origin	Systematics Name	Application
Jet Vertex Tagger		JVT	Event Weight
Energy Scale	Calibration Method	JET_21NP_ JET_EffectiveNP_1-19	p_T Correction p_T Correction
	η inter-calibration	JET_EtaIntercalibration_Modelling JET_EtaIntercalibration_NonClosure JET_EtaIntercalibration_TotalStat	p_T Correction p_T Correction p_T Correction
	High p_T jets	JET_SingleParticle_HighPt	p_T Correction
	Pile-Up	JET_Pileup_OffsetNPV JET_Pileup_OffsetMu JET_Pileup_PtTerm JET_Pileup_RhoTopology	p_T Correction p_T Correction p_T Correction p_T Correction
	Non Closure	JET_PunchThrough_MC15	p_T Correction
	Flavour	JET_Flavor_Response JET_BJES_Response JET_Flavor_Composition	p_T Correction p_T Correction p_T Correction
Resolution		JET_JER_SINGLE_NP	Event Weight

Table 11: Jet systematics take into account effects of jets calibration method, η inter-calibration, high p_T jets, pile-up, and flavor response. They are all diagonalised into effective parameters.

Experimental Systematics on b-tagging		
Type	Origin	Systematic Name
Scale Factors	DL1r b-tagger efficiency on b originated jets in bins of η	DL1r_Continuous_EventWeight_B0-29
	DL1r b-tagger efficiency on c originated jets in bins of η	DL1r_Continuous_EventWeight_C0-19
	DL1r b-tagger efficiency on light flavoured originated jets in bins of η and p_T	DL1r_Continuous_EventWeight_Light0-79
	DL1r b-tagger extrapolation efficiency	DL1r_Continuous_EventWeight_extrapolation DL1r_Continuous_EventWeight_extrapolation_from_charm

Table 12: Summary of experimental systematics to be included for b-tagging of jets in the analysis, using the continuous DL1r tagging algorithm. All of the b-tagging related systematics are applied as event weights. From left: type, description, and the name of systematic used in the fit.

518 Theoretical uncertainties applied to MC predictions, including cross section, PDF, and scale
 519 uncertainties are taken from theory calculations, with the exception of non-prompt and diboson
 520 backgrounds. The cross-section uncertainty on tZ is taken from [29]. Derivation of the non-
 521 prompt background uncertainties, Z+jets and tt}, are explained in detail in Section 6.3. These
 522 normalization uncertainties are chosen so as to account for the complete uncertainty in the
 523 non-prompt contribution, and therefore no additional modelling uncertainties are considered for
 524 Z+jets and tt}.

525 The other VV + heavy flavor processes (namely VV+b and VV+charm, which primarily consist
 526 of ZZ events) are also poorly understood, because these processes involve the same physics as
 527 WZ + heavy flavor, and have also not been measured. Therefore, a conservative 50% uncertainty
 528 is applied to those samples. While this uncertainty is large, it is found to have little impact on
 529 the significance of the final result.

530 The theory uncertainties applied to the predominate background estimates are summarized in
 531 Table 13.

Process	X-section [%]
tZ	X-sec: ± 15.2
t̄ H (aMC@NLO+Pythia8)	QCD Scale: $^{+5.8}_{-9.2}$ PDF($+\alpha_S$): ± 3.6
t̄ Z (aMC@NLO+Pythia8)	QCD Scale: $^{+9.6}_{-11.3}$ PDF($+\alpha_S$): ± 4
t̄ W (aMC@NLO+Pythia8)	QCD Scale: $^{+12.9}_{-11.5}$ PDF($+\alpha_S$): ± 3.4
VV + b/charm (Sherpa 2.2.1)	± 50
VV + light (Sherpa 2.2.1)	± 6
t̄ t	± 20
Z + jets	± 25
Others	± 50

Table 13: Summary of theoretical uncertainties for MC predictions in the analysis.

532 Due to its importance as a background, additional modelling uncertainties are considered for tZ.
 533 Alternative tZ samples with variations in scale (DSID 412064-5) and shower modelling (DSID
 534 501046) are included as systematics..

535 The fit involves varying the overall normalization of signal templates over the regions de-
 536 scribed in Section 6.2, which are defined by the flavor and number of associated jets at truth-
 537 level. The modelling of these template shapes therefore significantly impacts the final result.
 538 Additional signal uncertainties, probing the shape of the signal templates as well as the rate of
 539 migrations between the number of truth-jets and reconstructed jets, are estimated by comparing
 540 estimates from the nominal Sherpa WZ samples with alternative WZ samples generated with
 541 POWHEG+PYTHIA8 (DSID 361601). Separate systematics are included in the fit for WZ + b, WZ
 542 + c and WZ + light, where the distribution among each of the fit regions is varied based on the
 543 prediction of the Powheg sample.

544 The variations in the signal templates are shown in Figures 30 and 31. Each of these plots are
 545 normalized to unity in order to capture the relevant differences in shape.

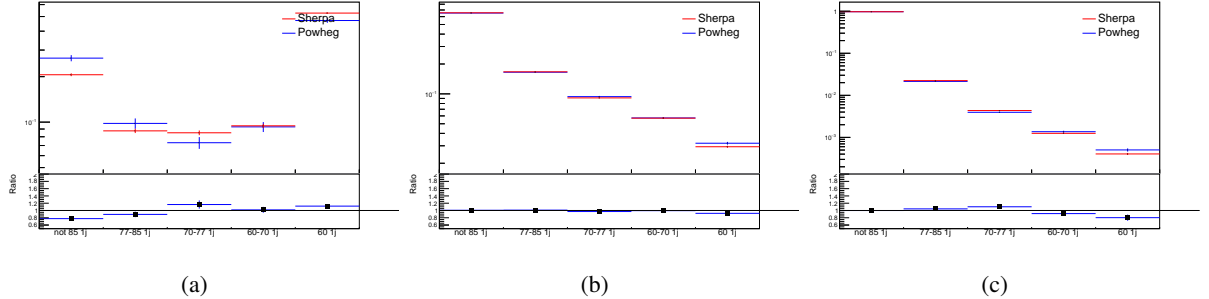


Figure 30: Comparison between Sherpa and Powheg predictions of the distribution of (a) WZ + b, (b) WZ + charm, and (c) WZ + light among the various b-tag WPs used in the 1-jet fit.

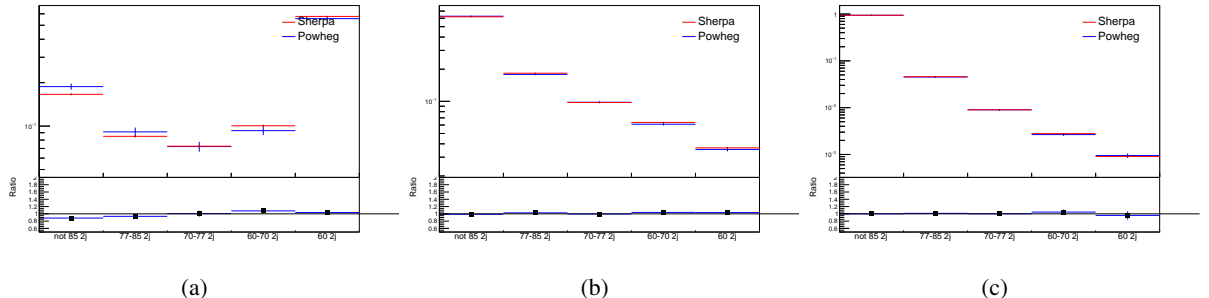


Figure 31: Comparison between Sherpa and Powheg predictions of the distribution of (a) WZ + b, (b) WZ + charm, and (c) WZ + light among the various b-tag WPs used in the 2-jet fit.

546 Separate systematics are included in the fit for WZ + b, WZ + charm and WZ + light, where
 547 the distribution among each of the fit regions is varied based on the prediction of the Powheg
 548 sample.

549 A similar approach is taken to account for uncertainties in migrations between the number of
 550 reco and truth jets. The fraction of events with 1 truth jet which fall into the 1 jet bin versus the
 551 2 jet bin at reco level is compared for Sherpa and Powheg. The same is done for events with 2
 552 truth jets. This comparison is shown in figure 32.

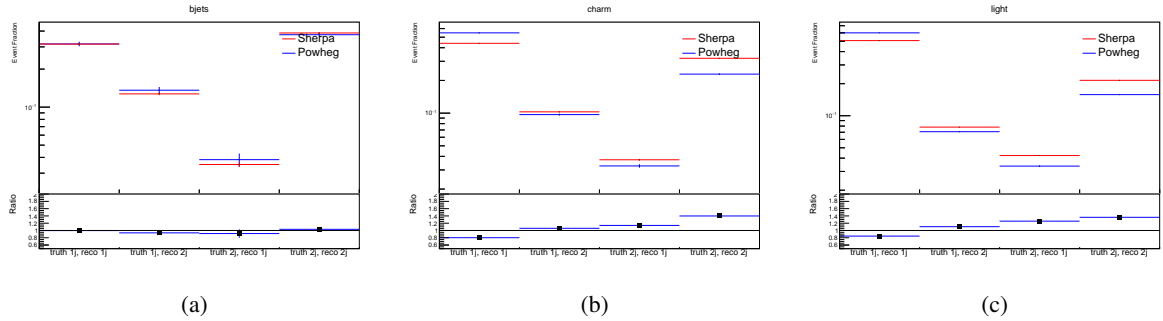


Figure 32: Comparison between Sherpa and Powheg predictions for truth jet migrations between the 1 and 2 jet reco bins for (a) WZ + b, (b) WZ + charm, and (c) WZ + light

553 A systematic is included where events are shifted between the 1-jet and 2-jet regions based on
 554 the differences between these two shapes. This is done independently for each of the WZ + b,
 555 WZ + charm, and WZ + light templates.

556 Additional systematics are included to account for the uncertainty in the contamination of 0 jet
 557 and 3 or more jet events (at truth level) in the 1 and 2 reco jet bins. Because these events fall
 558 outside the scope of this measurement, these events are included as a background. As such, a
 559 normalization, rather than a shape, uncertainty is applied for this background.

560 The number of WZ events with 0-jets and $>=3$ -jets in the reconstructed 1-jet and 2-jet regions
 561 are compared for Sherpa and Powheg, as seen in figure 33. These differences are taken as separate
 562 normalization systematics on the yield of WZ+0-jet and WZ+ $>=3$ -jet events.

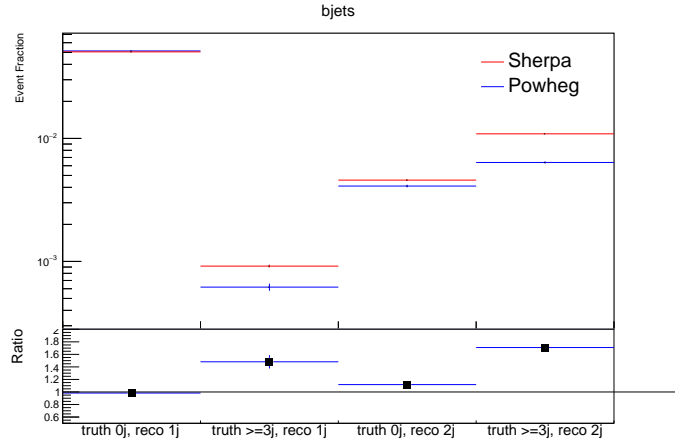


Figure 33: Comparison between Sherpa and Powheg predictions for 0 and $>=3$ truth jet contributions in the 1 and 2 jet reco bins

563 8 Results

564 8.1 Fit Procedure

565 A maximum-likelihood fit is performed over the unfolded signal templates in the various fit
 566 regions described in Section 6 in order to extract the best-fit value of the WZ + b-jet and WZ +
 567 charm jet contributions for events with both 1 and 2 associated jets.

568 Because the fit regions are defined by the number of associated jets at reco-level, an unfolding
 569 procedure is applied to the signal in order to account for differences in the number of truth jets
 570 compared to the number of reco-jets. The WZ + b, WZ + charm and WZ + light contributions
 571 are separated into independent samples based on the number of truth jets in each event. WZ + 1
 572 truth-jet and WZ + 2 truth-jets are treated as signal samples, while WZ + 0 truth-jets and WZ +
 573 ≥ 3 truth-jets are treated as an additional background.

574 A maximum likelihood fit to data is performed simultaneously in the regions described in Section
 575 6, summarized in figure 34. The six signal templates, which include WZ+b 1-jet, WZ+c 1-jet,
 576 WZ+l 1-jet, WZ+b 2-jets, WZ+c 2-jets, WZ+l 2-jets, are allowed to float, while the remaining
 577 background contributions are held fixed. The parameters $\mu_{WZ+b-1-jet}$, $\mu_{WZ+charm1-jet}$,
 578 $\mu_{WZ+light-1-jet}$, $\mu_{WZ+b-2-jet}$, $\mu_{WZ+charm2-jet}$, $\mu_{WZ+light-2-jet}$, where $\mu = \sigma_{\text{observed}}/\sigma_{\text{SM}}$,
 579 are extracted from the fit. A simultaneous fit is performed over all 1-jet and 2-jet regions.

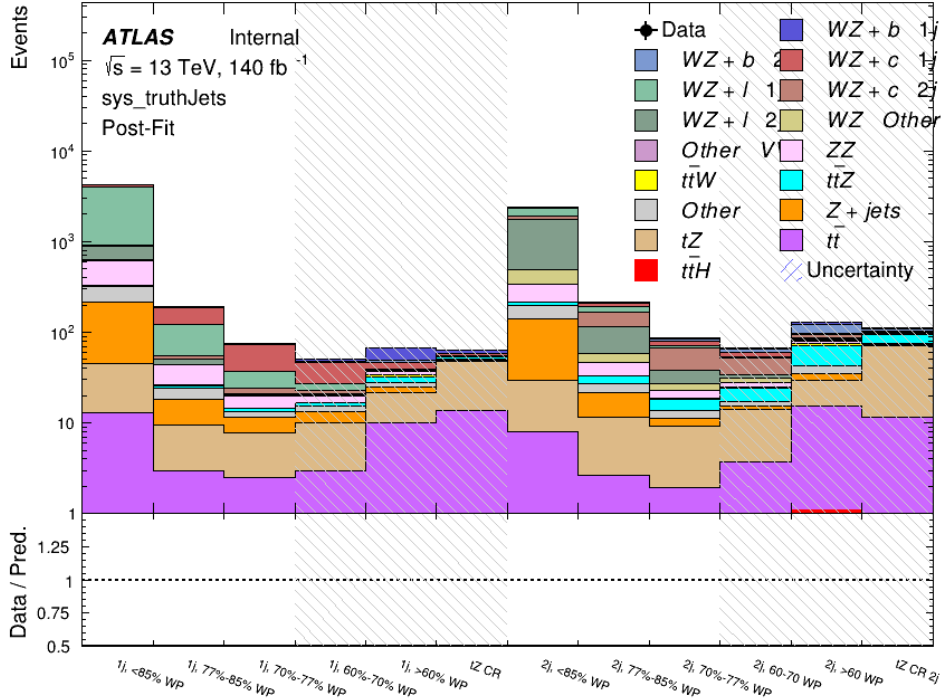


Figure 34: Post-fit summary of the fit regions.

- 580 As described in Section 7, there are 235 systematic uncertainties that are considered as NPs in
 581 the fit. These NPs are constrained by Gaussian or log-normal probability density functions. The
 582 latter are used for normalisation factors to ensure that they are always positive. The expected
 583 number of signal and background events are functions of the likelihood. The prior for each NP
 584 is added as a penalty term, decreasing the likelihood as it is shifted away from its nominal value.
 585 The correlations between these nuisance parameters are summarized in Figure ??.
- 586 Several alternative fit strategies are documented in Appendices 8.3-8.4.1. These include a
 587 measurement of WZ + 1 or 2 jets inclusively, a fit where tZ is allowed to float, and a case where
 588 tZ is included as part of the signal.

589 8.2 Results of the Simultaneous Fit

- 590 The Asimov fit for 1-jet events gives an expected μ value of $1.00^{+0.47}_{-0.43}(\text{stat})^{+0.30}_{-0.27}(\text{sys})$ for WZ
 591 + b. The normalization factors extracted from the fit for WZ + charm and WZ + light are
 592 $1.00 \pm 0.17 \pm 0.17$ and $1.00 \pm 0.06 \pm 0.14$, respectively.
- 593 The expected cross-section of WZ+b with 1-jet in the fiducial region outlined in Section 2
 594 is $1.74^{+0.82}_{-0.75}(\text{stat})^{+0.53}_{-0.48}(\text{sys}) \text{ fb}$, and $14.6 \pm 2.5(\text{stat}) \pm 2.3(\text{sys}) \text{ fb}$ for WZ + charm, with a

595 correlation of -0.15 between them. An expected significance of 2.0 is observed for WZ + b in
 596 this region.

597 For 2-jet events, the fit gives an expected μ value of $1.00^{+0.53}_{-0.51}(\text{stat})^{+0.39}_{-0.34}(\text{sys})$ for WZ + b.
 598 The fitted cross-section modifiers for WZ + charm and WZ + light are $1.00 \pm 0.25 \pm 0.21$ and
 599 $1.00 \pm 0.06 \pm 0.16$, respectively.

600 The expected WZ + b cross-section in the fiducial region with 2 associated jets is $2.5^{+1.3}_{-1.3}(\text{stat})^{+0.95}_{-0.83}(\text{sys})$
 601 fb with an expected significance of 1.7σ . The 2-jet expected cross-section of WZ + charm is
 602 $12.7 \pm 3.2(\text{stat}) \pm 2.7(\text{sys})$ fb, and the correlation between WZ + charm and WZ + b is -0.22.

603 The results of the fit to an Asimov dataset for the fiducial regions considered, including both the
 604 normalization factors as well as the expected cross-sections, along with their uncertainties, are
 605 summarized in Table 14.

606

Process	μ	σ
WZ + b - 1-jet	$1.00^{+0.47}_{-0.43}(\text{stat})^{+0.30}_{-0.27}(\text{sys})$	$1.74^{+0.82}_{-0.75}(\text{stat})^{+0.53}_{-0.48}(\text{sys})$ fb
WZ + c - 1-jet	$1.00 \pm 0.17(\text{stat}) \pm 0.17(\text{sys})$	$14.6 \pm 2.5(\text{stat}) \pm 2.3(\text{sys})$ fb
WZ + b - 2-jet	$1.00^{+0.53}_{-0.51}(\text{stat})^{+0.39}_{-0.34}(\text{sys})$	$2.5^{+1.3}_{-1.3}(\text{stat})^{+0.95}_{-0.83}(\text{sys})$ fb
WZ + c - 2-jet	$1.00^{+0.25}_{-0.24}(\text{stat})^{+0.32}_{-0.27}(\text{sys})$	$12.7^{+3.3}_{-3.2}(\text{stat})^{+3.9}_{-3.4}(\text{sys})$ fb

Table 14: Normalization factors and cross-sections extracted from the fit for each of the fiducial regions considered

607 An expected significance of 2.0σ is observed for WZ + b with 1-jet, and 1.7σ for WZ + b with
 608 two jets. A summary of the correlations between these various measurements is shown in Figure
 609 35.

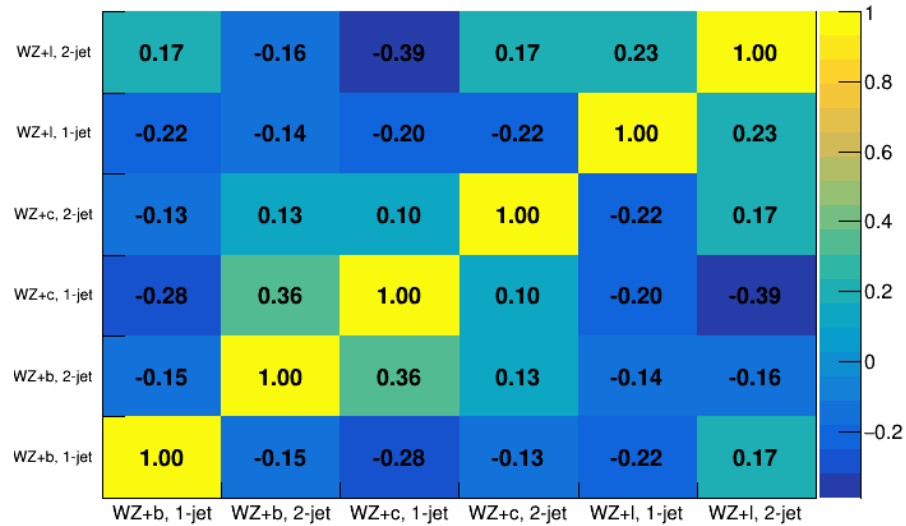


Figure 35: Correlations between the various measured components of WZ.

610 The pre-fit yields in each of the 1-jet regions used in the fit are shown in Table 15.

611

Sample	1j, <85% WP	1j, 77%-85% WP	1j, 70%-77% WP	1j, 60%-70% WP	1j, 60%+ WP	tZ CR
WZ + b – 1j	8.1 ± 1.6	4.7 ± 0.5	4.6 ± 0.4	5.1 ± 0.4	18.1 ± 2.4	5.0 ± 0.6
WZ + c – 1j	260 ± 22	81 ± 6	43.1 ± 3.6	25.8 ± 2.6	9.4 ± 1.8	2.9 ± 0.6
WZ + l – 1j	3090 ± 250	91 ± 13	17 ± 3	4.9 ± 1.6	1.3 ± 0.4	0.2 ± 0.1
WZ + b – 2j	1.10 ± 0.37	0.44 ± 0.11	0.39 ± 0.06	0.62 ± 0.14	2.1 ± 0.5	0.59 ± 0.14
WZ + c – 2j	21 ± 5	5.6 ± 1.2	3.0 ± 0.7	2.0 ± 0.5	0.70 ± 0.20	0.30 ± 0.08
WZ + l – 2j	250 ± 60	5.7 ± 1.6	0.73 ± 0.53	0.31 ± 0.15	0.07 ± 0.06	0.01 ± 0.01
WZ – Other	13 ± 5	1.4 ± 0.4	0.42 ± 0.08	0.2 ± 0.01	0.30 ± 0.05	0.67 ± 0.15
Other VV	6.2 ± 0.6	0.2 ± 0.4	0.2 ± 0.04	0.07 ± 0.1	0.1 ± 0.1	0.1 ± 0.2
ZZ	336 ± 26	17.8 ± 2.1	4.3 ± 0.6	1.7 ± 0.5	0.36 ± 0.08	0.10 ± 0.03
t <bar>t>W</bar>	1.1 ± 0.2	0.2 ± 0.1	0.3 ± 0.1	0.4 ± 0.1	1.5 ± 0.3	0.7 ± 0.2
t <bar>t>Z</bar>	6.8 ± 1.2	1.4 ± 0.3	1.0 ± 0.2	1.2 ± 0.2	4.4 ± 0.8	3.2 ± 0.6
Z + jets	169 ± 38	8.9 ± 1.9	3.7 ± 0.8	3.3 ± 0.7	3.2 ± 0.7	0.8 ± 0.17
V + γ	45 ± 28	1.9 ± 2.4	0.1 ± 0.1	0.02 ± 0.01	1.0 ± 0.9	0.02 ± 0.03
tZ	31.8 ± 4.3	6.4 ± 1.1	5.3 ± 0.8	7.2 ± 1.1	11.8 ± 2.0	33.9 ± 4.5
tW	1.4 ± 0.8	0.2 ± 0.5	0.0 ± 0.2	0.7 ± 0.6	0.26 ± 0.42	0.39 ± 0.41
WtZ	2.3 ± 1.2	0.6 ± 0.3	0.3 ± 0.21	0.27 ± 0.2	1.1 ± 0.7	0.6 ± 0.5
VVV	12.4 ± 0.5	0.93 ± 0.06	0.35 ± 0.03	0.13 ± 0.02	0.14 ± 0.03	0.02 ± 0.01
VH	40 ± 6	2.6 ± 1.4	0.9 ± 0.8	0.7 ± 0.8	0.5 ± 0.6	0.0 ± 0.0
t <bar>t></bar>	12.1 ± 1.6	2.9 ± 0.6	2.5 ± 0.5	2.8 ± 0.5	11.2 ± 1.4	10.9 ± 1.5
t <bar>t>H</bar>	0.24 ± 0.03	0.05 ± 0.01	0.04 ± 0.01	0.06 ± 0.01	0.20 ± 0.03	0.13 ± 0.02
Total	5010 ± 260	227 ± 24	88 ± 12	57 ± 8	76 ± 16	53 ± 8

Table 15: Pre-fit yields in each of the 1-jet regions.

⁶¹² Here <85% includes jets that fail to pass the 85% WP, and 60%+ includes jets that pass the highest, 60%, WP. The post-fit yields in each region are summarized in Table 16.

⁶¹⁴

	1j, <85% WP	1j, 77%-85% WP	1j, 70%-77% WP	1j, 60%-70% WP	1j, 60%+ WP	tZ CR
WZ + b – 1j	8.1 ± 4.9	4.7 ± 2.0	4.6 ± 2.0	5.1 ± 2.1	18 ± 10	5.0 ± 2.5
WZ + c – 1j	260 ± 60	80 ± 14	43 ± 7	26 ± 5	7.4 ± 2.3	2.1 ± 0.7
WZ + l – 1j	3090 ± 130	90 ± 11	17.3 ± 2.8	4.9 ± 1.6	1.3 ± 0.4	0.23 ± 0.13
WZ + b – 2j	1.10 ± 0.37	0.44 ± 0.11	0.39 ± 0.06	0.62 ± 0.14	2.1 ± 0.5	0.59 ± 0.14
WZ + c – 2j	21 ± 5	5.6 ± 1.2	3.0 ± 0.7	2.0 ± 0.5	0.70 ± 0.20	0.30 ± 0.08
WZ + l – 2j	250 ± 60	5.7 ± 1.6	0.73 ± 0.53	0.31 ± 0.15	0.07 ± 0.06	0.01 ± 0.01
WZ – Other	13 ± 5	1.4 ± 0.4	0.42 ± 0.08	0.2 ± 0.01	0.30 ± 0.05	0.67 ± 0.15
Other VV	6.2 ± 0.6	0.92 ± 0.07	0.02 ± 0.01	0.01 ± 0.01	0.01 ± 0.01	0.01 ± 0.01
ZZ	346 ± 57	19 ± 5	4.3 ± 0.8	2.7 ± 0.5	2.4 ± 0.1	2.1 ± 0.6
t̄tW	1.09 ± 0.21	0.2 ± 0.1	0.1 ± 0.1	0.4 ± 0.1	1.5 ± 0.3	0.1 ± 0.2
t̄tZ	6.8 ± 1.2	1.4 ± 0.3	1.0 ± 0.2	1.2 ± 0.2	4.4 ± 0.7	3.2 ± 0.5
rare Top	0.14 ± 0.04	0.04 ± 0.02	0.04 ± 0.0	0.1 ± 0.03	0.14 ± 0.04	0.15 ± 0.05
t̄tWW	0.04 ± 0.03	0.01 ± 0.02	0.01 ± 0.01	0.01 ± 0.01	0.01 ± 0.02	0.01 ± 0.01
Z + jets	169 ± 37	8.9 ± 1.9	3.7 ± 0.8	3.3 ± 0.7	3.2 ± 0.7	0.8 ± 0.2
W + jets	0.01 ± 0.01					
V + γ	46 ± 28	1.9 ± 2.4	0.1 ± 0.1	0.0 ± 0.2	1.0 ± 0.9	0.0 ± 0.0
tZ	31 ± 4	6.0 ± 1.0	5.3 ± 0.8	7.2 ± 1.0	11.8 ± 1.8	33.9 ± 4.5
tW	1.37 ± 0.82	0.18 ± 0.26	0.01 ± 0.12	0.67 ± 0.64	0.26 ± 0.42	0.39 ± 0.41
WtZ	2.3 ± 1.2	0.6 ± 0.3	0.3 ± 0.2	0.3 ± 0.2	1.1 ± 0.6	0.6 ± 0.3
VVV	12.4 ± 0.4	0.9 ± 0.1	0.4 ± 0.1	0.13 ± 0.02	0.14 ± 0.03	0.02 ± 0.01
VH	40 ± 6	2.6 ± 1.4	0.9 ± 0.8	0.7 ± 0.8	0.4 ± 0.6	0.01 ± 0.01
t̄t	12.1 ± 1.6	2.9 ± 0.6	2.5 ± 0.5	2.8 ± 0.5	11.2 ± 1.5	10.9 ± 1.4
t̄tH	0.24 ± 0.03	0.05 ± 0.01	0.04 ± 0.01	0.06 ± 0.01	0.20 ± 0.03	0.13 ± 0.02
Total	5100 ± 110	227 ± 12	87 ± 6	56.7 ± 4.4	76 ± 9	52.5 ± 4.2

Table 16: Post-fit yields in each of the 1-jet regions.

615 The impact of each NP is calculated by performing the fit with the parameter of interest held
 616 fixed, varied from its fitted value by its uncertainty, and calculating $\Delta\mu$ relative to the baseline
 617 fit. The impact of the most significant sources of systematic uncertainties on WZ + b with one
 618 associated jet is summarized in Table 17.

Uncertainty Source	$\Delta\mu$	
WZ + 1-jet light cross-section	0.13	-0.15
WZ + 1-jet charm cross-section	-0.10	0.12
Jet Energy Scale	0.1	-0.13
Other Diboson + b cross-section	-0.09	0.09
tZ cross-section	-0.08	0.08
WZ 1-jet/2-jet Migration	0.08	-0.07
Jet Energy Resolution	-0.07	0.08
Luminosity	-0.06	0.07
Flavor tagging	0.05	0.05
t <bar>t} cross-section</bar>	-0.05	0.05
Total Systematic Uncertainty	0.28	0.33

Table 17: Summary of the most significant sources of systematic uncertainty on the measurement of WZ + b with exactly one associated jet.

Uncertainty Source	$\Delta\sigma/\sigma_{\text{nominal}}$	
WZ + c 1j/2j migration	0.12	-0.09
Flavor Tagging	0.09	0.08
WZ + b, 1-jet cross-section	-0.04	0.05
Luminosity	-0.04	0.04
Jet Energy Resolution	0.04	0.04
WZ + b, 2-jet cross-section	0.04	-0.03
WZ cross-section - QCD scale	-0.04	0.04
Jet Energy Scaling	0.04	0.02
WZ cross-section - PDF	-0.03	0.03
WZ + light, 1-jet cross-section	0.03	-0.03
total	0.1879	0.1753

Table 18: Summary of the most significant sources of systematic uncertainty on the measurement of WZ + c with exactly one associated jet.

619 The ranking and impact of those nuisance parameters with the largest contribution to the overall
 620 uncertainty is shown in Figure 36.

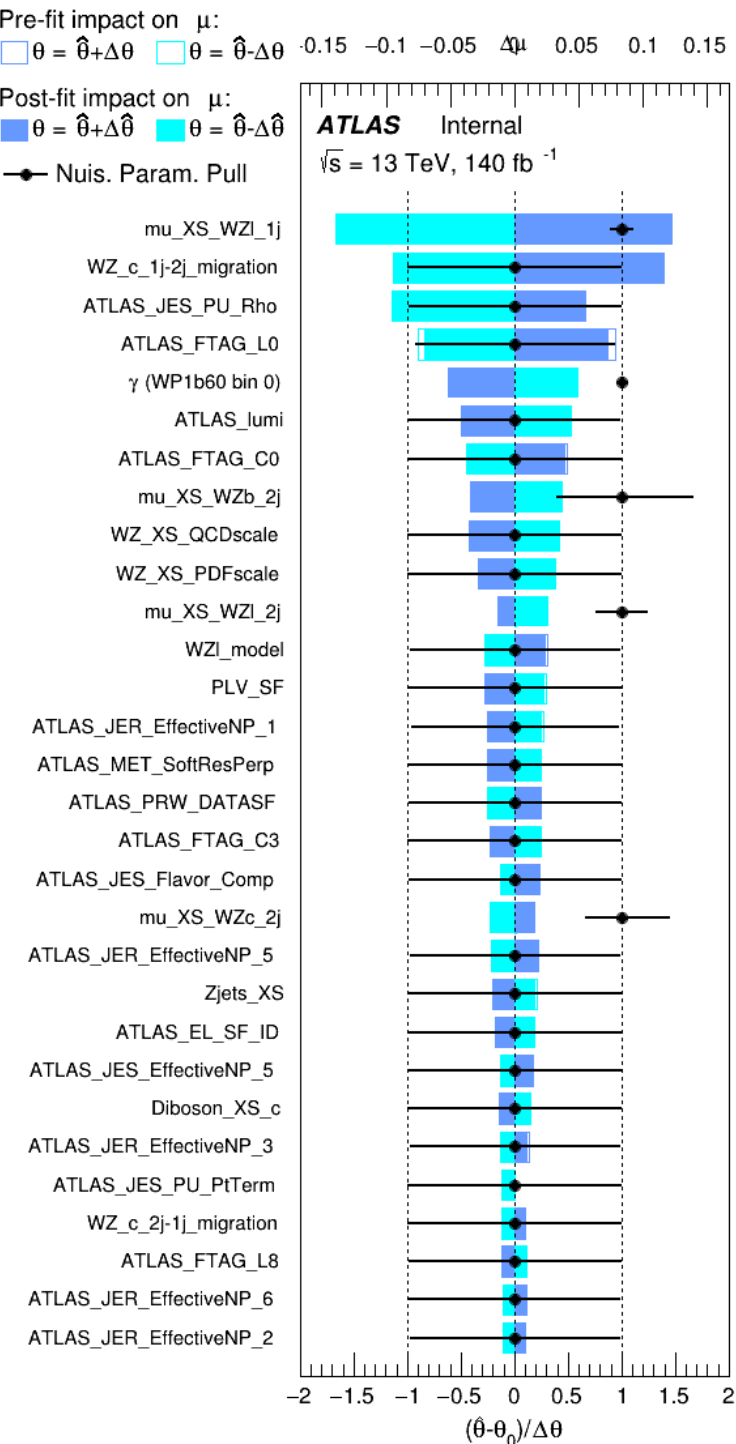


Figure 36: Impact of systematic uncertainties on the signal-strength of $WZ + b$ for events with exactly one jet

621 The large impact of the Jet Energy Scale and Jet Flavor Tagging is unsurprising, as the definition
 622 of the fit regions depends heavily on the modeling of the jets. The other major sources of
 623 uncertainty come from background modelling and cross-section uncertainty.

624 Pre-fit yields in each of the 2-jet fit are shown in Table 19.

	2j, <85% WP	2j, 77%-85% WP	2j, 70%-77% WP	2j, 60%-70% WP	2j, 60%+ WP	tZ CR 2j
WZ + b - 2j	3.1 ± 1.6	6.7 ± 0.5	5.6 ± 0.4	8.0 ± 0.6	24 ± 2	5 ± 1
WZ + c - 2j	180 ± 20	54 ± 6	41 ± 3	24 ± 3	17 ± 2	7.0 ± 0.6
WZ + l - 2j	1250 ± 150	90 ± 14	18 ± 3	5.8 ± 1.4	1.4 ± 0.4	0.25 ± 0.15
WZ + b - 1j	3.4 ± 0.6	1.52 ± 0.35	1.58 ± 0.23	1.95 ± 0.39	7.8 ± 1.1	0.8 ± 0.6
WZ + c - 1j	56 ± 14	17.6 ± 4.0	8.6 ± 2.2	6.3 ± 1.8	3.0 ± 0.9	0.7 ± 0.2
WZ + l - 1j	427 ± 120	24 ± 7	4.7 ± 2.3	1.6 ± 0.7	0.3 ± 0.2	0.01 ± 0.01
WZ - Other	129 ± 29	6.1 ± 4.6	1.2 ± 0.3	0.3 ± 0.2	2.9 ± 0.5	3.6 ± 0.6
Other VV	7.63 ± 0.63	0.6 ± 0.5	0.16 ± 0.03	0.01 ± 0.01	0.1 ± 0.1	0.1 ± 0.1
ZZ	135 ± 20	14.1 ± 3.2	4.7 ± 0.8	4.0 ± 0.6	4.1 ± 0.7	3.1 ± 0.5
t̄W	0.8 ± 0.2	0.4 ± 0.1	0.5 ± 0.1	0.7 ± 0.2	4.3 ± 0.6	3.9 ± 0.6
t̄Z	14.7 ± 2.2	5.6 ± 0.8	4.5 ± 0.7	6.5 ± 1.1	25.4 ± 4.0	21.9 ± 3.4
rare Top	0.14 ± 0.04	0.07 ± 0.03	0.03 ± 0.02	0.09 ± 0.03	0.37 ± 0.07	0.6 ± 0.1
t̄WW	0.04 ± 0.03	0.02 ± 0.02	0.01 ± 0.01	0.01 ± 0.00	0.03 ± 0.03	0.01 ± 0.01
Z + jets	110.0 ± 22.9	9.6 ± 2.0	2.1 ± 0.50	1.6 ± 0.4	5.1 ± 1.1	1.5 ± 0.3
W + jets	0.0 ± 0.0	0.0 ± 0.0	0.0 ± 0.0	0.0 ± 0.0	0.0 ± 0.0	0.0 ± 0.0
V + γ	25 ± 18	0.5 ± 0.2	0.1 ± 0.1	0.1 ± 0.1	0.0 ± 0.02	0.05 ± 0.07
tZ	21.9 ± 2.9	9.6 ± 1.3	9.1 ± 1.0	10.0 ± 1.5	14.7 ± 3.2	60 ± 6
tW	0.9 ± 0.7	0.2 ± 0.3	0.0 ± 0.1	0.0 ± 0.0	0.8 ± 0.6	0.2 ± 0.2
WtZ	4.9 ± 2.5	1.5 ± 0.8	1.1 ± 0.6	1.3 ± 0.7	4.6 ± 2.4	3.3 ± 1.7
VVV	7.4 ± 0.3	1.0 ± 0.1	0.4 ± 0.1	0.2 ± 0.1	0.13 ± 0.03	0.04 ± 0.01
VH	19.5 ± 4.2	2.8 ± 1.6	0.7 ± 0.7	0.1 ± 0.2	0.0 ± 0.0	0.0 ± 0.0
t̄t	0.7 ± 0.4	0.1 ± 0.1	0.05 ± 0.06	0.15 ± 0.13	0.8 ± 0.5	2.3 ± 1.2
t̄t̄	6.8 ± 1.0	2.4 ± 0.5	1.8 ± 0.4	3.3 ± 0.6	8.4 ± 1.2	13.6 ± 1.7
t̄tH	0.4 ± 0.1	0.2 ± 0.1	0.16 ± 0.02	0.23 ± 0.03	0.94 ± 0.11	1.03 ± 0.12
Total	2580 ± 160	229 ± 24	89 ± 13	69 ± 11	120 ± 15	108 ± 11

Table 19: Pre-fit yields in each of the 2-jet regions.

625 The post-fit yields in each region are summarized in Table 20.

	2j, <85% WP	2j, 77%-85% WP	2j, 70%-77% WP	2j, 60%-70% WP	2j, 60%+ WP	tZ CR 2j
WZ + b	13 ± 6	6.7 ± 2.9	5.8 ± 2.5	8.0 ± 3.5	31 ± 13	14 ± 5
WZ + c	260 ± 60	77 ± 15	41 ± 8	26 ± 5	10.9 ± 2.4	4.8 ± 1.1
WZ + l	1860 ± 90	90 ± 12	17.6 ± 2.8	5.8 ± 1.3	1.4 ± 0.4	0.3 ± 0.2
WZ + b - 1j	3.4 ± 0.6	1.52 ± 0.35	1.58 ± 0.23	1.95 ± 0.39	6.7 ± 1.1	1.9 ± 0.6
WZ + c - 1j	56 ± 14	17.6 ± 4.0	8.6 ± 2.2	6.3 ± 1.8	3.0 ± 0.9	0.7 ± 0.2
WZ + l - 1j	427 ± 120	24 ± 7	4.7 ± 2.3	1.6 ± 0.7	0.3 ± 0.2	0.01 ± 0.01
WZ - Other	129 ± 29	6.1 ± 4.6	1.2 ± 0.3	0.3 ± 0.2	2.9 ± 0.5	3.6 ± 0.6
Other VV	7.6 ± 0.6	0.3 ± 0.3	0.3 ± 0.1	0.1 ± 0.06	0.03 ± 0.02	0.1 ± 0.1
ZZ	145 ± 30	11.3 ± 4.4	2.7 ± 1.6	1.0 ± 0.3	4.0 ± 0.1	2.4 ± 0.1
t̄tW	0.8 ± 0.2	0.4 ± 0.1	0.54 ± 0.12	0.74 ± 0.15	4.3 ± 0.6	3.9 ± 0.6
t̄tZ	14.7 ± 2.2	5.6 ± 0.8	4.5 ± 0.7	6.5 ± 1.0	25.4 ± 3.9	21.9 ± 3.3
rare Top	0.14 ± 0.04	0.07 ± 0.03	0.03 ± 0.02	0.09 ± 0.03	0.4 ± 0.1	0.6 ± 0.1
t̄tWW	0.04 ± 0.03	0.02 ± 0.02	0.01 ± 0.01	0.01 ± 0.01	0.03 ± 0.03	0.01 ± 0.01
Z + jets	110 ± 23	9.6 ± 2.0	2.1 ± 0.5	1.6 ± 0.4	5.1 ± 1.1	1.5 ± 0.3
W + jets	0.0 ± 0.0					
V + γ	25 ± 19	0.5 ± 0.2	0.1 ± 0.1	0.13 ± 0.14	0.0 ± 0.02	0.05 ± 0.07
tZ	21.9 ± 2.7	9.6 ± 1.2	7.1 ± 0.9	10.0 ± 1.4	14.7 ± 3.0	60 ± 6
tW	0.1 ± 0.7	0.2 ± 0.3	0.0 ± 0.1	0.0 ± 0.0	0.8 ± 0.6	0.2 ± 0.2
WtZ	4.9 ± 2.5	1.5 ± 0.8	1.1 ± 0.6	1.3 ± 0.7	4.6 ± 2.3	3.3 ± 1.7
VVV	7.4 ± 0.3	1.0 ± 0.1	0.36 ± 0.03	0.19 ± 0.03	0.13 ± 0.03	0.04 ± 0.01
VH	19 ± 4	2.8 ± 1.6	0.7 ± 0.7	0.1 ± 0.2	0.0 ± 0.0	0.0 ± 0.0
t̄t	6.8 ± 1.0	2.4 ± 0.5	1.8 ± 0.4	3.3 ± 0.6	8.4 ± 1.2	13.6 ± 1.7
t̄tH	0.40 ± 0.05	0.19 ± 0.03	0.16 ± 0.02	0.23 ± 0.03	0.94 ± 0.11	1.03 ± 0.11
Total	2580 ± 60	229 ± 11	89 ± 6	69.1 ± 4.1	120 ± 10	108 ± 6

Table 20: Post-fit yields in each of the 2-jet regions.

626 The same set of systematic uncertainties consider for the 1-jet fit are included in the 2-jet fit as
 627 well. The impact of the most significant systematic uncertainties is summarized in Table 21.

Uncertainty Source	$\Delta\mu$	
WZ + c 2-jet cross-section	-0.13	0.16
WZ + l 2-jet cross-section	0.12	-0.09
ttZ cross-section - QCD scale	-0.10	0.13
WZ + b 1-jet cross-section	-0.11	0.10
Jet Energy Scale	-0.11	0.11
Luminosity	-0.11	0.12
tZ cross-section	-0.11	0.11
WtZ cross-section	-0.07	0.07
Flavor tagging	0.05	0.05
Other VV + b cross-section	-0.05	0.05
Total	0.35	0.37

Table 21: Summary of the most significant sources of systematic uncertainty on the measurement of WZ + b 2-jet events.

Uncertainty Source	$\Delta\sigma/\sigma_{\text{nominal}}$	
WZ + c 1j/2j migration	-0.17	0.25
Flavor Tagging	0.14	0.13
WZ + b, 1-jet cross-section	-0.09	0.09
Jet Energy Scale	0.06	0.08
Jet Energy Resolution	0.05	0.05
WZ $\geq 3j/2j$ migration	-0.04	0.04
WZ + c 2j/1j migration	-0.04	0.04
WZ cross-section - QCD scale	-0.04	0.04
WZ + light modelling	0.04	-0.03
Luminosity	-0.03	0.03
total	0.2694	0.3274

Table 22: Summary of the most significant sources of systematic uncertainty on the measurement of WZ + c with 2 associated jets.

628 The ranking and impact of those nuisance parameters with the largest contribution to the overall
 629 uncertainty is shown in Figure 37.

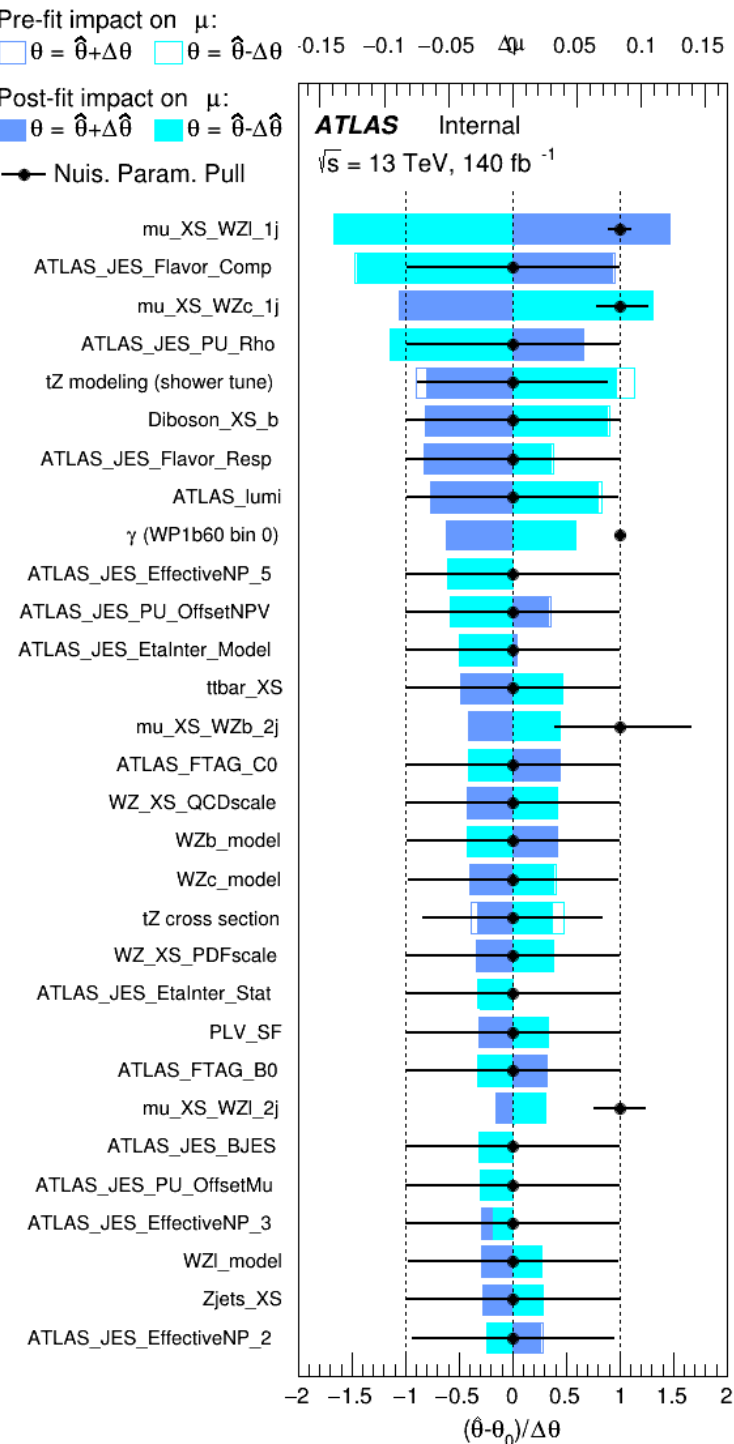


Figure 37: Impact of systematic uncertainties on the signal-strength of $WZ + b$ in 2-jet events.

630 The large impact of the Jet Energy Scale and Jet Flavor Tagging is unsurprising, as the shape of
631 the fit regions depends heavily on the modeling of the jets. The other major sources of uncertainty
632 come from background modelling and cross-section uncertainty.

633 **8.3 Inclusive 1+2 Jet Fit**

634 An alternative fit is performed which combines the WZ + 1-jet and WZ + 2-jet samples rather than
635 fitting them independently. This is done primarily as a cross-check of the nominal analysis, to
636 see if measuring 1-jet and 2-jet events separately and combining them gives drastically different
637 results than measuring them together.

638 For this study, three signal templates, WZ + b, WZ + charm and WZ + light, are fit to data, and
639 the systematics accounting for migrations between 1-jet and 2-jet bins are removed. All other
640 background and nuisance parameters remain the same as the nominal fit.

641 The measured μ value for WZ + b is $\mu = 1.00^{+0.30}_{-0.29}(\text{stat})^{+0.25}_{-23}(\text{sys})$, with a significance of 2.8σ ,
642 and the uncertainty on WZ + charm is $\mu = 1.00 \pm 0.12(\text{stat}) \pm 0.13(\text{sys})$. This is compared to
643 combined uncertainty of $\mu = 1.00^{+0.32}_{-0.30}(\text{stat})^{+0.24}_{-23}(\text{sys})$ for WZ + b when 1-jet and 2-jet events
644 are measured separately and then combined.

645 A post-fit summary plot of the fit regions is shown in Figure 38:

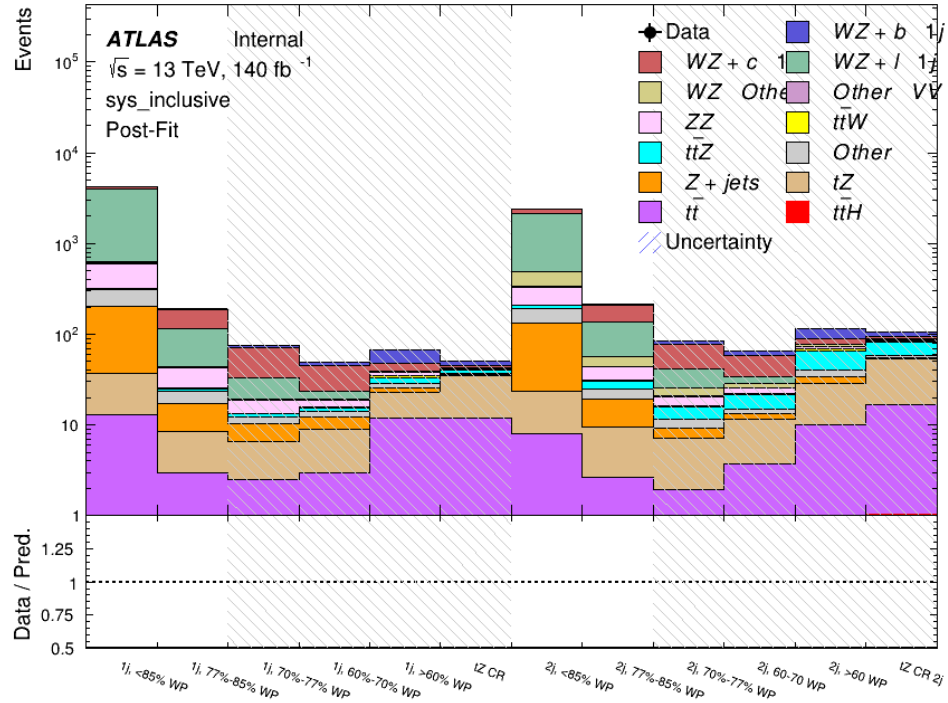


Figure 38: Post-fit summary of the 1-jet fit regions.

646 The impact of the most significant sources of systematic uncertainties on the measurement of
 647 WZ+b is summarized in Table 23.

Uncertainty Source	$\Delta\mu$	
WZ + light cross-section	0.13	-0.12
WZ + charm cross-section	-0.10	0.12
Jet Energy Scale	0.08	0.13
tZ cross-section	-0.10	0.10
Jet Energy Resolution	-0.10	0.10
Luminosity	-0.08	0.09
Other Diboson + b cross-section	-0.07	0.07
Flavor tagging	0.05	0.05
t <bar>t</bar>	-0.05	0.05
WZ cross-section - QCD scale	-0.04	0.03
Total Systematic Uncertainty	0.28	0.32

Table 23: Summary of the most significant sources of systematic uncertainty on the measurement of WZ + b with one or two associated jets.

648 The ranking and impact of those nuisance parameters with the largest contribution to the overall
649 uncertainty is shown in Figure 39.

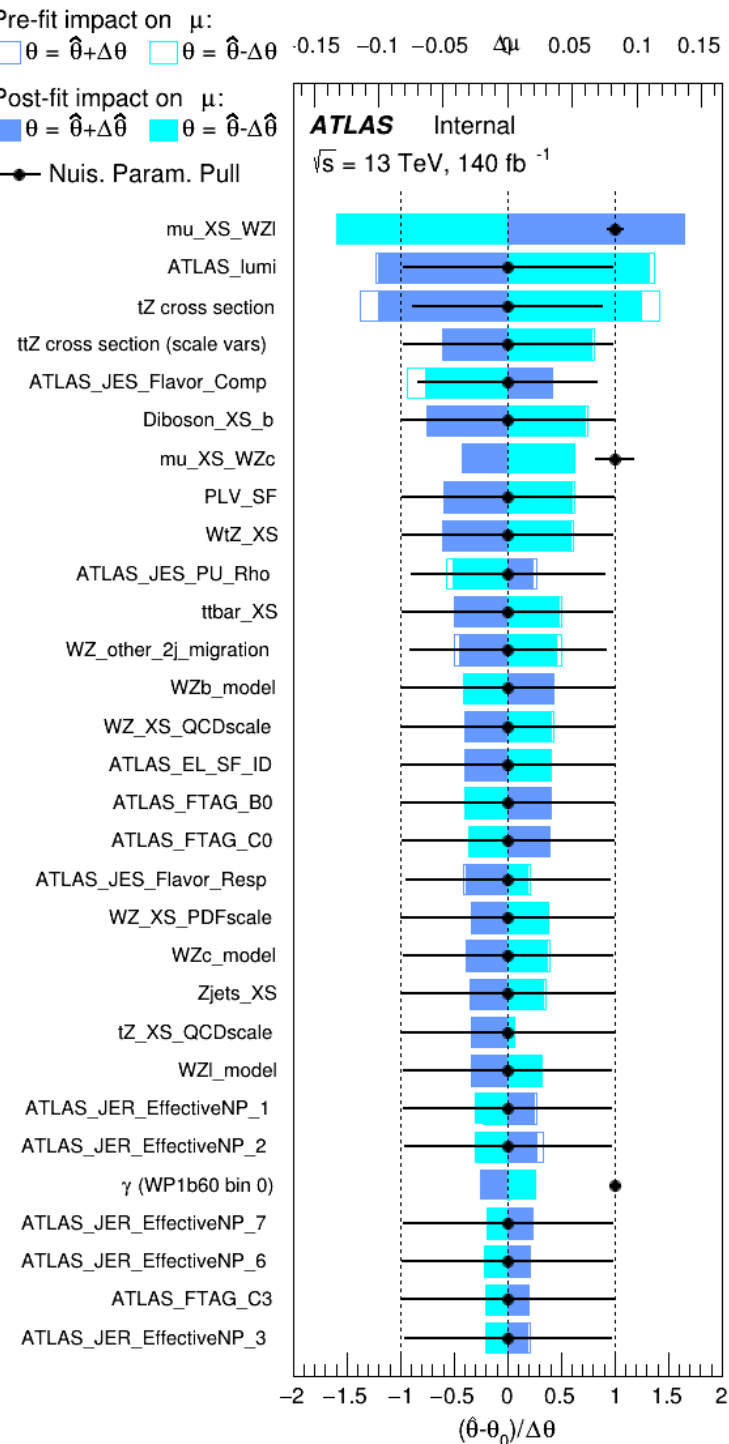


Figure 39: Impact of systematic uncertainties on the signal-strength of $WZ + b$ for events with one or two jets

650 **8.4 Alternate tZ Inclusive Fit**

651 **8.4.1 tZ Inclusive Fit**

652 While tZ is often considered as a distinct process from WZ + b, this could also be considered part
653 of the signal. Alternate studies are performed where, using the same framework as the nominal
654 analysis, a measurement of WZ + b is performed that includes tZ as part of WZ+b.

655 Because of this change, the tZ CR is no longer necessary, and only the five pseudo-continuous
656 b-tag regions are used in the fit. Further, systematics related to the tZ cross-section are removed
657 from the fit, as they are now encompassed by the normalization measurement of WZ + b. All
658 other systematic uncertainties are carried over from the nominal analysis.

659 An expected WZ + b cross-section of $4.1^{+0.78}_{-0.74}(\text{stat})^{+0.53}_{-0.52}(\text{sys}) \text{ fb}$ is extracted from the fit, with
660 an expected significance of 4.0σ .

661 The impact of the predominate systematics are summarized in Table 24.

Uncertainty Source	$\Delta\mu$	
WZ + light cross-section	0.08	-0.08
Jet Energy Scale	-0.06	0.08
Luminosity	-0.05	0.06
WZ + charm cross-section	-0.04	0.05
Other Diboson + b cross-section	-0.04	0.04
WZ cross-section - QCD scale	-0.04	0.03
t̄t cross-section	-0.03	0.03
Jet Energy Resolution	-0.03	0.03
Flavor tagging	-0.03	0.03
Z+jets cross section	-0.02	0.02
Total Systematic Uncertainty	-0.15	0.16

Table 24: Summary of the most significant sources of systematic uncertainty on the measurement of WZ + b with exactly one associated jet.

662 **8.4.2 Floating tZ**

663 In order to quantify the impact of the tZ uncertainty on the fit, an alternative fit strategy is
664 used where the tZ normalization is allowed to float. This normalization factor replaces the
665 cross-section uncertainty on tZ, and all other parameters of the fit remain the same.

666 An uncertainty of 17% on the normalization of tZ is extracted from the fit, compared to a theory
667 uncertainty of 15% applied to the tZ cross-section. The measured uncertainties on WZ remain
668 the same.

669 9 Conclusion

670 A measurement of WZ + heavy flavor is performed using 140 fb^{-1} of $\sqrt{s} = 13 \text{ TeV}$ proton-
 671 proton collision data collected by the ATLAS detector at the LHC. The expected cross-section
 672 of WZ+b with 1-jet is $1.74^{+0.82}_{-0.75}(\text{stat})^{+0.53}_{-0.48}(\text{sys}) \text{ fb}$, and $14.6 \pm 2.5(\text{stat}) \pm 2.3(\text{sys}) \text{ fb}$ for WZ
 673 + charm, with a correlation of -0.22 between them. An expected significance of 2.0 is observed
 674 for WZ + b in this region.

675 For the 2-jet regions, an expected significance of 1.7 is observed for WZ + b, with an ex-
 676 pected cross-section of $2.5^{+1.3}_{-1.3}(\text{stat})^{+0.95}_{-0.83}(\text{sys}) \text{ fb}$. For WZ + charm, a cross-section of
 677 $12.7 \pm 3.2(\text{stat}) \pm 2.7(\text{sys}) \text{ fb}$ is expected for 2-jet events. A correlation of -0.26 is observed
 678 for WZ+b and WZ + charm.

679 **This section will be include final results once unblinded.**

680 References

- 681 [1] ATLAS Collaboration. ‘Observation of electroweak $W^\pm Z$ boson pair production in asso-
 682 ciation with two jets in pp collisions at $\sqrt{s} = 13 \text{ TeV}$ with the ATLAS detector’. In: *Phys.*
 683 *Lett.* B793 (2019), pp. 469–492. doi: [10.1016/j.physletb.2019.05.012](https://doi.org/10.1016/j.physletb.2019.05.012). arXiv:
 684 [1812.09740 \[hep-ex\]](https://arxiv.org/abs/1812.09740).
- 685 [2] ATLAS Collaboration. ‘Luminosity determination in pp collisions at $\sqrt{s} = 7 \text{ TeV}$ using
 686 the ATLAS detector at the LHC’. In: *Eur. Phys. J. C* 71 (2011), p. 1630. doi: [10.1140/epjc/s10052-011-1630-5](https://doi.org/10.1140/epjc/s10052-011-1630-5). arXiv: [1101.2185 \[hep-ex\]](https://arxiv.org/abs/1101.2185).
- 688 [3] ATLAS Collaboration. ‘Performance of the ATLAS detector using first collision data’. In:
 689 *JHEP* 09 (2010), p. 056. doi: [10.1007/JHEP09\(2010\)056](https://doi.org/10.1007/JHEP09(2010)056). arXiv: [1005.5254 \[hep-ex\]](https://arxiv.org/abs/1005.5254).
- 691 [4] S. Agostinelli et al. ‘GEANT4: A Simulation toolkit’. In: *Nucl. Instrum. Meth.* A506
 692 (2003), pp. 250–303. doi: [10.1016/S0168-9002\(03\)01368-8](https://doi.org/10.1016/S0168-9002(03)01368-8).
- 693 [5] T. Gleisberg et al. ‘Event generation with SHERPA 1.1’. In: *JHEP* 02 (2009), p. 007. doi:
 694 [10.1088/1126-6708/2009/02/007](https://doi.org/10.1088/1126-6708/2009/02/007). arXiv: [0811.4622 \[hep-ph\]](https://arxiv.org/abs/0811.4622).
- 695 [6] H.-L. Lai et al. ‘New parton distributions for collider physics’. In: *Phys. Rev. D* 82 (2010),
 696 p. 074024. doi: [10.1103/PhysRevD.82.074024](https://doi.org/10.1103/PhysRevD.82.074024). arXiv: [1007.2241 \[hep-ph\]](https://arxiv.org/abs/1007.2241).
- 697 [7] J. Alwall et al. ‘The automated computation of tree-level and next-to-leading order dif-
 698 fferential cross sections, and their matching to parton shower simulations’. In: *JHEP* 07
 699 (2014), p. 079. doi: [10.1007/JHEP07\(2014\)079](https://doi.org/10.1007/JHEP07(2014)079). arXiv: [1405.0301 \[hep-ph\]](https://arxiv.org/abs/1405.0301).
- 700 [8] R. D. Ball et al. ‘Parton distributions for the LHC Run II’. In: *JHEP* 04 (2015), p. 040.
 701 doi: [10.1007/JHEP04\(2015\)040](https://doi.org/10.1007/JHEP04(2015)040). arXiv: [1410.8849 \[hep-ph\]](https://arxiv.org/abs/1410.8849).
- 702 [9] M. Bahr et al. ‘Herwig++ Physics and Manual’. In: *Eur. Phys. J. C* 58 (2008), p. 639. doi:
 703 [10.1140/epjc/s10052-008-0798-9](https://doi.org/10.1140/epjc/s10052-008-0798-9). arXiv: [0803.0883 \[hep-ph\]](https://arxiv.org/abs/0803.0883).

- 704 [10] R. D. Ball et al. ‘Parton distributions with LHC data’. In: *Nucl. Phys. B* 867 (2013), p. 244.
 705 doi: [10.1016/j.nuclphysb.2012.10.003](https://doi.org/10.1016/j.nuclphysb.2012.10.003). arXiv: [1207.1303 \[hep-ph\]](https://arxiv.org/abs/1207.1303).
- 706 [11] S. Frixione, G. Ridolfi and P. Nason. ‘A positive-weight next-to-leading-order Monte Carlo
 707 for heavy flavour hadroproduction’. In: *JHEP* 09 (2007), p. 126. doi: [10.1088/1126-6708/2007/09/126](https://doi.org/10.1088/1126-6708/2007/09/126). arXiv: [0707.3088 \[hep-ph\]](https://arxiv.org/abs/0707.3088).
- 709 [12] E. Re. ‘Single-top Wt-channel production matched with parton showers using the POWHEG
 710 method’. In: *Eur. Phys. J. C* 71 (2011), p. 1547. doi: [10.1140/epjc/s10052-011-1547-z](https://doi.org/10.1140/epjc/s10052-011-1547-z). arXiv: [1009.2450 \[hep-ph\]](https://arxiv.org/abs/1009.2450).
- 712 [13] ATLAS Collaboration. *Electron efficiency measurements with the ATLAS detector using
 713 the 2015 LHC proton–proton collision data*. ATLAS-CONF-2016-024. 2016. URL: <https://cds.cern.ch/record/2157687>.
- 715 [14] ATLAS Collaboration. ‘Measurement of the muon reconstruction performance of the
 716 ATLAS detector using 2011 and 2012 LHC proton–proton collision data’. In: *Eur. Phys.
 717 J. C* 74 (2014), p. 3130. doi: [10.1140/epjc/s10052-014-3130-x](https://doi.org/10.1140/epjc/s10052-014-3130-x). arXiv: [1407.3935 \[hep-ex\]](https://arxiv.org/abs/1407.3935).
- 719 [15] R. Narayan et al. *Measurement of the total and differential cross sections of a top-quark-
 720 antiquark pair in association with a W boson in proton-proton collisions at a centre-of-
 721 mass energy of 13 TeV with ATLAS detector at the Large Hadron Collider*. Tech. rep.
 722 ATL-COM-PHYS-2020-217. Geneva: CERN, Mar. 2020. URL: <https://cds.cern.ch/record/2712986>.
- 724 [16] ATLAS Collaboration. *Jet Calibration and Systematic Uncertainties for Jets Reconstruc-
 725 ted in the ATLAS Detector at $\sqrt{s} = 13$ TeV*. ATL-PHYS-PUB-2015-015. 2015. URL:
 726 <https://cds.cern.ch/record/2037613>.
- 727 [17] ATLAS Collaboration. *Selection of jets produced in 13 TeV proton–proton collisions with
 728 the ATLAS detector*. ATLAS-CONF-2015-029. 2015. URL: <https://cds.cern.ch/record/2037702>.
- 730 [18] ATLAS Collaboration. ‘Performance of pile-up mitigation techniques for jets in pp col-
 731 lisions at $\sqrt{s} = 8$ TeV using the ATLAS detector’. In: *Eur. Phys. J. C* 76 (2016), p. 581.
 732 doi: [10.1140/epjc/s10052-016-4395-z](https://doi.org/10.1140/epjc/s10052-016-4395-z). arXiv: [1510.03823 \[hep-ex\]](https://arxiv.org/abs/1510.03823).
- 733 [19] ATLAS Collaboration. ‘Performance of b -jet identification in the ATLAS experiment’.
 734 In: *Journal of Instrumentation* 11.04 (2016), P04008. URL: <http://stacks.iop.org/1748-0221/11/i=04/a=P04008>.
- 736 [20] ATLAS Collaboration. ‘Performance of missing transverse momentum reconstruction
 737 with the ATLAS detector using proton–proton collisions at $\sqrt{s} = 13$ TeV’. In: *The
 738 European Physical Journal C* 78.11 (Nov. 2018). ISSN: 1434-6052. doi: [10.1140/epjc/s10052-018-6288-9](https://doi.org/10.1140/epjc/s10052-018-6288-9). URL: <http://dx.doi.org/10.1140/epjc/s10052-018-6288-9>.
- 741 [21] ATLAS Collaboration. ‘Measurement of the fiducial and differential cross-section of a top
 742 quark pair in association with a Z boson at 13 TeV with the ATLAS detector’. In: ATL-
 743 COM-PHYS-2019-334 (Apr. 2019). URL: <https://cds.cern.ch/record/2672207>.

- 744 [22] T. Chen and C. Guestrin. ‘XGBoost: A Scalable Tree Boosting System’. In: *Proceedings*
 745 of the 22nd ACM SIGKDD International Conference on Knowledge Discovery and Data
 746 Mining. KDD ’16. San Francisco, California, USA: ACM, 2016, pp. 785–794. ISBN: 978-
 747 1-4503-4232-2. doi: [10.1145/2939672.2939785](https://doi.org/10.1145/2939672.2939785). URL: <http://doi.acm.org/10.1145/2939672.2939785>.
- 749 [23] R. Frederix et al. ‘The automation of next-to-leading order electroweak calculations’. In:
 750 *Journal of High Energy Physics* 2018.7 (July 2018). ISSN: 1029-8479. doi: [10.1007/jhep07\(2018\)185](https://doi.org/10.1007/jhep07(2018)185). URL: [http://dx.doi.org/10.1007/JHEP07\(2018\)185](http://dx.doi.org/10.1007/JHEP07(2018)185).
- 752 [24] 2021. URL: https://twiki.cern.ch/twiki/bin/view/AtlasProtected/BTagCalibrationRecommendationsRelease21#Tools_for_Flavor_Tagging_Calibra.
- 755 [25] ‘Luminosity determination in pp collisions at $\sqrt{s} = 13$ TeV using the ATLAS detector at
 756 the LHC’. In: (June 2019).
- 757 [26] ATLAS Collaboration. ‘The new LUCID-2 detector for luminosity measurement and
 758 monitoring in ATLAS’. In: *JINST* 13.07 (2018), P07017. doi: [10.1088/1748-0221/13/07/P07017](https://doi.org/10.1088/1748-0221/13/07/P07017).
- 760 [27] A. Collaboration. ‘Electron reconstruction and identification in the ATLAS experiment
 761 using the 2015 and 2016 LHC proton–proton collision data at $\sqrt{s} = 13$ TeV’. In: *The*
 762 *European Physical Journal C* 79.8 (Aug. 2019). ISSN: 1434-6052. doi: [10.1140/epjc/s10052-019-7140-6](https://doi.org/10.1140/epjc/s10052-019-7140-6). URL: <http://dx.doi.org/10.1140/epjc/s10052-019-7140-6>.
- 765 [28] ATLAS Collaboration. ‘Jet energy scale measurements and their systematic uncertainties
 766 in proton–proton collisions at $\sqrt{s} = 13$ TeV with the ATLAS detector’. In: *Phys. Rev.*
 767 *D* 96 (2017), p. 072002. doi: [10.1103/PhysRevD.96.072002](https://doi.org/10.1103/PhysRevD.96.072002). arXiv: [1703.09665](https://arxiv.org/abs/1703.09665) [hep-ex].
- 769 [29] ATLAS Collaboration. ‘Observation of the associated production of a top quark and a
 770 Z boson in pp collisions at $\sqrt{s}= 13$ TeV with the ATLAS detector’. In: *Journal of High*
 771 *Energy Physics* 2020.7 (July 2020). ISSN: 1029-8479. doi: [10.1007/jhep07\(2020\)124](https://doi.org/10.1007/jhep07(2020)124).
 772 URL: [http://dx.doi.org/10.1007/JHEP07\(2020\)124](http://dx.doi.org/10.1007/JHEP07(2020)124).

773 **A Appendices**

774 **A.1 Non-prompt lepton MVA**

775 A lepton MVA has been developed to better reject non-prompt leptons than standard cut
 776 based selections based upon impact parameter, isolation and PID. The name of this MVA is
 777 **PromptLeptonVeto**. The full set of studies and detailed explanation can be found in [15].

778 The decays of W and Z bosons are commonly selected by the identification of one or two electrons
 779 or muons. The negligible lifetimes of these bosons mean that the leptons produced in the decay
 780 originate from the interaction vertex and are thus labelled “prompt”. Analyses using these
 781 light leptons impose strict reconstruction quality, isolation and impact parameter requirements
 782 to remove “fake” leptons. A significant source of the fake light leptons are non-prompt leptons
 783 produced in decays of hadrons that contain bottom (b) or charm (c) quarks. Such hadrons
 784 typically have microscopically significant lifetimes that can be detected experimentally.

785 These non-prompt leptons can also pass the tight selection criteria. In analyses that involve top (t)
 786 quarks, which decay almost exclusively into a W boson and a b quark, non-prompt leptons from
 787 the semileptonic decay of bottom and charm hadrons can be a significant source of background
 788 events. This is particularly the case in the selection of same-sign dilepton and multilepton final
 789 states.

790 The main idea is to identify non-prompt light leptons using lifetime information associated with a
 791 track jet that matches the selected light lepton. This lifetime information is computed using tracks
 792 contained within the jet. Typically, lepton lifetime is determined using the impact parameter of the
 793 track reconstructed by the inner tracking detector which is matched to the reconstructed lepton.
 794 Using additional reconstructed charged particle tracks increases the precision of identifying the
 795 displaced decay vertex of bottom or charm hadrons that produced a non-prompt light lepton.
 796 The MVA also includes information related to the isolation of the lepton to reject non-prompt
 797 leptons.

798 **PromptLeptonVeto** is a gradient boosted BDT. The training of the BDT is performed on leptons
 799 selected from the POWHEG+PYTHIA6 non-allhad $t\bar{t}$ MC sample. Eight variables are used to train
 800 the BDT in order to discriminate between prompt and non-prompt leptons. The track jets that
 801 are matched to the non-prompt leptons correspond to jets initiated by b or c quarks, and may
 802 contain a displaced vertex. Consequently, three of the selected variables are used to identify
 803 b-tag jets by standard ATLAS flavour tagging algorithms. Two variables use the relationship
 804 between the track jet and lepton: the ratio of the lepton p_T with respect to the track jet p_T and
 805 ΔR between the lepton and the track jet axis. Finally three additional variables test whether the
 806 reconstructed lepton is isolated: the number of tracks collected by the track jet and the lepton
 807 track and calorimeter isolation variables. Table 25 describes the variables used to train the BDT
 808 algorithm. The choice of input variables has been extensively discussed with Egamma, Muon,
 809 Tracking, and Flavour Tagging CP groups.

810 The output distribution of the BDT is shown in Figure A.1.

Variable	Description
N_{track} in track jet	Number of tracks collected by the track jet
$\text{IP2 log}(P_b/P_{\text{light}})$	Log-likelihood ratio between the b and light jet hypotheses with the IP2D algorithm
$\text{IP3 log}(P_b/P_{\text{light}})$	Log-likelihood ratio between the b and light jet hypotheses with the IP3D algorithm
N_{TrkAtVtx} SV + JF	Number of tracks used in the secondary vertex found by the SV1 algorithm in addition to the number of tracks from secondary vertices found by the JetFitter algorithm with at least two tracks
$p_T^{\text{lepton}}/p_T^{\text{track jet}}$	The ratio of the lepton p_T and the track jet p_T
$\Delta R(\text{lepton}, \text{track jet})$	ΔR between the lepton and the track jet axis
$p_T^{\text{VarCone30}}/p_T$	Lepton track isolation, with track collecting radius of $\Delta R < 0.3$
$E_T^{\text{TopoCone30}}/p_T$	Lepton calorimeter isolation, with topological cluster collecting radius of $\Delta R < 0.3$

Table 25: A table of the variables used in the training of `PromptLeptonVeto`.

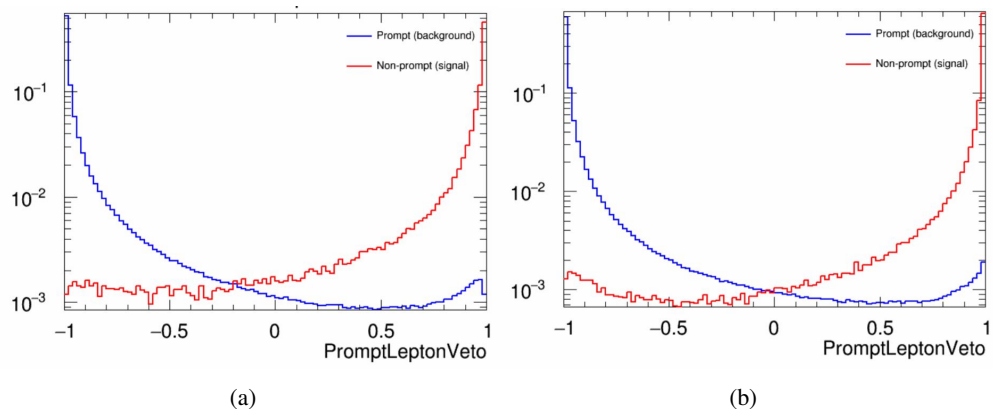


Figure 40: Distribution of the PLV BDT discriminant for (a) electrons and (b) muons.

811 The ROC curve for the BDT response, compared to the standard `FixedCutTight` WP, is shown
812 in figure A.1, which shows a clear improvement when using this alternative training.

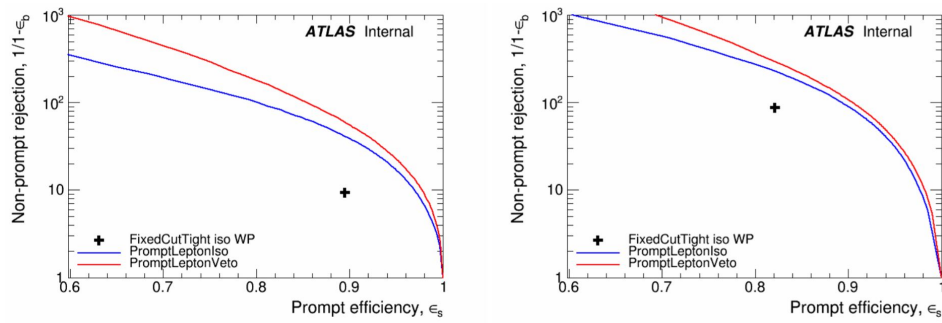


Figure 41: ROC curves for the PLV as well as the performance of the standard FixedCutTight WP for (left) electrons and (right) muons. Plot also includes curves for PROMPTLEPTONIso, which is not considered in this analysis.

813 A cutoff value of -0.7 for electrons and -0.5 for muons are chosen as the WPs for this MVA, based
814 on an optimisation of S/\sqrt{B} performed in the preselection regions of the $t\bar{t}H$ – ML analysis,
815 which have a signature similar to that of this analysis.

816 The efficiency of the tight `PromptLeptonVeto` working point is measured using the tag and
817 probe method with $Z \rightarrow \ell^+\ell^-$ events. Such calibration are performed by analysers from this
818 analysis in communication with the Egamma and Muon combined performance groups. The
819 scale factor are approximately 0.92 for $10 < p_T < 15$ GeV, and averaging at 0.98 to 0.99 for
820 higher p_T leptons. An extra systematic is applied to muons within $\Delta R < 0.6$ of a calorimeter
821 jet, since there is a strong dependence on the scale factor due to the presence of these jets. For
822 electrons, the dominant systematics is coming from pile-up dependence. Overall the systematics
823 are a maximum of 3% at low p_T and decreasing at a function of p_T .

824 **A.2 Non-prompt CR Modelling**

825 In order to further validate the modeling in each of the non-prompt CRs, additional kinematic
826 plots are made in the Z+jets CR and $t\bar{t}$ CR in each of the continuous b-tag regions, after the
827 correction factors detailed in Section 6.3 have been applied.

828 In the case of the Z+jets CR, the p_T spectrum of the lepton originating from the W candidate is
829 shown, as this is the distribution used to extract the scale factor applied to Z+jets. These plots
830 are shown in Figures 42 and 43.

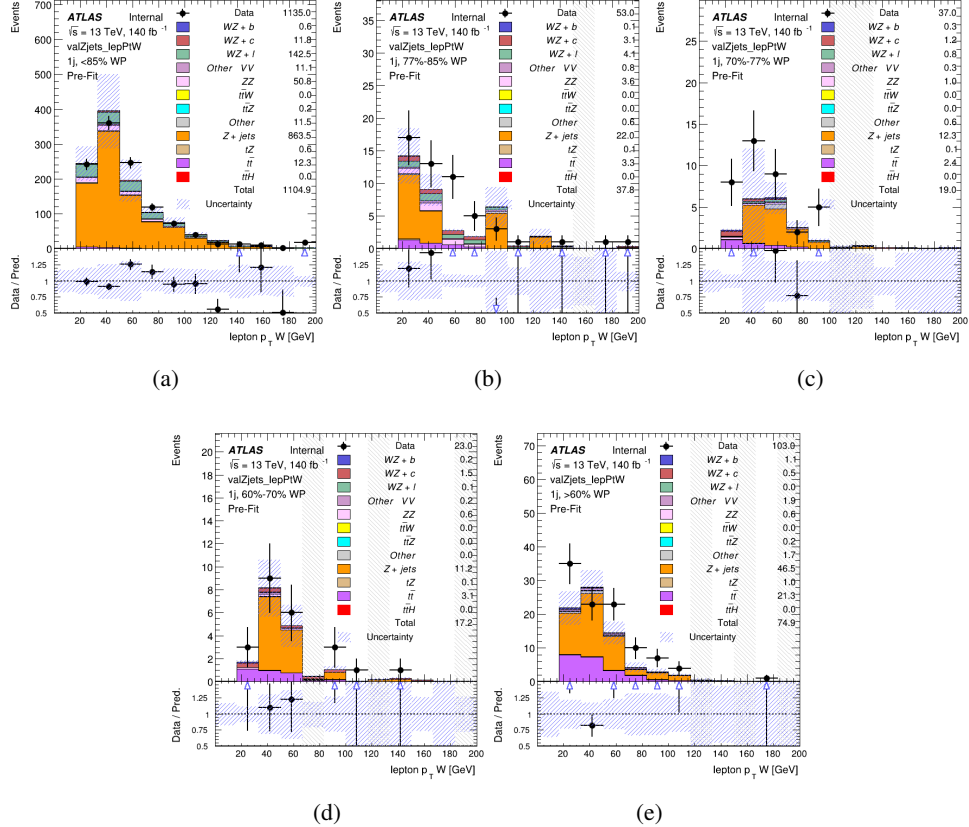


Figure 42: Comparisons between the data and MC distributions of the p_T of the lepton originating from the W-candidate in the Z+jets CR for each of the 1-jet b-tag working point regions

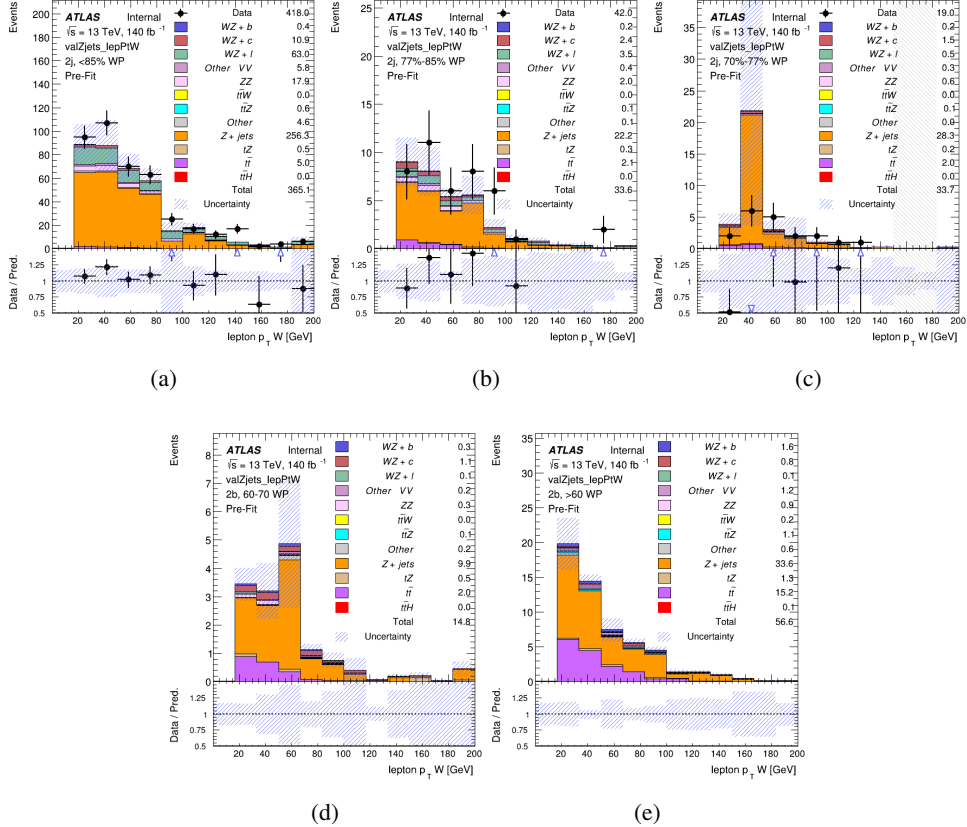


Figure 43: Comparisons between the data and MC distributions of the p_T of the lepton originating from the W-candidate in the Z+jets CR for each of the 2-jet b-tag working point regions

831 The same is shown for the $t\bar{t}$ CR, but the p_T of the OS lepton is used instead as a representation
 832 of the modeling, as the lepton from the W is not well defined for $t\bar{t}$ events. These plots are shown
 833 in Figures 44 and 45.

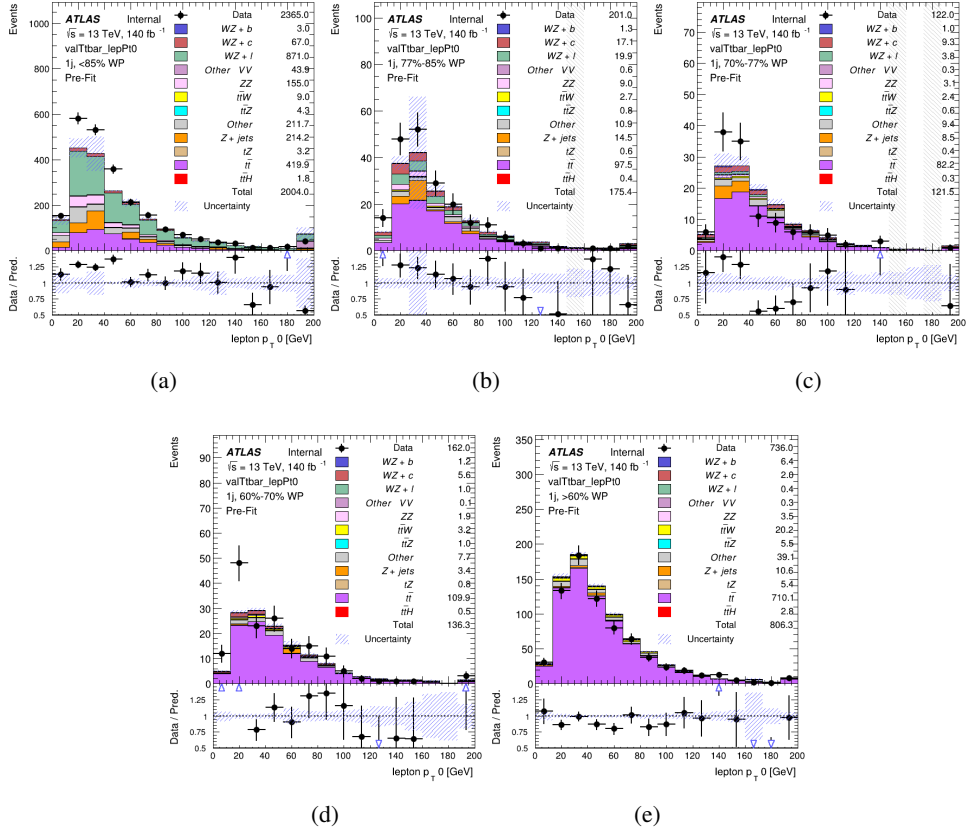


Figure 44: Comparisons between the data and MC distributions of the p_T of the OS lepton in the $t\bar{t}$ CR for each of the 1-jet b-tag working point regions

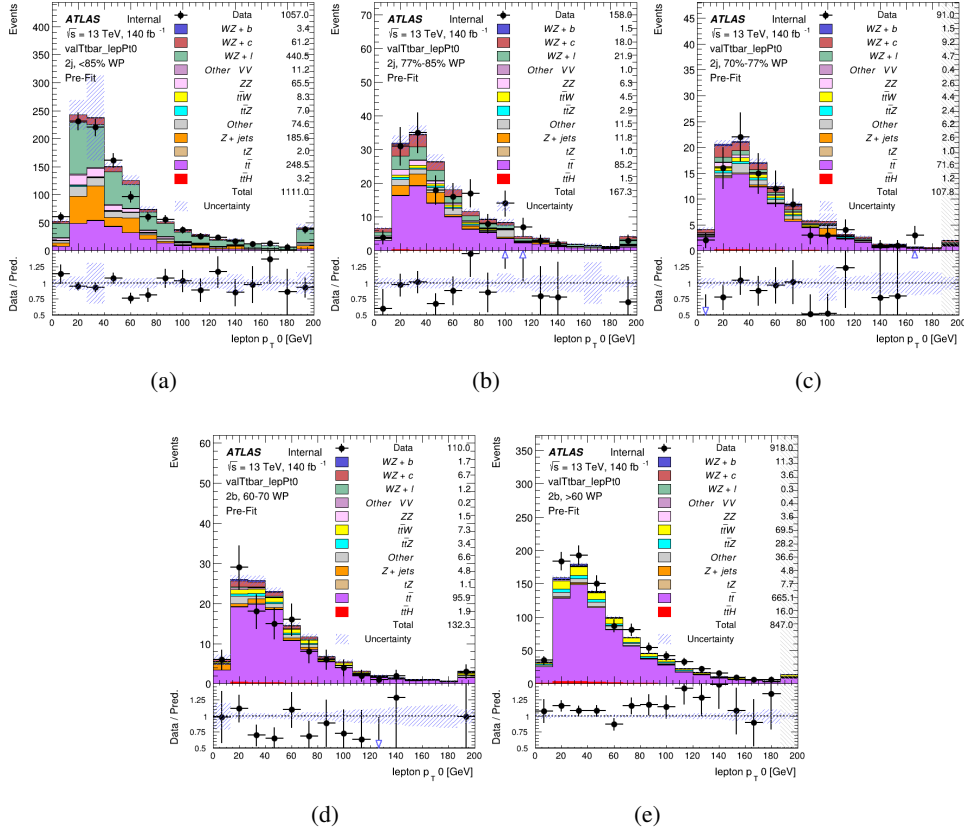


Figure 45: Comparisons between the data and MC distributions of the p_T of the OS lepton in the $t\bar{t}$ CR for each of the 2-jet b-tag working point regions

834 A.3 DSID list

Data:

```
data15_13TeV.AllYear.physics_Main.PhysCont.DAOD_HIGG8D1.grp15_v01_p4134
data16_13TeV.AllYear.physics_Main.PhysCont.DAOD_HIGG8D1.grp16_v01_p4134
data17_13TeV.AllYear.physics_Main.PhysCont.DAOD_HIGG8D1.grp17_v01_p4134
data18_13TeV.AllYear.physics_Main.PhysCont.DAOD_HIGG8D1.grp18_v01_p4134
```

mc16a:

```
mc16_13TeV.361603.PowhegPy8EG_CT10nloME_AZNLOCTEQ6L1_ZZllll_mll4.deriv.DAOD_HIGG8D1.e4475_s3126_r9364_r9315_p4133
mc16_13TeV.361602.PowhegPy8EG_CT10nloME_AZNLOCTEQ6L1_WZlvvv_mll4.deriv.DAOD_HIGG8D1.e4054_s3126_r9364_r9315_p4133
mc16_13TeV.361604.PowhegPy8EG_CT10nloME_AZNLOCTEQ6L1_ZZvvll_mll4.deriv.DAOD_HIGG8D1.e4475_s3126_r9364_r9315_p4133
mc16_13TeV.361600.PowhegPy8EG_CT10nloME_AZNLOCTEQ6L1_WWlvvv.deriv.DAOD_HIGG8D1.e4616_s3126_r9364_r9315_p4133
mc16_13TeV.361605.PowhegPy8EG_CT10nloME_AZNLOCTEQ6L1_ZZvvvv_mll4.deriv.DAOD_HIGG8D1.e4054_s3126_s3136_r9364_r9315_p4133
mc16_13TeV.361601.PowhegPy8EG_CT10nloME_AZNLOCTEQ6L1_WZlvvll_mll4.deriv.DAOD_HIGG8D1.e4475_s3126_r9364_r9315_p4133
mc16_13TeV.364286.Sherpa_222_NNPDF30NNLO_llvvjj_ss_EW4.deriv.DAOD_HIGG8D1.e6055_e5984_s3126_r9364_r9315_p3983 mc16_13TeV.364285.Sherpa_222_NNPDF30NNLO_llvvjj_ss_EW4.deriv.DAOD_HIGG8D1.e6055_e5984_s3126_r9364_r9315_p3983
mc16_13TeV.364740.MGPy8EG_NNPDF30NLO_A14NNPDF23LO_llvlij_EW6_OFPlus.deriv.DAOD_HIGG8D1.e7421_e5984_s3126_r9364_r9315_p4133
mc16_13TeV.364742.MGPy8EG_NNPDF30NLO_A14NNPDF23LO_llvlij_EW6_SFPlus.deriv.DAOD_HIGG8D1.e7421_e5984_s3126_r9364_r9315_p4133
mc16_13TeV.364253.Sherpa_222_NNPDF30NNLO_llvv.deriv.DAOD_HIGG8D1.e5916_s3126_r9364_r9315_p4133
mc16_13TeV.364250.Sherpa_222_NNPDF30NNLO_llll.deriv.DAOD_HIGG8D1.e5894_s3126_r9364_r9315_p4133
mc16_13TeV.364254.Sherpa_222_NNPDF30NNLO_llvv.deriv.DAOD_HIGG8D1.e5916_s3126_r9364_r9315_p4133
```

mc16_13TeV.364255.Sherpa_222_NNPDF30NNLO_lvyy.deriv.DAOD_HIGG8D1.e5916_s3126_r9364_r9315_p4133
 mc16_13TeV.410155.aMcAtNloPythia8EvtGen_MEN30NLO_A14N23LO_ttW.deriv.DAOD_HIGG8D1.e5070_s3126_r9364_r9315_p4133
 mc16_13TeV.410156.aMcAtNloPythia8EvtGen_MEN30NLO_A14N23LO_ttZnuu.deriv.DAOD_HIGG8D1.e5070_s3126_r9364_r9315_p4133
 mc16_13TeV.410157.aMcAtNloPythia8EvtGen_MEN30NLO_A14N23LO_ttZqq.deriv.DAOD_HIGG8D1.e5070_s3126_r9364_r9315_p4133
 mc16_13TeV.410218.aMcAtNloPythia8EvtGen_MEN30NLO_A14N23LO_ttee.deriv.DAOD_HIGG8D1.e5070_s3126_r9364_r9315_p4133
 mc16_13TeV.410219.aMcAtNloPythia8EvtGen_MEN30NLO_A14N23LO_ttmumu.deriv.DAOD_HIGG8D1.e5070_s3126_r9364_r9315_p4133
 mc16_13TeV.410220.aMcAtNloPythia8EvtGen_MEN30NLO_A14N23LO_ttautau.deriv.DAOD_HIGG8D1.e5070_s3126_r9364_r9315_p4133
 mc16_13TeV.412063.aMcAtNloPythia8EvtGen_tllq_NNPDF30_nf4_A4.deriv.DAOD_TOPQ1.e7054_e5984_s3126_r9364_r9315_p4174
 mc16_13TeV.410276.aMcAtNloPythia8EvtGen_MEN30NLO_A14N23LO_ttee_mll_1_5.deriv.DAOD_HIGG8D1.e6087_e5984_s3126_r9364_r9315_p4133
 mc16_13TeV.410277.aMcAtNloPythia8EvtGen_MEN30NLO_A14N23LO_ttmumu_mll_1_5.deriv.DAOD_HIGG8D1.e6087_e5984_s3126_r9364_r9315_p4133
 mc16_13TeV.410278.aMcAtNloPythia8EvtGen_MEN30NLO_A14N23LO_ttautau_mll_1_5.deriv.DAOD_HIGG8D1.e6087_e5984_s3126_r9364_r9315_p4133
 mc16_13TeV.410397.MadGraphPythia8EvtGen_ttbar_wbee_MEN30LO_A14N23LO.deriv.DAOD_HIGG8D1.e6086_e5984_s3126_r9364_r9315_p4133
 mc16_13TeV.410398.MadGraphPythia8EvtGen_ttbar_wbmumu_MEN30LO_A14N23LO.deriv.DAOD_HIGG8D1.e6086_e5984_s3126_r9364_r9315_p4133
 mc16_13TeV.410399.MadGraphPythia8EvtGen_ttbar_wbtautau_MEN30LO_A14N23LO.deriv.DAOD_HIGG8D1.e6086_e5984_s3126_r9364_r9315_p4133
 mc16_13TeV.410658.PhPy8EG_A14_tchan_BW50_lept_top.deriv.DAOD_HIGG8D1.e6671_e5984_s3126_r9364_r9315_p4133
 mc16_13TeV.410659.PhPy8EG_A14_tchan_BW50_lept_antitop.deriv.DAOD_HIGG8D1.e6671_e5984_s3126_r9364_r9315_p4133
 mc16_13TeV.410644.PowhegPythia8EvtGen_A14_singletop_schan_lept_top.deriv.DAOD_HIGG8D1.e6527_e5984_s3126_r9364_r9315_p4133
 mc16_13TeV.410645.PowhegPythia8EvtGen_A14_singletop_schan_lept_antitop.deriv.DAOD_HIGG8D1.e6527_e5984_s3126_r9364_r9315_p4133
 mc16_13TeV.304014.MadGraphPythia8EvtGen_A14NNPDF23_3top_SM.deriv.DAOD_HIGG8D1.e4324_s3126_r9364_r9315_p4133
 mc16_13TeV.410080.MadGraphPythia8EvtGen_A14NNPDF23_4topSM.deriv.DAOD_HIGG8D1.e4111_s3126_r9364_r9315_p4133
 mc16_13TeV.410081.MadGraphPythia8EvtGen_A14NNPDF23_ttbarWW.deriv.DAOD_HIGG8D1.e4111_s3126_r9364_r9315_p4133
 mc16_13TeV.364100.Sherpa_221_NNPDF30NNLO_Zmumu_MAXHTPTV0_70_CVetoBVeto.deriv.DAOD_HIGG8D1.e5271_s3126_r9364_r9315_p4133
 mc16_13TeV.364101.Sherpa_221_NNPDF30NNLO_Zmumu_MAXHTPTV0_70_CFilterBVeto.deriv.DAOD_HIGG8D1.e5271_s3126_r9364_r9315_p4133
 mc16_13TeV.364102.Sherpa_221_NNPDF30NNLO_Zmumu_MAXHTPTV0_70_BFilter.deriv.DAOD_HIGG8D1.e5271_s3126_r9364_r9315_p4133
 mc16_13TeV.364103.Sherpa_221_NNPDF30NNLO_Zmumu_MAXHTPTV70_140_CVetoBVeto.deriv.DAOD_HIGG8D1.e5271_s3126_r9364_r9315_p4133
 mc16_13TeV.364104.Sherpa_221_NNPDF30NNLO_Zmumu_MAXHTPTV70_140_CFilterBVeto.deriv.DAOD_HIGG8D1.e5271_s3126_r9364_r9315_p4133
 mc16_13TeV.364106.Sherpa_221_NNPDF30NNLO_Zmumu_MAXHTPTV140_280_CVetoBVeto.deriv.DAOD_HIGG8D1.e5271_s3126_r9364_r9315_p4133
 mc16_13TeV.364107.Sherpa_221_NNPDF30NNLO_Zmumu_MAXHTPTV140_280_CFilterBVeto.deriv.DAOD_HIGG8D1.e5271_s3126_r9364_r9315_p4133
 mc16_13TeV.364108.Sherpa_221_NNPDF30NNLO_Zmumu_MAXHTPTV140_280_BFilter.deriv.DAOD_HIGG8D1.e5271_s3126_r9364_r9315_p4133
 mc16_13TeV.364109.Sherpa_221_NNPDF30NNLO_Zmumu_MAXHTPTV280_500_CVetoBVeto.deriv.DAOD_HIGG8D1.e5271_s3126_r9364_r9315_p4133
 mc16_13TeV.364110.Sherpa_221_NNPDF30NNLO_Zmumu_MAXHTPTV280_500_CFilterBVeto.deriv.DAOD_HIGG8D1.e5271_s3126_r9364_r9315_p4133
 mc16_13TeV.364111.Sherpa_221_NNPDF30NNLO_Zmumu_MAXHTPTV280_500_BFilter.deriv.DAOD_HIGG8D1.e5271_e5984_s3126_r9364_r9315_p4133
 mc16_13TeV.364111.Sherpa_221_NNPDF30NNLO_Zmumu_MAXHTPTV280_500_BFilter.deriv.DAOD_HIGG8D1.e5271_s3126_r9364_r9315_p4133
 mc16_13TeV.364112.Sherpa_221_NNPDF30NNLO_Zmumu_MAXHTPTV500_1000.deriv.DAOD_HIGG8D1.e5271_s3126_r9364_r9315_p4133
 mc16_13TeV.364113.Sherpa_221_NNPDF30NNLO_Zmumu_MAXHTPTV1000_E_CMS.deriv.DAOD_HIGG8D1.e5271_s3126_r9364_r9315_p4133
 mc16_13TeV.364114.Sherpa_221_NNPDF30NNLO_Zee_MAXHTPTV0_70_CVetoBVeto.deriv.DAOD_HIGG8D1.e5299_s3126_r9364_r9315_p4133
 mc16_13TeV.364115.Sherpa_221_NNPDF30NNLO_Zee_MAXHTPTV0_70_CFilterBVeto.deriv.DAOD_HIGG8D1.e5299_s3126_r9364_r9315_p4133
 mc16_13TeV.364116.Sherpa_221_NNPDF30NNLO_Zee_MAXHTPTV0_70_BFilter.deriv.DAOD_HIGG8D1.e5299_s3126_r9364_r9315_p4133
 mc16_13TeV.364117.Sherpa_221_NNPDF30NNLO_Zee_MAXHTPTV70_140_CVetoBVeto.deriv.DAOD_HIGG8D1.e5299_s3126_r9364_r9315_p4133
 mc16_13TeV.364118.Sherpa_221_NNPDF30NNLO_Zee_MAXHTPTV70_140_CFilterBVeto.deriv.DAOD_HIGG8D1.e5299_s3126_r9364_r9315_p4133
 mc16_13TeV.364119.Sherpa_221_NNPDF30NNLO_Zee_MAXHTPTV70_140_BFilter.deriv.DAOD_HIGG8D1.e5299_s3126_r9364_r9315_p4133
 mc16_13TeV.364120.Sherpa_221_NNPDF30NNLO_Zee_MAXHTPTV140_280_CVetoBVeto.deriv.DAOD_HIGG8D1.e5299_s3126_r9364_r9315_p4133
 mc16_13TeV.364121.Sherpa_221_NNPDF30NNLO_Zee_MAXHTPTV140_280_CFilterBVeto.deriv.DAOD_HIGG8D1.e5299_s3126_r9364_r9315_p4133
 mc16_13TeV.364122.Sherpa_221_NNPDF30NNLO_Zee_MAXHTPTV140_280_BFilter.deriv.DAOD_HIGG8D1.e5299_s3126_r9364_r9315_p4133
 mc16_13TeV.364123.Sherpa_221_NNPDF30NNLO_Zee_MAXHTPTV280_500_CVetoBVeto.deriv.DAOD_HIGG8D1.e5299_s3126_r9364_r9315_p4133
 mc16_13TeV.364124.Sherpa_221_NNPDF30NNLO_Zee_MAXHTPTV280_500_CFilterBVeto.deriv.DAOD_HIGG8D1.e5299_s3126_r9364_r9315_p4133
 mc16_13TeV.364125.Sherpa_221_NNPDF30NNLO_Zee_MAXHTPTV280_500_BFilter.deriv.DAOD_HIGG8D1.e5299_s3126_r9364_r9315_p4133
 mc16_13TeV.364126.Sherpa_221_NNPDF30NNLO_Zee_MAXHTPTV280_500_BFilter.deriv.DAOD_HIGG8D1.e5299_s3126_r9364_r9315_p4133
 mc16_13TeV.364127.Sherpa_221_NNPDF30NNLO_Zee_MAXHTPTV1000_E_CMS.deriv.DAOD_HIGG8D1.e5299_s3126_r9364_r9315_p4133
 mc16_13TeV.364128.Sherpa_221_NNPDF30NNLO_Ztautau_MAXHTPTV0_70_CVetoBVeto.deriv.DAOD_HIGG8D1.e5307_s3126_r9364_r9315_p4133
 mc16_13TeV.364129.Sherpa_221_NNPDF30NNLO_Ztautau_MAXHTPTV0_70_CFilterBVeto.deriv.DAOD_HIGG8D1.e5307_s3126_r9364_r9315_p4133
 mc16_13TeV.364130.Sherpa_221_NNPDF30NNLO_Ztautau_MAXHTPTV0_70_BFilter.deriv.DAOD_HIGG8D1.e5307_s3126_r9364_r9315_p4133
 mc16_13TeV.364131.Sherpa_221_NNPDF30NNLO_Ztautau_MAXHTPTV70_140_CVetoBVeto.deriv.DAOD_HIGG8D1.e5307_s3126_r9364_r9315_p4133
 mc16_13TeV.364132.Sherpa_221_NNPDF30NNLO_Ztautau_MAXHTPTV70_140_CFilterBVeto.deriv.DAOD_HIGG8D1.e5307_s3126_r9364_r9315_p4133
 mc16_13TeV.364133.Sherpa_221_NNPDF30NNLO_Ztautau_MAXHTPTV70_140_BFilter.deriv.DAOD_HIGG8D1.e5307_s3126_r9364_r9315_p4133
 mc16_13TeV.364134.Sherpa_221_NNPDF30NNLO_Ztautau_MAXHTPTV140_280_CVetoBVeto.deriv.DAOD_HIGG8D1.e5307_s3126_r9364_r9315_p4133
 mc16_13TeV.364135.Sherpa_221_NNPDF30NNLO_Ztautau_MAXHTPTV140_280_CFilterBVeto.deriv.DAOD_HIGG8D1.e5307_s3126_r9364_r9315_p4133
 mc16_13TeV.364136.Sherpa_221_NNPDF30NNLO_Ztautau_MAXHTPTV140_280_BFilter.deriv.DAOD_HIGG8D1.e5307_s3126_r9364_r9315_p4133
 mc16_13TeV.364137.Sherpa_221_NNPDF30NNLO_Ztautau_MAXHTPTV280_500_CVetoBVeto.deriv.DAOD_HIGG8D1.e5307_e5984_s3126_r9364_r9315_p4133
 mc16_13TeV.364138.Sherpa_221_NNPDF30NNLO_Ztautau_MAXHTPTV280_500_CFilterBVeto.deriv.DAOD_HIGG8D1.e5313_s3126_r9364_r9315_p4133

mc16_13TeV.364189.Sherpa_221_NNPDF30NNLO_Wtaunu_MAXHTPTV70_140_BFilter.deriv.DAOD_HIGG8D1.e5340_s3126_r9364_r9315_p4133
 mc16_13TeV.364190.Sherpa_221_NNPDF30NNLO_Wtaunu_MAXHTPTV140_280_CVetoBVeto.deriv.DAOD_HIGG8D1.e5340_e5984_s3126_r9364_r9315_p4133
 mc16_13TeV.364191.Sherpa_221_NNPDF30NNLO_Wtaunu_MAXHTPTV140_280_CVetoBVeto.deriv.DAOD_HIGG8D1.e5340_s3126_r9364_r9315_p4133
 mc16_13TeV.364191.Sherpa_221_NNPDF30NNLO_Wtaunu_MAXHTPTV140_280_CFilterBVeto.deriv.DAOD_HIGG8D1.e5340_s3126_r9364_r9315_p4133
 mc16_13TeV.364191.Sherpa_221_NNPDF30NNLO_Wtaunu_MAXHTPTV140_280_CFilterBVeto.deriv.DAOD_HIGG8D1.e5340_e5984_s3126_s3136_r9364_r9315_p4133
 mc16_13TeV.364192.Sherpa_221_NNPDF30NNLO_Wtaunu_MAXHTPTV140_280_BFilter.deriv.DAOD_HIGG8D1.e5340_s3126_r9364_r9315_p4133
 mc16_13TeV.364193.Sherpa_221_NNPDF30NNLO_Wtaunu_MAXHTPTV280_500_CVetoBVeto.deriv.DAOD_HIGG8D1.e5340_s3126_r9364_r9315_p4133
 mc16_13TeV.364193.Sherpa_221_NNPDF30NNLO_Wtaunu_MAXHTPTV280_500_CVetoBVeto.deriv.DAOD_HIGG8D1.e5340_e5984_s3126_s3136_r9364_r9315_p4133
 mc16_13TeV.364194.Sherpa_221_NNPDF30NNLO_Wtaunu_MAXHTPTV280_500_CFilterBVeto.deriv.DAOD_HIGG8D1.e5340_s3126_r9364_r9315_p4133
 mc16_13TeV.364194.Sherpa_221_NNPDF30NNLO_Wtaunu_MAXHTPTV280_500_CFilterBVeto.deriv.DAOD_HIGG8D1.e5340_e5984_s3126_s3136_r9364_r9315_p4133
 mc16_13TeV.364195.Sherpa_221_NNPDF30NNLO_Wtaunu_MAXHTPTV280_500_BFilter.deriv.DAOD_HIGG8D1.e5340_s3126_r9364_r9315_p4133
 mc16_13TeV.364196.Sherpa_221_NNPDF30NNLO_Wtaunu_MAXHTPTV500_1000.deriv.DAOD_HIGG8D1.e5340_s3126_r9364_r9315_p4133
 mc16_13TeV.364197.Sherpa_221_NNPDF30NNLO_Wtaunu_MAXHTPTV1000_E_CMS.deriv.DAOD_HIGG8D1.e5340_s3126_r9364_r9315_p4133
 mc16_13TeV.364500.Sherpa_222_NNPDF30NNLO_eegamma_pty_7_15.deriv.DAOD_HIGG8D1.e5928_e5984_s3126_r9364_r9315_p4133
 mc16_13TeV.364501.Sherpa_222_NNPDF30NNLO_eegamma_pty_15_35.deriv.DAOD_HIGG8D1.e5928_e5984_s3126_r9364_r9315_p4133
 mc16_13TeV.364502.Sherpa_222_NNPDF30NNLO_eegamma_pty_35_70.deriv.DAOD_HIGG8D1.e5928_e5984_s3126_r9364_r9315_p4133
 mc16_13TeV.364503.Sherpa_222_NNPDF30NNLO_eegamma_pty_70_140.deriv.DAOD_HIGG8D1.e5928_e5984_s3126_r9364_r9315_p4133
 mc16_13TeV.364504.Sherpa_222_NNPDF30NNLO_eegamma_pty_140_E_CMS.deriv.DAOD_HIGG8D1.e5928_e5984_s3126_r9364_r9315_p4133
 mc16_13TeV.364505.Sherpa_222_NNPDF30NNLO_mumugamma_pty_7_15.deriv.DAOD_HIGG8D1.e5928_e5984_s3126_r9364_r9315_p4133
 mc16_13TeV.364506.Sherpa_222_NNPDF30NNLO_mumugamma_pty_15_35.deriv.DAOD_HIGG8D1.e5988_e5984_s3126_r9364_r9315_p4133
 mc16_13TeV.364507.Sherpa_222_NNPDF30NNLO_mumugamma_pty_35_70.deriv.DAOD_HIGG8D1.e5928_e5984_s3126_r9364_r9315_p4133
 mc16_13TeV.364508.Sherpa_222_NNPDF30NNLO_mumugamma_pty_70_140.deriv.DAOD_HIGG8D1.e5928_e5984_s3126_r9364_r9315_p4133
 mc16_13TeV.364509.Sherpa_222_NNPDF30NNLO_mumugamma_pty_140_E_CMS.deriv.DAOD_HIGG8D1.e5928_e5984_s3126_r9364_r9315_p4133
 mc16_13TeV.364510.Sherpa_222_NNPDF30NNLO_tautaugamma_pty_7_15.deriv.DAOD_HIGG8D1.e5928_s3126_r9364_r9315_p4133
 mc16_13TeV.364511.Sherpa_222_NNPDF30NNLO_tautaugamma_pty_15_35.deriv.DAOD_HIGG8D1.e5928_s3126_r9364_r9315_p4133
 mc16_13TeV.364512.Sherpa_222_NNPDF30NNLO_tautaugamma_pty_35_70.deriv.DAOD_HIGG8D1.e5928_s3126_r9364_r9315_p4133
 mc16_13TeV.364513.Sherpa_222_NNPDF30NNLO_tautaugamma_pty_70_140.deriv.DAOD_HIGG8D1.e5982_s3126_r9364_r9315_p4133
 mc16_13TeV.364514.Sherpa_222_NNPDF30NNLO_tautaugamma_pty_140_E_CMS.deriv.DAOD_HIGG8D1.e5928_s3126_r9364_r9315_p4133
 mc16_13TeV.364521.Sherpa_222_NNPDF30NNLO_enugamma_pty_7_15.deriv.DAOD_HIGG8D1.e5928_s3126_r9364_r9315_p4133
 mc16_13TeV.364522.Sherpa_222_NNPDF30NNLO_enugamma_pty_15_35.deriv.DAOD_HIGG8D1.e5928_s3126_r9364_r9315_p4133
 mc16_13TeV.364523.Sherpa_222_NNPDF30NNLO_enugamma_pty_35_70.deriv.DAOD_HIGG8D1.e5928_s3126_r9364_r9315_p4133
 mc16_13TeV.364524.Sherpa_222_NNPDF30NNLO_enugamma_pty_70_140.deriv.DAOD_HIGG8D1.e5928_s3126_r9364_r9315_p4133
 mc16_13TeV.364525.Sherpa_222_NNPDF30NNLO_enugamma_pty_140_E_CMS.deriv.DAOD_HIGG8D1.e5928_s3126_r9364_r9315_p4133
 mc16_13TeV.364525.Sherpa_222_NNPDF30NNLO_enugamma_pty_140_E_CMS.deriv.DAOD_HIGG8D1.e5928_e5984_s3126_r9364_r9315_p4133
 mc16_13TeV.364526.Sherpa_222_NNPDF30NNLO_munugamma_pty_7_15.deriv.DAOD_HIGG8D1.e5928_s3126_r9364_r9315_p4133
 mc16_13TeV.364527.Sherpa_222_NNPDF30NNLO_munugamma_pty_15_35.deriv.DAOD_HIGG8D1.e5928_s3126_r9364_r9315_p4133
 mc16_13TeV.364528.Sherpa_222_NNPDF30NNLO_munugamma_pty_35_70.deriv.DAOD_HIGG8D1.e5928_s3126_r9364_r9315_p4133
 mc16_13TeV.364529.Sherpa_222_NNPDF30NNLO_munugamma_pty_70_140.deriv.DAOD_HIGG8D1.e5928_s3126_r9364_r9315_p4133
 mc16_13TeV.364530.Sherpa_222_NNPDF30NNLO_munugamma_pty_140_E_CMS.deriv.DAOD_HIGG8D1.e5928_s3126_r9364_r9315_p4133
 mc16_13TeV.364530.Sherpa_222_NNPDF30NNLO_munugamma_pty_140_E_CMS.deriv.DAOD_HIGG8D1.e5928_e5984_s3126_r9364_r9315_p4133
 mc16_13TeV.364531.Sherpa_222_NNPDF30NNLO_taunugamma_pty_7_15.deriv.DAOD_HIGG8D1.e5928_s3126_r9364_r9315_p4133
 mc16_13TeV.364532.Sherpa_222_NNPDF30NNLO_taunugamma_pty_15_35.deriv.DAOD_HIGG8D1.e5928_s3126_r9364_r9315_p4133
 mc16_13TeV.364533.Sherpa_222_NNPDF30NNLO_taunugamma_pty_35_70.deriv.DAOD_HIGG8D1.e5928_s3126_r9364_r9315_p4133
 mc16_13TeV.364534.Sherpa_222_NNPDF30NNLO_taunugamma_pty_70_140.deriv.DAOD_HIGG8D1.e5928_s3126_r9364_r9315_p4133
 mc16_13TeV.364535.Sherpa_222_NNPDF30NNLO_taunugamma_pty_140_E_CMS.deriv.DAOD_HIGG8D1.e5928_s3126_r9364_r9315_p4133
 mc16_13TeV.364535.Sherpa_222_NNPDF30NNLO_taunugamma_pty_140_E_CMS.deriv.DAOD_HIGG8D1.e5928_e5984_s3126_r9364_r9315_p4133
 mc16_13TeV.410560.MadGraphPythia8EvtGen_A14_Z_4fl_tchan_noAllHad.deriv.DAOD_HIGG8D1.e5803_s3126_r9364_r9315_p4133
 mc16_13TeV.410013.PowhegPythiaEvtGen_P2012_Wt_inclusive_top.deriv.DAOD_HIGG8D1.e3753_s3126_r9364_r9315_p4133
 mc16_13TeV.410014.PowhegPythiaEvtGen_P2012_Wt_inclusive_antitop.deriv.DAOD_HIGG8D1.e3753_s3126_r9364_r9315_p4133
 mc16_13TeV.410408.aMcAtNloPythia8EvtGen_tWZ_Tzoll_minDR1.deriv.DAOD_HIGG8D1.e6423_e5984_s3126_r9364_r9315_p4133
 mc16_13TeV.364242.Sherpa_222_NNPDF30NNLO_WWW_31v_EW6.deriv.DAOD_HIGG8D1.e5887_s3126_r9364_r9315_p4133
 mc16_13TeV.364243.Sherpa_222_NNPDF30NNLO_WWW_412v_EW6.deriv.DAOD_HIGG8D1.e5887_s3126_r9364_r9315_p4133
 mc16_13TeV.364244.Sherpa_222_NNPDF30NNLO_WWW_214v_EW6.deriv.DAOD_HIGG8D1.e5887_s3126_r9364_r9315_p4133
 mc16_13TeV.364245.Sherpa_222_NNPDF30NNLO_WZZ_51v_EW6.deriv.DAOD_HIGG8D1.e5887_s3126_r9364_r9315_p4133
 mc16_13TeV.364246.Sherpa_222_NNPDF30NNLO_WZZ_313v_EW6.deriv.DAOD_HIGG8D1.e5887_s3126_r9364_r9315_p4133
 mc16_13TeV.364247.Sherpa_222_NNPDF30NNLO_ZZZ_610v_EW6.deriv.DAOD_HIGG8D1.e5887_s3126_r9364_r9315_p4133
 mc16_13TeV.364248.Sherpa_222_NNPDF30NNLO_ZZZ_412v_EW6.deriv.DAOD_HIGG8D1.e5887_s3126_r9364_r9315_p4133
 mc16_13TeV.364249.Sherpa_222_NNPDF30NNLO_ZZZ_214v_EW6.deriv.DAOD_HIGG8D1.e5887_s3126_r9364_r9315_p4133
 mc16_13TeV.342284.Pythia8EvtGen_A14NNPDF23LO_WH125_inc.deriv.DAOD_HIGG8D1.e4246_s3126_r9364_r9315_p4133
 mc16_13TeV.342285.Pythia8EvtGen_A14NNPDF23LO_ZH125_inc.deriv.DAOD_HIGG8D1.e4246_s3126_r9364_r9315_p4133
 mc16_13TeV.341998.aMcAtNloHppEG_UEEE5_CTEQ6L1_CT10ME_tWH125_gamgam_yt_plus1.deriv.DAOD_HIGG8D1.e4394_e5984_s3126_r9364_r9315_p4133
 mc16_13TeV.410389.MadGraphPythia8EvtGen_A14NNPDF23_ttgamma_nonallhadronic.deriv.DAOD_HIGG8D1.e6155_e5984_s3126_r9364_r9315_p4133

mc16_13TeV.410470.PhPy8EG_A14_ttbar_hdamp258p75_nonallhad.deriv.DAOD_HIGG8D1.e6337_e5984_s3126_r9364_r9315_p4133
 mc16_13TeV.410472.PhPy8EG_A14_ttbar_hdamp258p75_dil.deriv.DAOD_HIGG8D1.e6348_e5984_s3126_r9364_r9315_p4133
 mc16_13TeV.346343.PhPy8EG_A14NNPDF23_NNPDF30ME_ttH125_allhad.deriv.DAOD_HIGG8D1.e7148_e5984_s3126_r9364_r9315_p4133
 mc16_13TeV.346344.PhPy8EG_A14NNPDF23_NNPDF30ME_ttH125_semilep.deriv.DAOD_HIGG8D1.e7148_e5984_s3126_r9364_r9315_p4133
 mc16_13TeV.346345.PhPy8EG_A14NNPDF23_NNPDF30ME_ttH125_dilep.deriv.DAOD_HIGG8D1.e7148_e5984_s3126_r9364_r9315_p4133

 mc16d:
 mc16_13TeV.364253.Sherpa_222_NNPDF30NNLO_lllv.deriv.DAOD_HIGG8D1.e5916_e5984_s3126_r10201_r10210_p4133
 mc16_13TeV.364250.Sherpa_222_NNPDF30NNLO_llll.deriv.DAOD_HIGG8D1.e5984_e5984_s3126_r10201_r10210_p4133
 mc16_13TeV.364254.Sherpa_222_NNPDF30NNLO_llvv.deriv.DAOD_HIGG8D1.e5916_e5984_s3126_r10201_r10210_p4133
 mc16_13TeV.364255.Sherpa_222_NNPDF30NNLO_lvvv.deriv.DAOD_HIGG8D1.e5916_e5984_s3126_r10201_r10210_p4133
 mc16_13TeV.410155.aMcAtNloPythia8EvtGen_MEN30NLO_A14N23LO_ttW.deriv.DAOD_HIGG8D1.e5070_e5984_s3126_r10201_r10210_p4133
 mc16_13TeV.410156.aMcAtNloPythia8EvtGen_MEN30NLO_A14N23LO_ttZnunu.deriv.DAOD_HIGG8D1.e5070_e5984_s3126_r10201_r10210_p4133
 mc16_13TeV.410157.aMcAtNloPythia8EvtGen_MEN30NLO_A14N23LO_ttZqq.deriv.DAOD_HIGG8D1.e5070_e5984_s3126_r10201_r10210_p4133
 mc16_13TeV.410218.aMcAtNloPythia8EvtGen_MEN30NLO_A14N23LO_ttee.deriv.DAOD_HIGG8D1.e5070_e5984_s3126_r10201_r10210_p4133
 mc16_13TeV.410219.aMcAtNloPythia8EvtGen_MEN30NLO_A14N23LO_ttmumu.deriv.DAOD_HIGG8D1.e5070_e5984_s3126_r10201_r10210_p4133
 mc16_13TeV.410220.aMcAtNloPythia8EvtGen_MEN30NLO_A14N23LO_ttautau.deriv.DAOD_HIGG8D1.e5070_e5984_s3126_r10201_r10210_p4133
 mc16_13TeV.410276.aMcAtNloPythia8EvtGen_MEN30NLO_A14N23LO_ttautau_mll_1_5.deriv.DAOD_HIGG8D1.e6087_e5984_s3126_r10201_r10210_p4133
 mc16_13TeV.410277.aMcAtNloPythia8EvtGen_MEN30NLO_A14N23LO_ttautau_mll_1_5.deriv.DAOD_HIGG8D1.e6087_e5984_s3126_r10201_r10210_p4133
 mc16_13TeV.410278.aMcAtNloPythia8EvtGen_MEN30NLO_A14N23LO_ttautau_mll_1_5.deriv.DAOD_HIGG8D1.e6087_e5984_s3126_r10201_r10210_p4133
 mc16_13TeV.410397.MadGraphPythia8EvtGen_ttbar_wbee_MEN30LO_A14N23LO.deriv.DAOD_HIGG8D1.e6086_e5984_s3126_r10201_r10210_p4133
 mc16_13TeV.410398.MadGraphPythia8EvtGen_ttbar_wbmumu_MEN30LO_A14N23LO.deriv.DAOD_HIGG8D1.e6086_e5984_s3126_r10201_r10210_p4133
 mc16_13TeV.410399.MadGraphPythia8EvtGen_ttbar_wbtautau_MEN30LO_A14N23LO.deriv.DAOD_HIGG8D1.e6086_e5984_s3126_r10201_r10210_p4133
 mc16_13TeV.410658.PhPy8EG_A14_tchan_BW50_lept_top.deriv.DAOD_HIGG8D1.e6671_e5984_s3126_r10201_r10210_p4133
 mc16_13TeV.410659.PhPy8EG_A14_tchan_BW50_lept_antitop.deriv.DAOD_HIGG8D1.e6671_e5984_s3126_r10201_r10210_p4133
 mc16_13TeV.410644.PowhegPythia8EvtGen_A14_singleton_schan_lept_top.deriv.DAOD_HIGG8D1.e6527_e5984_s3126_r10201_r10210_p4133
 mc16_13TeV.410645.PowhegPythia8EvtGen_A14_singleton_schan_lept_antitop.deriv.DAOD_HIGG8D1.e6527_s3126_r10201_r10210_p4133
 mc16_13TeV.412063.aMcAtNloPythia8EvtGen_tllq_NNPDF30_nf4_A14.deriv.DAOD_TOPQ1.e7054_e5984_s3126_r10201_r10210_p4174
 mc16_13TeV.304014.MadGraphPythia8EvtGen_A14NNPDF23_3top_SM.deriv.DAOD_HIGG8D1.e4324_e5984_s3126_r10201_r10210_p4133
 mc16_13TeV.410080.MadGraphPythia8EvtGen_A14NNPDF23_4topSM.deriv.DAOD_HIGG8D1.e4111_e5984_s3126_r10201_r10210_p4133
 mc16_13TeV.410081.MadGraphPythia8EvtGen_A14NNPDF23_ttbarWW.deriv.DAOD_HIGG8D1.e4111_e5984_s3126_r10201_r10210_p4133
 mc16_13TeV.364100.Sherpa_221_NNPDF30NNLO_Zmumu_MAXHTPTV0_70_CVetoBVeto.deriv.DAOD_HIGG8D1.e5271_s3126_r10201_r10210_p4133
 mc16_13TeV.364101.Sherpa_221_NNPDF30NNLO_Zmumu_MAXHTPTV0_70_CFilterBVeto.deriv.DAOD_HIGG8D1.e5271_s3126_r10201_r10210_p4133
 mc16_13TeV.364101.Sherpa_221_NNPDF30NNLO_Zmumu_MAXHTPTV0_70_CFilterBVeto.deriv.DAOD_HIGG8D1.e5271_s3126_r10201_r10210_p4133
 mc16_13TeV.364102.Sherpa_221_NNPDF30NNLO_Zmumu_MAXHTPTV0_70_BFilter.deriv.DAOD_HIGG8D1.e5271_s3126_r10201_r10210_p4133
 mc16_13TeV.364103.Sherpa_221_NNPDF30NNLO_Zmumu_MAXHTPTV70_140_CVetoBVeto.deriv.DAOD_HIGG8D1.e5271_s3126_r10201_r10210_p4133
 mc16_13TeV.364104.Sherpa_221_NNPDF30NNLO_Zmumu_MAXHTPTV70_140_CFilterBVeto.deriv.DAOD_HIGG8D1.e5271_s3126_r10201_r10210_p4133
 mc16_13TeV.364106.Sherpa_221_NNPDF30NNLO_Zmumu_MAXHTPTV140_280_CVetoBVeto.deriv.DAOD_HIGG8D1.e5271_s3126_r10201_r10210_p4133
 mc16_13TeV.364107.Sherpa_221_NNPDF30NNLO_Zmumu_MAXHTPTV140_280_CFilterBVeto.deriv.DAOD_HIGG8D1.e5271_s3126_r10201_r10210_p4133
 mc16_13TeV.364108.Sherpa_221_NNPDF30NNLO_Zmumu_MAXHTPTV140_280_BFilter.deriv.DAOD_HIGG8D1.e5271_s3126_r10201_r10210_p4133
 mc16_13TeV.364108.Sherpa_221_NNPDF30NNLO_Zmumu_MAXHTPTV140_280_BFilter.deriv.DAOD_HIGG8D1.e5271_s3126_r10201_r10210_p4133
 mc16_13TeV.364109.Sherpa_221_NNPDF30NNLO_Zmumu_MAXHTPTV280_500_CVetoBVeto.deriv.DAOD_HIGG8D1.e5271_s3126_r10201_r10210_p4133
 mc16_13TeV.364109.Sherpa_221_NNPDF30NNLO_Zmumu_MAXHTPTV280_500_CVetoBVeto.deriv.DAOD_HIGG8D1.e5271_s3126_r10201_r10210_p4133
 mc16_13TeV.364110.Sherpa_221_NNPDF30NNLO_Zmumu_MAXHTPTV280_500_CFilterBVeto.deriv.DAOD_HIGG8D1.e5271_s3126_r10201_r10210_p4133
 mc16_13TeV.364111.Sherpa_221_NNPDF30NNLO_Zmumu_MAXHTPTV280_500_BFilter.deriv.DAOD_HIGG8D1.e5271_s3126_r10201_r10210_p4133
 mc16_13TeV.364112.Sherpa_221_NNPDF30NNLO_Zmumu_MAXHTPTV280_500_BFilter.deriv.DAOD_HIGG8D1.e5271_s3126_r10201_r10210_p4133
 mc16_13TeV.364112.Sherpa_221_NNPDF30NNLO_Zmumu_MAXHTPTV500_1000.deriv.DAOD_HIGG8D1.e5271_s3126_r10201_r10210_p4133
 mc16_13TeV.364113.Sherpa_221_NNPDF30NNLO_Zmumu_MAXHTPTV1000_E_CMS.deriv.DAOD_HIGG8D1.e5271_s3126_r10201_r10210_p4133
 mc16_13TeV.364114.Sherpa_221_NNPDF30NNLO_Zee_MAXHTPTV0_70_CVetoBVeto.deriv.DAOD_HIGG8D1.e5299_s3126_r10201_r10210_p4133
 mc16_13TeV.364115.Sherpa_221_NNPDF30NNLO_Zee_MAXHTPTV0_70_CFilterBVeto.deriv.DAOD_HIGG8D1.e5299_e5984_s3126_r10201_r10210_p4133
 mc16_13TeV.364116.Sherpa_221_NNPDF30NNLO_Zee_MAXHTPTV0_70_BFilter.deriv.DAOD_HIGG8D1.e5299_e5984_s3126_r10201_r10210_p4133
 mc16_13TeV.364117.Sherpa_221_NNPDF30NNLO_Zee_MAXHTPTV70_140_CVetoBVeto.deriv.DAOD_HIGG8D1.e5299_e5984_s3126_r10201_r10210_p4133
 mc16_13TeV.364118.Sherpa_221_NNPDF30NNLO_Zee_MAXHTPTV70_140_CFilterBVeto.deriv.DAOD_HIGG8D1.e5299_e5984_s3126_r10201_r10210_p4133
 mc16_13TeV.364119.Sherpa_221_NNPDF30NNLO_Zee_MAXHTPTV70_140_BFilter.deriv.DAOD_HIGG8D1.e5299_e5984_s3126_r10201_r10210_p4133
 mc16_13TeV.364120.Sherpa_221_NNPDF30NNLO_Zee_MAXHTPTV140_280_CVetoBVeto.deriv.DAOD_HIGG8D1.e5299_e5984_s3126_r10201_r10210_p4133
 mc16_13TeV.364121.Sherpa_221_NNPDF30NNLO_Zee_MAXHTPTV140_280_CFilterBVeto.deriv.DAOD_HIGG8D1.e5299_e5984_s3126_r10201_r10210_p4133
 mc16_13TeV.364122.Sherpa_221_NNPDF30NNLO_Zee_MAXHTPTV140_280_BFilter.deriv.DAOD_HIGG8D1.e5299_e5984_s3126_r10201_r10210_p4133
 mc16_13TeV.364123.Sherpa_221_NNPDF30NNLO_Zee_MAXHTPTV280_500_CVetoBVeto.deriv.DAOD_HIGG8D1.e5299_e5984_s3126_r10201_r10210_p4133
 mc16_13TeV.364124.Sherpa_221_NNPDF30NNLO_Zee_MAXHTPTV280_500_CFilterBVeto.deriv.DAOD_HIGG8D1.e5299_e5984_s3126_r10201_r10210_p4133
 mc16_13TeV.364125.Sherpa_221_NNPDF30NNLO_Zee_MAXHTPTV280_500_BFilter.deriv.DAOD_HIGG8D1.e5299_e5984_s3126_r10201_r10210_p4133
 mc16_13TeV.364126.Sherpa_221_NNPDF30NNLO_Zee_MAXHTPTV500_1000.deriv.DAOD_HIGG8D1.e5299_e5984_s3126_r10201_r10210_p4133

mc16_13TeV.364506.Sherpa_222_NNPDF30NNLO_mumugamma_pty_15_35.deriv.DAOD_HIGG8D1.e5928_e5984_s3126_r10201_r10210_p4133
mc16_13TeV.364507.Sherpa_222_NNPDF30NNLO_mumugamma_pty_35_70.deriv.DAOD_HIGG8D1.e5928_e5984_s3126_r10201_r10210_p4133
mc16_13TeV.364508.Sherpa_222_NNPDF30NNLO_mumugamma_pty_70_140.deriv.DAOD_HIGG8D1.e5928_e5984_s3126_r10201_r10210_p4133
mc16_13TeV.364509.Sherpa_222_NNPDF30NNLO_mumugamma_pty_140_E_CMS.deriv.DAOD_HIGG8D1.e5928_e5984_s3126_r10201_r10210_p4133
mc16_13TeV.364510.Sherpa_222_NNPDF30NNLO_tautaugamma_pty_7_15.deriv.DAOD_HIGG8D1.e5928_e5984_s3126_r10201_r10210_p4133
mc16_13TeV.364511.Sherpa_222_NNPDF30NNLO_tautaugamma_pty_15_35.deriv.DAOD_HIGG8D1.e5928_e5984_s3126_r10201_r10210_p4133
mc16_13TeV.364512.Sherpa_222_NNPDF30NNLO_tautaugamma_pty_35_70.deriv.DAOD_HIGG8D1.e5928_e5984_s3126_r10201_r10210_p4133
mc16_13TeV.364513.Sherpa_222_NNPDF30NNLO_tautaugamma_pty_70_140.deriv.DAOD_HIGG8D1.e5928_e5984_s3126_r10201_r10210_p4133
mc16_13TeV.364513.Sherpa_222_NNPDF30NNLO_tautaugamma_pty_70_140.deriv.DAOD_HIGG8D1.e5928_e5984_s3126_r10201_r10210_p4133
mc16_13TeV.364514.Sherpa_222_NNPDF30NNLO_tautaugamma_pty_140_E_CMS.deriv.DAOD_HIGG8D1.e5928_e5984_s3126_r10201_r10210_p4133
mc16_13TeV.364521.Sherpa_222_NNPDF30NNLO_enugamma_pty_7_15.deriv.DAOD_HIGG8D1.e5928_e5984_s3126_r10201_r10210_p4133
mc16_13TeV.364522.Sherpa_222_NNPDF30NNLO_enugamma_pty_15_35.deriv.DAOD_HIGG8D1.e5928_e5984_s3126_r10201_r10210_p4133
mc16_13TeV.364523.Sherpa_222_NNPDF30NNLO_enugamma_pty_35_70.deriv.DAOD_HIGG8D1.e5928_e5984_s3126_r10201_r10210_p4133
mc16_13TeV.364524.Sherpa_222_NNPDF30NNLO_enugamma_pty_70_140.deriv.DAOD_HIGG8D1.e5928_e5984_s3126_r10201_r10210_p4133
mc16_13TeV.364525.Sherpa_222_NNPDF30NNLO_enugamma_pty_140_E_CMS.deriv.DAOD_HIGG8D1.e5928_e5984_s3126_r10201_r10210_p4133
mc16_13TeV.364526.Sherpa_222_NNPDF30NNLO_munugamma_pty_7_15.deriv.DAOD_HIGG8D1.e5928_e5984_s3126_r10201_r10210_p4133
mc16_13TeV.364527.Sherpa_222_NNPDF30NNLO_munugamma_pty_15_35.deriv.DAOD_HIGG8D1.e5928_e5984_s3126_r10201_r10210_p4133
mc16_13TeV.364528.Sherpa_222_NNPDF30NNLO_munugamma_pty_35_70.deriv.DAOD_HIGG8D1.e5928_e5984_s3126_r10201_r10210_p4133
mc16_13TeV.364529.Sherpa_222_NNPDF30NNLO_munugamma_pty_70_140.deriv.DAOD_HIGG8D1.e5928_e5984_s3126_r10201_r10210_p4133
mc16_13TeV.364530.Sherpa_222_NNPDF30NNLO_munugamma_pty_140_E_CMS.deriv.DAOD_HIGG8D1.e5928_e5984_s3126_r10201_r10210_p4133
mc16_13TeV.364531.Sherpa_222_NNPDF30NNLO_taunugamma_pty_7_15.deriv.DAOD_HIGG8D1.e5928_e5984_s3126_r10201_r10210_p4133
mc16_13TeV.364532.Sherpa_222_NNPDF30NNLO_taunugamma_pty_15_35.deriv.DAOD_HIGG8D1.e5928_e5984_s3126_r10201_r10210_p4133
mc16_13TeV.364533.Sherpa_222_NNPDF30NNLO_taunugamma_pty_35_70.deriv.DAOD_HIGG8D1.e5928_e5984_s3126_r10201_r10210_p4133
mc16_13TeV.364534.Sherpa_222_NNPDF30NNLO_taunugamma_pty_70_140.deriv.DAOD_HIGG8D1.e5928_e5984_s3126_r10201_r10210_p4133
mc16_13TeV.364535.Sherpa_222_NNPDF30NNLO_taunugamma_pty_140_E_CMS.deriv.DAOD_HIGG8D1.e5928_e5984_s3126_r10201_r10210_p4133
mc16_13TeV.410056.MadGraphPythiaEvtGen_A14_iZ_4fl_tchan_noAllHad.deriv.DAOD_HIGG8D1.e5803_e5984_s3126_r10201_r10210_p4133
mc16_13TeV.410013.PowhegPythiaEvtGen_P2012_Wt_inclusive_top.deriv.DAOD_HIGG8D1.e3753_s3126_r10201_r10210_p4133
mc16_13TeV.410014.PowhegPythiaEvtGen_P2012_Wt_inclusive_antitop.deriv.DAOD_HIGG8D1.e3753_s3126_r10201_r10210_p4133
mc16_13TeV.410408.aMcAtNloPythia8EvtGen_tWZ_Ztoll_minDR1.deriv.DAOD_HIGG8D1.e6423_e5984_s3126_r10201_r10210_p4133
mc16_13TeV.364242.Sherpa_222_NNPDF30NNLO_WWW_313v_EW6.deriv.DAOD_HIGG8D1.e5887_e5984_s3126_r10201_r10210_p4133
mc16_13TeV.364243.Sherpa_222_NNPDF30NNLO_WWZ_412v_EW6.deriv.DAOD_HIGG8D1.e5887_e5984_s3126_r10201_r10210_p4133
mc16_13TeV.364244.Sherpa_222_NNPDF30NNLO_WWZ_214v_EW6.deriv.DAOD_HIGG8D1.e5887_e5984_s3126_r10201_r10210_p4133
mc16_13TeV.364245.Sherpa_222_NNPDF30NNLO_WZZ_511v_EW6.deriv.DAOD_HIGG8D1.e5887_e5984_s3126_r10201_r10210_p4133
mc16_13TeV.364246.Sherpa_222_NNPDF30NNLO_WZZ_313v_EW6.deriv.DAOD_HIGG8D1.e5887_e5984_s3126_r10201_r10210_p4133
mc16_13TeV.364247.Sherpa_222_NNPDF30NNLO_ZZZ_610v_EW6.deriv.DAOD_HIGG8D1.e5887_e5984_s3126_r10201_r10210_p4133
mc16_13TeV.364248.Sherpa_222_NNPDF30NNLO_ZZZ_412v_EW6.deriv.DAOD_HIGG8D1.e5887_e5984_s3126_r10201_r10210_p4133
mc16_13TeV.364249.Sherpa_222_NNPDF30NNLO_ZZZ_214v_EW6.deriv.DAOD_HIGG8D1.e5887_e5984_s3126_r10201_r10210_p4133
mc16_13TeV.342284.Pythia8EvtGen_A14NNPDF23LO_WH125_inc.deriv.DAOD_HIGG8D1.e4246_e5984_s3126_r10201_r10210_p4133
mc16_13TeV.342285.Pythia8EvtGen_A14NNPDF23LO_ZH125_inc.deriv.DAOD_HIGG8D1.e4246_e5984_s3126_r10201_r10210_p4133
mc16_13TeV.341998.aMcAtNloHppEG_UEEE5_CTEQ6L1_CT10ME_tWH125_gamgam_yt_plus1.deriv.DAOD_HIGG8D1.e4394_e5984_s3126_r10201_r10210_p4133
mc16_13TeV.410470.PhPy8EG_A14_ttbar_hdamp258p75_nonallhad.deriv.DAOD_HIGG8D1.e6337_e5984_s3126_r10201_r10210_p4133
mc16_13TeV.410472.PhPy8EG_A14_ttbar_hdamp258p75_dil.deriv.DAOD_HIGG8D1.e6348_e5984_s3126_r10201_r10210_p4133
mc16_13TeV.346343.PhPy8EG_A14NNPDF23_NNPDF30ME_ttH125_allhad.deriv.DAOD_HIGG8D1.e7148_e5984_s3126_r10201_r10210_p4133
mc16_13TeV.346344.PhPy8EG_A14NNPDF23_NNPDF30ME_ttH125_semilep.deriv.DAOD_HIGG8D1.e7148_e5984_a875_r10201_r10210_p4133
mc16_13TeV.346345.PhPy8EG_A14NNPDF23_NNPDF30ME_ttH125_dilep.deriv.DAOD_HIGG8D1.e7148_e5984_a875_r10201_r10210_p4133

mc16e:

mc16_13TeV.361605.PowhegPy8EG_CT10nloME_AZNLOCTEQ6L1_ZZvvvv_mll4.deriv.DAOD_HIGG8D1.e4054_e5984_s3126_r10724_r10726_p4133
mc16_13TeV.361602.PowhegPy8EG_CT10nloME_AZNLOCTEQ6L1_WZlvvv_mll4.deriv.DAOD_HIGG8D1.e4054_e5984_s3126_r10724_r10726_p4133
mc16_13TeV.361601.PowhegPy8EG_CT10nloME_AZNLOCTEQ6L1_WZlavl_mll4.deriv.DAOD_HIGG8D1.e4475_e5984_s3126_r10724_r10726_p4133
mc16_13TeV.361600.PowhegPy8EG_CT10nloME_AZNLOCTEQ6L1_WWlvlv.deriv.DAOD_HIGG8D1.e4616_e5984_s3126_r10724_r10726_p4133
mc16_13TeV.361603.PowhegPy8EG_CT10nloME_AZNLOCTEQ6L1_ZZllll_mll4.deriv.DAOD_HIGG8D1.e4475_e5984_s3126_r10724_r10726_p4133
mc16_13TeV.361604.PowhegPy8EG_CT10nloME_AZNLOCTEQ6L1_ZZvvll_mll4.deriv.DAOD_HIGG8D1.e4475_e5984_s3126_r10724_r10726_p4133
mc16_13TeV.364288.Sherpa_222_NNPDF30NNLO_llll_lowMllPtComplement.deriv.DAOD_HIGG8D1.e6096_s3126_r10724_p3983 mc16_13TeV.364287.Sherpa_222_NNPDF30NNLO_llll_lowMllPtComplement.deriv.DAOD_HIGG8D1.e6096_s3126_r10724_p3983
mc16_13TeV.364285.Sherpa_222_NNPDF30NNLO_llvjj_EW6.deriv.DAOD_HIGG8D1.e6055_s3126_r10724_r10726_p3983
mc16_13TeV.364284.Sherpa_222_NNPDF30NNLO_llvjj_EW6.deriv.DAOD_HIGG8D1.e6055_s3126_r10724_p3983
mc16_13TeV.364283.Sherpa_222_NNPDF30NNLO_lllijj_EW6.deriv.DAOD_HIGG8D1.e6055_s3126_r10724_p3983
mc16_13TeV.364739.MGPy8EG_NNPDF30NLO_A14NNPDF23LO_lvjlljjEW6_OFMinus.deriv.DAOD_HIGG8D1.e7421_e5984_s3126_r10724_r10726_p4133
mc16_13TeV.364742.MGPy8EG_NNPDF30NLO_A14NNPDF23LO_lvjlljjEW6_SFPlus.deriv.DAOD_HIGG8D1.e7421_e5984_s3126_r10724_r10726_p4133
mc16_13TeV.364740.MGPy8EG_NNPDF30NLO_A14NNPDF23LO_lvjlljjEW6_OFPlus.deriv.DAOD_HIGG8D1.e7421_e5984_s3126_r10724_r10726_p4133
mc16_13TeV.364741.MGPy8EG_NNPDF30NLO_A14NNPDF23LO_lvjlljjEW6_SFMinus.deriv.DAOD_HIGG8D1.e7421_e5984_s3126_r10724_r10726_p4133
mc16_13TeV.364253.Sherpa_222_NNPDF30NNLO_llv.deriv.DAOD_HIGG8D1.e5916_e5984_s3126_r10724_r10726_p4133

mc16_13TeV.364250.Sherpa_222_NNPDF30NNLO_llll.deriv.DAOD_HIGG8D1.e5894_e5984_s3126_r10724_r10726_p4133
 mc16_13TeV.364254.Sherpa_222_NNPDF30NNLO_llvv.deriv.DAOD_HIGG8D1.e5916_e5984_s3126_r10724_r10726_p4133
 mc16_13TeV.364255.Sherpa_222_NNPDF30NNLO_lvvv.deriv.DAOD_HIGG8D1.e5916_e5984_s3126_r10724_r10726_p4133
 mc16_13TeV.410155.aMcAtNloPythia8EvtGen_MEN30NLO_A14N23LO_ttW.deriv.DAOD_HIGG8D1.e5070_e5984_s3126_r10724_r10726_p4133
 mc16_13TeV.410156.aMcAtNloPythia8EvtGen_MEN30NLO_A14N23LO_ttZnunu.deriv.DAOD_HIGG8D1.e5070_e5984_s3126_r10724_r10726_p4133
 mc16_13TeV.410157.aMcAtNloPythia8EvtGen_MEN30NLO_A14N23LO_ttZqq.deriv.DAOD_HIGG8D1.e5070_e5984_s3126_r10724_r10726_p4133
 mc16_13TeV.410218.aMcAtNloPythia8EvtGen_MEN30NLO_A14N23LO_ttee.deriv.DAOD_HIGG8D1.e5070_e5984_s3126_r10724_r10726_p4133
 mc16_13TeV.410219.aMcAtNloPythia8EvtGen_MEN30NLO_A14N23LO_ttmumu.deriv.DAOD_HIGG8D1.e5070_e5984_s3126_r10724_r10726_p4133
 mc16_13TeV.410220.aMcAtNloPythia8EvtGen_MEN30NLO_A14N23LO_ttautau.deriv.DAOD_HIGG8D1.e5070_e5984_s3126_r10724_r10726_p4133
 mc16_13TeV.410276.aMcAtNloPythia8EvtGen_MEN30NLO_A14N23LO_ttee_mll_1_5.deriv.DAOD_HIGG8D1.e6087_e5984_s3126_r10724_r10726_p4133
 mc16_13TeV.410277.aMcAtNloPythia8EvtGen_MEN30NLO_A14N23LO_ttmumu_mll_1_5.deriv.DAOD_HIGG8D1.e6087_e5984_s3126_r10724_r10726_p4133
 mc16_13TeV.410278.aMcAtNloPythia8EvtGen_MEN30NLO_A14N23LO_ttautau_mll_1_5.deriv.DAOD_HIGG8D1.e6087_e5984_s3126_r10724_r10726_p4133
 mc16_13TeV.410397.MadGraphPythia8EvtGen_ttbar_wbee_MEN30NLO_A14N23LO.deriv.DAOD_HIGG8D1.e6086_e5984_s3126_r10724_r10726_p4133
 mc16_13TeV.410398.MadGraphPythia8EvtGen_ttbar_wbmumu_MEN30NLO_A14N23LO.deriv.DAOD_HIGG8D1.e6086_e5984_s3126_r10724_r10726_p4133
 mc16_13TeV.410399.MadGraphPythia8EvtGen_ttbar_wbtautau_MEN30NLO_A14N23LO.deriv.DAOD_HIGG8D1.e6086_e5984_s3126_r10724_r10726_p4133
 mc16_13TeV.410658.PhPy8EG_A14_tchan_BW50_lept_top.deriv.DAOD_HIGG8D1.e6671_e5984_s3126_s3136_r10724_r10726_p4133
 mc16_13TeV.410659.PhPy8EG_A14_tchan_BW50_lept_antitop.deriv.DAOD_HIGG8D1.e6671_e5984_s3126_s3136_r10724_r10726_p4133
 mc16_13TeV.410644.PowhegPythia8EvtGen_A14_singletop_schan_lept_top.deriv.DAOD_HIGG8D1.e6527_e5984_s3126_r10724_r10726_p4133
 mc16_13TeV.410645.PowhegPythia8EvtGen_A14_singletop_schan_lept_antitop.deriv.DAOD_HIGG8D1.e6527_e5984_s3126_r10724_r10726_p4133
 mc16_13TeV.412063.aMcAtNloPythia8EvtGen_tllq_NNPDF30_nf4_A14.deriv.DAOD_TOPQ1.e7054_e5984_s3126_r10724_r10726_p4174
 mc16_13TeV.304014.MadGraphPythia8EvtGen_A14NNPDF23_3top_SM.deriv.DAOD_HIGG8D1.e4324_e5984_s3126_r10724_r10726_p4133
 mc16_13TeV.410080.MadGraphPythia8EvtGen_A14NNPDF23_4topSM.deriv.DAOD_HIGG8D1.e4111_e5984_s3126_r10724_r10726_p4133
 mc16_13TeV.410081.MadGraphPythia8EvtGen_A14NNPDF23_ttbarWW.deriv.DAOD_HIGG8D1.e4111_e5984_s3126_r10724_r10726_p4133
 mc16_13TeV.364100.Sherpa_221_NNPDF30NNLO_Zmumu_MAXHPTV0_70_CVetoBVeto.deriv.DAOD_HIGG8D1.e5271_e5984_s3126_s3136_r10724_r10726_p4133
 mc16_13TeV.364100.Sherpa_221_NNPDF30NNLO_Zmumu_MAXHPTV0_70_CVetoBVeto.deriv.DAOD_HIGG8D1.e5271_e5984_s3126_r10724_r10726_p4133
 mc16_13TeV.364101.Sherpa_221_NNPDF30NNLO_Zmumu_MAXHPTV0_70_CFilterBVeto.deriv.DAOD_HIGG8D1.e5271_e5984_s3126_r10724_r10726_p4133
 mc16_13TeV.364102.Sherpa_221_NNPDF30NNLO_Zmumu_MAXHPTV0_70_BFilter.deriv.DAOD_HIGG8D1.e5271_e5984_s3126_s3136_r10724_r10726_p4133
 mc16_13TeV.364102.Sherpa_221_NNPDF30NNLO_Zmumu_MAXHPTV0_70_BFilter.deriv.DAOD_HIGG8D1.e5271_e5984_s3126_r10724_r10726_p4133
 mc16_13TeV.364103.Sherpa_221_NNPDF30NNLO_Zmumu_MAXHPTV70_140_CVetoBVeto.deriv.DAOD_HIGG8D1.e5271_e5984_s3126_r10724_r10726_p4133
 mc16_13TeV.364103.Sherpa_221_NNPDF30NNLO_Zmumu_MAXHPTV70_140_CVetoBVeto.deriv.DAOD_HIGG8D1.e5271_e5984_s3126_s3136_r10724_r10726_p4133
 mc16_13TeV.364104.Sherpa_221_NNPDF30NNLO_Zmumu_MAXHPTV70_140_CFilterBVeto.deriv.DAOD_HIGG8D1.e5271_e5984_s3126_r10724_r10726_p4133
 mc16_13TeV.364104.Sherpa_221_NNPDF30NNLO_Zmumu_MAXHPTV70_140_CFilterBVeto.deriv.DAOD_HIGG8D1.e5271_e5984_s3126_s3136_r10724_r10726_p4133
 mc16_13TeV.364106.Sherpa_221_NNPDF30NNLO_Zmumu_MAXHPTV140_280_CVetoBVeto.deriv.DAOD_HIGG8D1.e5271_e5984_s3126_s3136_r10724_r10726_p4133
 mc16_13TeV.364106.Sherpa_221_NNPDF30NNLO_Zmumu_MAXHPTV140_280_CVetoBVeto.deriv.DAOD_HIGG8D1.e5271_e5984_s3126_r10724_r10726_p4133
 mc16_13TeV.364107.Sherpa_221_NNPDF30NNLO_Zmumu_MAXHPTV140_280_CFilterBVeto.deriv.DAOD_HIGG8D1.e5271_e5984_s3126_r10724_r10726_p4133
 mc16_13TeV.364107.Sherpa_221_NNPDF30NNLO_Zmumu_MAXHPTV140_280_CFilterBVeto.deriv.DAOD_HIGG8D1.e5271_e5984_s3126_s3136_r10724_r10726_p4133
 mc16_13TeV.364108.Sherpa_221_NNPDF30NNLO_Zmumu_MAXHPTV140_280_BFilter.deriv.DAOD_HIGG8D1.e5271_e5984_s3126_r10724_r10726_p4133
 mc16_13TeV.364109.Sherpa_221_NNPDF30NNLO_Zmumu_MAXHPTV280_500_CVetoBVeto.deriv.DAOD_HIGG8D1.e5271_e5984_s3126_r10724_r10726_p4133
 mc16_13TeV.364110.Sherpa_221_NNPDF30NNLO_Zmumu_MAXHPTV280_500_CFilterBVeto.deriv.DAOD_HIGG8D1.e5271_e5984_s3126_r10724_r10726_p4133
 mc16_13TeV.364110.Sherpa_221_NNPDF30NNLO_Zmumu_MAXHPTV280_500_CFilterBVeto.deriv.DAOD_HIGG8D1.e5271_e5984_s3126_s3136_r10724_r10726_p4133
 mc16_13TeV.364111.Sherpa_221_NNPDF30NNLO_Zmumu_MAXHPTV280_500_BFilter.deriv.DAOD_HIGG8D1.e5271_e5984_s3126_s3136_r10724_r10726_p4133
 mc16_13TeV.364111.Sherpa_221_NNPDF30NNLO_Zmumu_MAXHPTV280_500_BFilter.deriv.DAOD_HIGG8D1.e5271_e5984_s3126_r10724_r10726_p4133
 mc16_13TeV.364112.Sherpa_221_NNPDF30NNLO_Zmumu_MAXHPTV500_1000.deriv.DAOD_HIGG8D1.e5271_e5984_s3126_r10724_r10726_p4133
 mc16_13TeV.364113.Sherpa_221_NNPDF30NNLO_Zmumu_MAXHPTV1000_E_CMS.deriv.DAOD_HIGG8D1.e5271_e5984_s3126_r10724_r10726_p4133
 mc16_13TeV.364113.Sherpa_221_NNPDF30NNLO_Zmumu_MAXHPTV1000_E_CMS.deriv.DAOD_HIGG8D1.e5271_e5984_s3126_s3136_r10724_r10726_p4133
 mc16_13TeV.364114.Sherpa_221_NNPDF30NNLO_Zee_MAXHPTV0_70_CVetoBVeto.deriv.DAOD_HIGG8D1.e5299_e5984_s3126_s3136_r10724_r10726_p4133
 mc16_13TeV.364114.Sherpa_221_NNPDF30NNLO_Zee_MAXHPTV0_70_CVetoBVeto.deriv.DAOD_HIGG8D1.e5299_e5984_s3126_r10724_r10726_p4133
 mc16_13TeV.364115.Sherpa_221_NNPDF30NNLO_Zee_MAXHPTV0_70_CFilterBVeto.deriv.DAOD_HIGG8D1.e5299_e5984_s3126_s3136_r10724_r10726_p4133
 mc16_13TeV.364115.Sherpa_221_NNPDF30NNLO_Zee_MAXHPTV0_70_CFilterBVeto.deriv.DAOD_HIGG8D1.e5299_e5984_s3126_r10724_r10726_p4133
 mc16_13TeV.364116.Sherpa_221_NNPDF30NNLO_Zee_MAXHPTV0_70_BFilter.deriv.DAOD_HIGG8D1.e5299_e5984_s3126_r10724_r10726_p4133
 mc16_13TeV.364117.Sherpa_221_NNPDF30NNLO_Zee_MAXHPTV70_140_CVetoBVeto.deriv.DAOD_HIGG8D1.e5299_e5984_s3126_s3136_r10724_r10726_p4133
 mc16_13TeV.364117.Sherpa_221_NNPDF30NNLO_Zee_MAXHPTV70_140_CVetoBVeto.deriv.DAOD_HIGG8D1.e5299_e5984_s3126_r10724_r10726_p4133
 mc16_13TeV.364118.Sherpa_221_NNPDF30NNLO_Zee_MAXHPTV70_140_CFilterBVeto.deriv.DAOD_HIGG8D1.e5299_e5984_s3126_s3136_r10724_r10726_p4133
 mc16_13TeV.364118.Sherpa_221_NNPDF30NNLO_Zee_MAXHPTV70_140_CFilterBVeto.deriv.DAOD_HIGG8D1.e5299_e5984_s3126_r10724_r10726_p4133
 mc16_13TeV.364119.Sherpa_221_NNPDF30NNLO_Zee_MAXHPTV70_140_BFilter.deriv.DAOD_HIGG8D1.e5299_e5984_s3126_r10724_r10726_p4133
 mc16_13TeV.364120.Sherpa_221_NNPDF30NNLO_Zee_MAXHPTV140_280_CVetoBVeto.deriv.DAOD_HIGG8D1.e5299_e5984_s3126_r10724_r10726_p4133
 mc16_13TeV.364121.Sherpa_221_NNPDF30NNLO_Zee_MAXHPTV140_280_CFilterBVeto.deriv.DAOD_HIGG8D1.e5299_e5984_s3126_r10724_r10726_p4133
 mc16_13TeV.364122.Sherpa_221_NNPDF30NNLO_Zee_MAXHPTV140_280_BFilter.deriv.DAOD_HIGG8D1.e5299_e5984_s3126_s3136_r10724_r10726_p4133
 mc16_13TeV.364122.Sherpa_221_NNPDF30NNLO_Zee_MAXHPTV140_280_BFilter.deriv.DAOD_HIGG8D1.e5299_e5984_s3126_r10724_r10726_p4133
 mc16_13TeV.364123.Sherpa_221_NNPDF30NNLO_Zee_MAXHPTV280_500_CVetoBVeto.deriv.DAOD_HIGG8D1.e5299_e5984_s3126_r10724_r10726_p4133
 mc16_13TeV.364124.Sherpa_221_NNPDF30NNLO_Zee_MAXHPTV280_500_CFilterBVeto.deriv.DAOD_HIGG8D1.e5299_e5984_s3126_r10724_r10726_p4133
 mc16_13TeV.364125.Sherpa_221_NNPDF30NNLO_Zee_MAXHPTV280_500_BFilter.deriv.DAOD_HIGG8D1.e5299_e5984_s3126_s3136_r10724_r10726_p4133

mc16_13TeV.364513.Sherpa_222_NNPDF30NNLO_tautaugamma_pty_70_140.deriv.DAOD_HIGG8D1.e5982_e5984_s3126_r10724_r10726_p4133
 mc16_13TeV.364514.Sherpa_222_NNPDF30NNLO_tautaugamma_pty_140_E_CMS.deriv.DAOD_HIGG8D1.e5928_e5984_s3126_r10724_r10726_p4133
 mc16_13TeV.364522.Sherpa_222_NNPDF30NNLO_enugamma_pty_15_35.deriv.DAOD_HIGG8D1.e5928_e5984_s3126_r10724_r10726_p4133
 mc16_13TeV.364523.Sherpa_222_NNPDF30NNLO_enugamma_pty_35_70.deriv.DAOD_HIGG8D1.e5928_e5984_s3126_r10724_r10726_p4133
 mc16_13TeV.364524.Sherpa_222_NNPDF30NNLO_enugamma_pty_70_140.deriv.DAOD_HIGG8D1.e5928_e5984_s3126_r10724_r10726_p4133
 mc16_13TeV.364525.Sherpa_222_NNPDF30NNLO_enugamma_pty_140_E_CMS.deriv.DAOD_HIGG8D1.e5928_e5984_s3126_r10724_r10726_p4133
 mc16_13TeV.364527.Sherpa_222_NNPDF30NNLO_munugamma_pty_15_35.deriv.DAOD_HIGG8D1.e5928_e5984_s3126_r10724_r10726_p4133
 mc16_13TeV.364528.Sherpa_222_NNPDF30NNLO_munugamma_pty_35_70.deriv.DAOD_HIGG8D1.e5928_e5984_s3126_r10724_r10726_p4133
 mc16_13TeV.364529.Sherpa_222_NNPDF30NNLO_munugamma_pty_70_140.deriv.DAOD_HIGG8D1.e5928_e5984_s3126_r10724_r10726_p4133
 mc16_13TeV.364530.Sherpa_222_NNPDF30NNLO_munugamma_pty_140_E_CMS.deriv.DAOD_HIGG8D1.e5928_e5984_s3126_r10724_r10726_p4133
 mc16_13TeV.364532.Sherpa_222_NNPDF30NNLO_taunugamma_pty_15_35.deriv.DAOD_HIGG8D1.e5928_e5984_s3126_r10724_r10726_p4133
 mc16_13TeV.364533.Sherpa_222_NNPDF30NNLO_taunugamma_pty_35_70.deriv.DAOD_HIGG8D1.e5928_e5984_s3126_r10724_r10726_p4133
 mc16_13TeV.364534.Sherpa_222_NNPDF30NNLO_taunugamma_pty_70_140.deriv.DAOD_HIGG8D1.e5928_e5984_s3126_r10724_r10726_p4133
 mc16_13TeV.364535.Sherpa_222_NNPDF30NNLO_taunugamma_pty_140_E_CMS.deriv.DAOD_HIGG8D1.e5928_e5984_s3126_r10724_r10726_p4133
 mc16_13TeV.410560.MadGraphPythia8EvtGen_A14_tZ_4fl_tchan_noAllHad.deriv.DAOD_HIGG8D1.e5803_e5984_s3126_r10724_r10726_p4133
 mc16_13TeV.410408.aMcAtNloPythia8EvtGen_tWZ_Ztoll_minDR1.deriv.DAOD_HIGG8D1.e6423_e5984_s3126_r10724_r10726_p4133
 mc16_13TeV.364242.Sherpa_222_NNPDF30NNLO_WWW_3l3v_EW6.deriv.DAOD_HIGG8D1.e5887_e5984_s3126_r10724_r10726_p4133
 mc16_13TeV.364243.Sherpa_222_NNPDF30NNLO_WWZ_4l2v_EW6.deriv.DAOD_HIGG8D1.e5887_e5984_s3126_r10724_r10726_p4133
 mc16_13TeV.364244.Sherpa_222_NNPDF30NNLO_WWZ_2l4v_EW6.deriv.DAOD_HIGG8D1.e5887_e5984_s3126_r10724_r10726_p4133
 mc16_13TeV.364245.Sherpa_222_NNPDF30NNLO_WZZ_5l1v_EW6.deriv.DAOD_HIGG8D1.e5887_e5984_s3126_r10724_r10726_p4133
 mc16_13TeV.364246.Sherpa_222_NNPDF30NNLO_WZZ_3l3v_EW6.deriv.DAOD_HIGG8D1.e5887_e5984_s3126_r10724_r10726_p4133
 mc16_13TeV.364247.Sherpa_222_NNPDF30NNLO_ZZZ_6l0v_EW6.deriv.DAOD_HIGG8D1.e5887_e5984_s3126_r10724_r10726_p4133
 mc16_13TeV.364248.Sherpa_222_NNPDF30NNLO_ZZZ_4l2v_EW6.deriv.DAOD_HIGG8D1.e5887_e5984_s3126_r10724_r10726_p4133
 mc16_13TeV.364249.Sherpa_222_NNPDF30NNLO_ZZZ_2l4v_EW6.deriv.DAOD_HIGG8D1.e5887_e5984_s3126_r10724_r10726_p4133
 mc16_13TeV.342284.Pythia8EvtGen_A14NNPDF23LO_WH125_inc.deriv.DAOD_HIGG8D1.e4246_e5984_s3126_r10724_r10726_p4133
 mc16_13TeV.342285.Pythia8EvtGen_A14NNPDF23LO_ZH125_inc.deriv.DAOD_HIGG8D1.e4246_e5984_s3126_r10724_r10726_p4133
 mc16_13TeV.341998.aMcAtNloHppEG_UEEE5_CTEQ6L1_CT10ME_tWH125_gamgam_yt_plus1.deriv.DAOD_HIGG8D1.e4394_e5984_s3126_r10724_r10726_p4133
 mc16_13TeV.410389.MadGraphPythia8EvtGen_A14NNPDF23_ttgamma_nonallhadronic.deriv.DAOD_HIGG8D1.e6155_e5984_s3126_r10724_r10726_p4133
 mc16_13TeV.410470.PhPy8EG_A14_ttbar_hdamp258p75_nonallhad.deriv.DAOD_HIGG8D1.e6337_e5984_s3126_r10724_r10726_p4133
 mc16_13TeV.410472.PhPy8EG_A14_ttbar_hdamp258p75_dil.deriv.DAOD_HIGG8D1.e6348_e5984_s3126_r10724_r10726_p4133
 mc16_13TeV.346343.PhPy8EG_A14NNPDF23_NNPDF30ME_ttH125_allhad.deriv.DAOD_HIGG8D1.e7148_e5984_s3126_r10724_r10726_p4133
 mc16_13TeV.346343.PhPy8EG_A14NNPDF23_NNPDF30ME_ttH125_allhad.deriv.DAOD_HIGG8D1.e7148_e5984_a875_r10724_r10726_p4133
 mc16_13TeV.346344.PhPy8EG_A14NNPDF23_NNPDF30ME_ttH125_semilep.deriv.DAOD_HIGG8D1.e7148_e5984_a875_r10724_r10726_p4133
 mc16_13TeV.346344.PhPy8EG_A14NNPDF23_NNPDF30ME_ttH125_semilep.deriv.DAOD_HIGG8D1.e7148_e5984_s3126_r10724_r10726_p4133
 mc16_13TeV.346345.PhPy8EG_A14NNPDF23_NNPDF30ME_ttH125_dilep.deriv.DAOD_HIGG8D1.e7148_e5984_a875_r10724_r10726_p4133
 mc16_13TeV.346345.PhPy8EG_A14NNPDF23_NNPDF30ME_ttH125_dilep.deriv.DAOD_HIGG8D1.e7148_e5984_s3126_r10724_r10726_p4133